Cu_2O – ZnO p-n Junctions

Thermodynamics, Structure, and Properties – an Experimental
and Theoretical Study

Kevin Gregor Both

M.Sc. Thesis submitted to the Faculty of Mathematics and
Natural Sciences
UNIVERSITY OF OSLO

15.5.2019

University of Oslo

M.Sc. Thesis

Coexistent Cu$_2$O – ZnO p-n Junction

Thermodynamics, Structure, and Properties – an Experimental and Theoretical Study

Author:
Kevin Gregor Both

Supervisor:
Prof. Dr. Truls Norby

Co-Supervisors:
Prof. Dr. Ole Martin Løvvik
Dr. Tor S. Bjørheim
Dr. Calliope Bazioti

A thesis submitted in partial fulfillment of the

requirements for the degree of Master of Science

in the

Group for Electrochemistry,

Department of Chemistry,

Faculty of Mathematics and Natural Sciences

15 May 2019

Cu$_2$O-ZnO p-n-Junctions: Thermodynamics, Structure, and Properties – an Experimental and Theoretical Study

Kevin Gregor Both

Summary

Cuprous oxide (Cu_2O) is a promising material for an active top-layer in a tandem solar cell. Among others, zinc oxide (ZnO) has been suggested to be a suitable partner for the realization of a p-n-junction with Cu_2O used in a tandem solar cell. However, the reported conversion efficiencies are well below the theoretical value, and a cupric oxide (CuO) interlayer is believed to be the origin of the low experimental conversion efficiency. To study this behavior, different techniques, of both theoretical and experimental nature, have been utilized in this work.

Sol-gel formation of cuprous oxide powders, as well as the manufacturing of pellets, allowed the study of the influence of the oxygen partial pressure and the temperature on the phases formed. The experiments utilized ambient oxygen partial pressure, argon gas, and a mixture of argon and hydrogen gas to control the atmosphere. In contrast to the predicted dominant CuO phase for temperatures between 25℃ and 1000℃, a different behavior of the copper (Cu) system was found. Below 350℃ Cu, both Cu_2O and CuO can be formed, suggesting that the determining factor is not thermodynamics, but kinetics. Above 350℃, the system follows the thermodynamic plot.

Thin film p-n-junctions were manufactured by pulsed laser deposition, utilizing the pellets manufactured in the previous step. While the atmosphere in the chamber was argon (Ar) throughout all the experiments, the distance between the target and the silicon (Si) substrate, mechanical setting of the machine, number of shots, and energy per shot and square centimeter were adjusted to deposit both cuprous oxide and zinc oxide. The deposition order influenced the ZnO thin film quality, where ZnO deposited directly on Si showed a superior crystal quality than ZnO deposited on Cu_2O.

The quality of the thin films, as well as the phases present, were assessed by (scanning) transmission electron microscope ((S)TEM) experiments. The experiments provided nano-scale structural and chemical information. TEM and STEM imaging, selected-area diffraction (SAED) patterns, and energy dispersive x-ray spectroscopy (EDS) allowed for the determination of the phases present, as well as crystal quality of the films. The SAED pattern of the interface between Cu_2O and ZnO suggests the presence of a CuO phase.

Density functional theory was utilized to determine the most stable interfaces among the three phases observed while studying the junction. The calculations, utilizing the PBE functional, show that the cupric oxide – cuprous oxide and cupric oxide – zinc oxide interfaces are more stable than the cuprous oxide – zinc oxide interface, for any studied orientation, with

energies of formation ranging between -0.054 to -0.123 eV per atom. This supports the formation of a cupric oxide interlayer independent of growing order.

The argon atmosphere and the use of a cuprous oxide target did not change the conditions enough to hinder the formation of the cupric oxide layer at the interface. Moreover, thermodynamic considerations, defect chemistry, and the experiments conducted in this work hint at the inherent instability of the junction, where the formation of cupric oxide is promoted at elevated temperatures even in an argon atmosphere. As a potential alternative p-n-junction, the cupric oxide – zinc oxide junction is suggested.

Preface

This work would not have been possible without a plethora of people. First, I would like to thank the scientific community at the University of Oslo, especially SMN. It was a pleasure to work and study within the Group for Electrochemistry and participate in the Structure Physics Group. I want to extend a special thank you to my supervisor Truls Norby, and my co-supervisors Ole Martin Løvvik, Tor Svendsen Bjørheim, and Calliope Bazioti for their time, energy, input, and discussions. Furthermore, I would like to thank Øystein Prytz, Thomas Aarholt, and Phuong Dan Nguyen for their help with the TEM and analysis of the results, and Kaiqi Xu and Amir Masoud Dayaghi for their help with the PLD. I would be remissed if I did not mention Heine, Sindre, Mikael, Stian, and Håkon, and thank them for sharing an office with me. I cannot name every person I had a conversation with about this thesis, but I would like to thank you all.

Second, I want to thank all the people I have met during these two years in Oslo. It has been a real pleasure living here. With that, a special thanks go to Erik, Jonas, and Peder for sharing an apartment with me, and to Oscar, without whom I probably would not have thought about applying to this M.Sc. program.

Last, I would like to thank my friends and family outside of Norway. This work, as well as my attendance at the University of Oslo, would not have been possible without you. Most importantly I want to thank my parents and my sister for their unconditional support, their frequent visits to Oslo, and care packages with goods I missed slightly more than I want to admit. Again, there are too many people to mention all by name, but a big thank you to everyone supporting me during the last years.

University of Oslo, May 2018

Kevin Gregor Both

Table of Content

Table of Content

List of Abbreviations

AM (with G = Global, D = Direct)	Air Mass
ALD	Atomic Layer Deposition
BF	Bright Field
DFT	Density Functional Theory
EDS	Energy-Dispersive X-Ray Spectroscopy
FEG	Field Emission Gun
HAADF	High-Angular Annual Dark Field
HRTEM	High-Resolution Transmission Electron Microscopy
K – V	Kröger – Vink
MD	Misfit Dislocation
PIPS	Precision Ion Polishing System
PLD	Pulsed Laser Deposition
rf	Radio Frequency
SEM	Scanning Electron Microscopy
SAED	Selected-Area Electron Diffraction
(S)TEM	(Scanning) Transmission Electron Microscopy
TCO	Transparent Conducting Oxide
UV	Ultra Violet
VAPE	Vacuum Arc Plasma Evaporation
VASP	Vienna Ab-initio Simulation Package
XRD	X-Ray Diffraction

List of Abbreviations

1. Introduction

The universe consists of naturally occurring and artificially changed materials. These materials not only make up the world, but their properties shape the reality every life-form experiences. Throughout the history of humanity, materials properties have been studied and altered to increase the odds of survival or to display prosperity. Specific periods in history are named after the materials with significant influence on that time [1]. However, materials science as a specific scientific field is a recent development, and a large part of humankind's discoveries and advancements in utilizing materials properties were through empirical means [1]. In comparison to ceramics, used for thousands of years, the study of semiconductors is a young field in materials science [1, 2].

The study of semiconducting materials began during the late 18th and early 19th century. The term *"materials of semiconducting nature"* was introduced by Volta in 1782 [3, 4]. Volta also determined that the frogs' legs in Galvani's experiment moved because of electricity [4]. Followed by Seebeck and Faraday, and many others like Hans Christian Ørsted, he pioneered the study of semiconducting materials. Thomas Johan Seebeck discovered the thermoelectric effects in late 1820 [5], and Michael Faraday described a decreasing resistance of silver sulfide with increasing temperatures in 1839 [6]. These two observations and numerous others made during the 19th century could, however, only be explained collectively with the development of solid-state physics in the 20th century [4]. In the 1940s, Russel Ohl developed the first silicon (Si) based solar cell, and within that work described the first p-n-junction [7, 8].

The importance of the p-n-junction in today's world cannot be overstated. Diodes, transistors, solar cells, and integrated circuits utilize billions of junctions all over the world, both profiting from many advances and leading to improvements in the technology [7, 8]. While the principles remained the same, the size of a single junction, initially described in millimeters (mm), shrank to nanometers (nm). To further decrease the size, and consequently increase the density of junctions in a device, advancements in current manufacturing methods or new concepts have to be introduced. The classical Si-based homojunction, for example, is seldom stable at elevated temperatures, due to the diffusion of the dopants. The identical crystal structure of the p- and n-doped Si allows the respective dopants to cross the junction easily. Hence, elevated temperatures lead to an intermixing of the dopants and irreversible destruction of the junctions' properties. New ideas can overcome these limitations by utilizing different concepts, such as coexistence. A coexistent p-n-junction uses the same working principle as a

Si-based homojunction while using two distinct phases that coexist and cannot intermix further. Consequently, in two different semiconductors that are p- and n-type already, the destructive diffusion of dopants is eliminated.

1.1. Semiconductors, Oxides, and Coexistence

A material can be described as a metal, a semi-metal, a semiconductor, or an insulator. There are two ways to differentiate between them. The first is to distinguish them concerning their electrical resistivity at room temperature. Typically, an insulator has a resistivity above 10^{14} Ωm, while semiconductors have resistivities ranging from 10^{-2} Ωm to 10^9 Ωm [9]. Consequently, semimetals and metals have even lower resistivities. The second way to categorize them is based on their band gap value. Metals do not possess a band gap and have a large valence and conduction band overlap. Semimetals have no band gap either, but their charge carrier concentration at the Femi level is virtually zero.
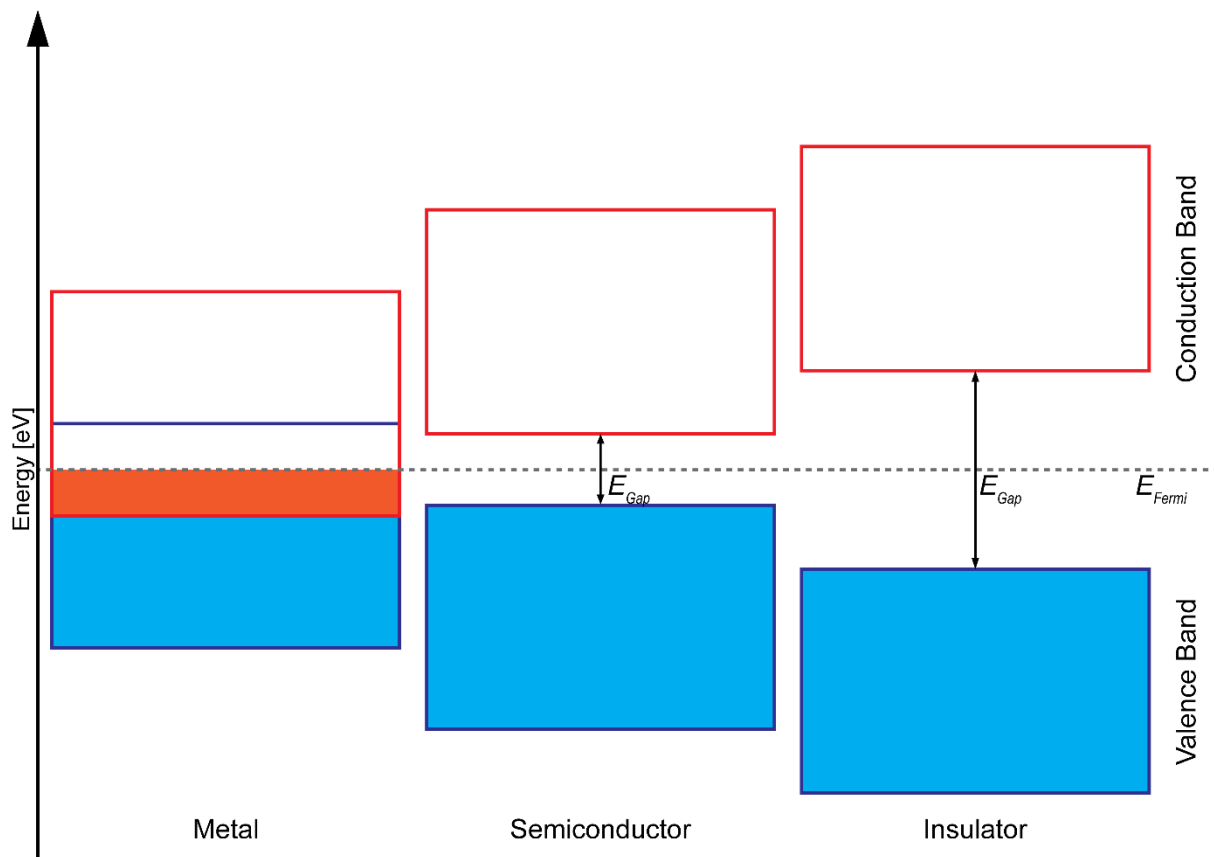
Figure 1: The Fermi level (E_{Fermi}) indicates the energy level up to which bands are filled with electrons. A metal has overlapping conduction and valence bands, resulting in a partly filled conduction band and a partly empty valence band. A semiconductor has a band gap ($E_{Gap} < 4$ eV), resulting in a filled valence band and an empty conduction band. An insulator with its band gap ($E_{Gap} > 4$ eV), has a filled valence band, and an empty conduction band. Electrons in semiconductors can be excited into the conduction band easily, in contrast to electrons in insulators that require considerable energy to be excited into the conduction band.

In contrast, both semiconductors and insulators possess a band gap. Semiconductors have a small band gap (< 4 eV) in comparison to the wide band gap of insulators (> 4 eV) [9-11], as shown in Figure 1. The electrons in a semiconductor can be excited easily into the conduction band. The behavior can be utilized in different devices such as diodes, transistors, and solar cells. This behavior is in contrast to the electrons in insulators, which require considerably more energy to be excited into the conduction band.

A solar cell device, such as described by Ohl, is still a popular device to describe p-n-junctions [12-19]. The field tries to keep up with the rising energy demand by taking advantage of improvements of the standard Si-homojunction solar cell, as well as device architectures beyond Si-based photovoltaic materials [12]. New concepts have been proposed, such as photon-harvesting dye molecules adsorbed on a gold-coated titanium oxide (TiO_2) layer [20]. These devices have a light-to-energy conversion efficiency of less than one percent [20]. Hence, the traditional concept with a higher conversion efficiency remains dominant. The critical factor for all concepts, novel or old, is the conversion efficiency, η, of devices. In general, the efficiency is governed by optical properties, charge carrier diffusion length, and the thickness and morphology of the device [21]. The film thickness, for example, can be increased to raise the conversion efficiency, however, often a thicker film is detrimental due to the thickness of the film becoming greater than the average diffusion length of an electron [22]. The film thickness and many other parameters have to be optimized for each system, to create a new type of solar cell able to compete with the Si-based devices.

Another concept, rather than using dye molecules on gold covered TiO_2 is utilizing copper oxides as active layers. Copper oxides are both abundant and have suitable optical properties for solar cell applications [12, 16, 17]. In particular cuprous oxide (Cu_2O) has been subject to numerous studies in this field [12, 16], but no device has been introduced to the private market. The low conversion efficiency is one of the main issues and concerns [12, 14, 16, 23-25]. Therefore, maximizing the conversion efficiency has been a critical effort, and improvements have been made during the past decades.

1.1.1. Copper and its Oxides

Copper (Cu) is a metal used in, for example, wires, microelectronics [26], and catalysts [27]. Moreover, it can be used as a direct precursor for the different copper oxides and will change phase with little more than oxygen and elevated temperature. Cupric oxide (CuO, tenorite; see Figure 2 (a)) is a stable semiconductor with a monoclinic crystal structure (space group: C2/c)

1. Introduction

[18, 28]. It has a direct band gap of ~1.5 eV, and a high absorption coefficient in the visible region. The ideal bandgap for solar cells is ~1.4 eV [18], which suits CuO rather well. The melting point of CuO is 1026℃ [29-35].

Moreover, CuO can form a p-n-junction with Si, where, depending on the respective doping, either one of the two layers can be the n-doped one [18]. CuO can also be used in entirely different architectures, e.g., as a counter electrode in a dye-sensitized solar cell [36]. However, the poor conversion efficiency in comparison to the standard Si-based solar cells prevents CuO to be used commercially in photovoltaic modules [18]. The poor performance has been attributed to a Cu-rich interlayer and a native oxide formation of SiO_x [37, 38]. Moreover, the charge transport properties of CuO are worse than those of cuprous oxide [37].

Cu_2O (cuprous oxide, cuprite; Figure 2 (b)) is nontoxic, abundant on earth, low-cost producible, and has a high absorption coefficient in the visible region of 10^5 cm^{-1} [18, 24, 39]. Its melting point has been reported as 1223℃ $\pm$ 2℃ [29, 40-43]. It has a cubic crystal cell (space group: $Pn\overline{3}m$, $a = 0.427$ nm) with fourfold coordinated oxygen atoms (O) at the tetrahedral site of the face-centered cubic lattice structure formed by the Cu atoms [16, 28]. Intrinsically, Cu_2O is a p-type semiconductor, most likely due to copper vacancies with a majority carrier mobility of ~100 cm^{2}V^{-1}s^{-1} [28]. Nitrogen (N) and carbon (C) can both be introduced as p-type dopants [18, 28, 44]. Cu_2O possesses a direct band gap of $1.7 - 2$ eV, depending on the deposition technique [18, 28]. Utilizing Cu_2O as an active layer in solar cells yields a theoretical efficiency as high as 20% [28]. Its band gap suggests the usage of the Cu_2O-based solar cell in a tandem solar cell, using a Si solar cell below.
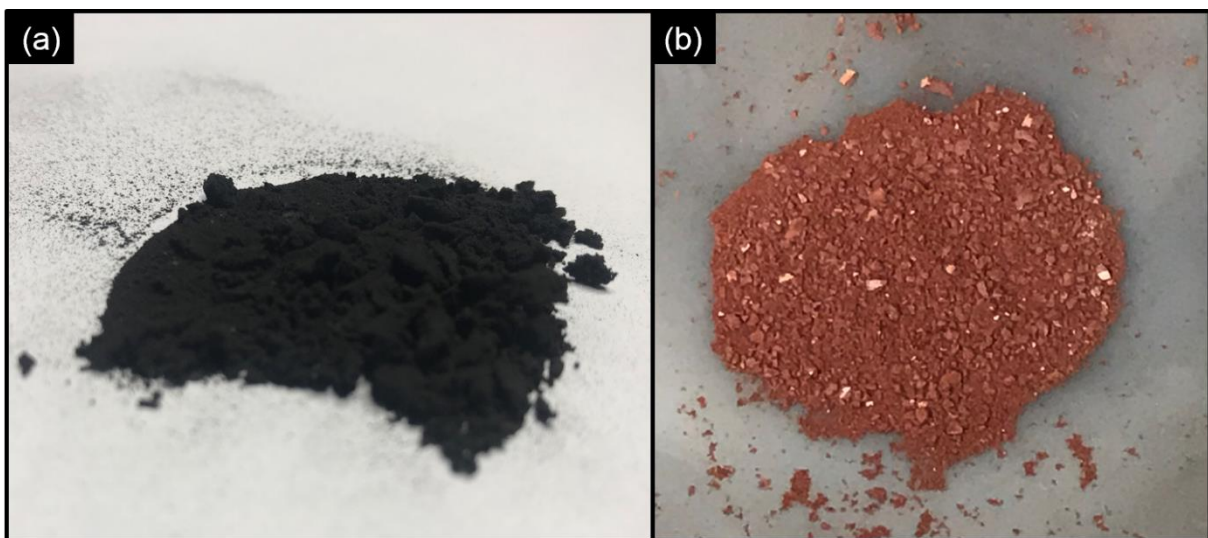

Figure 2 (a): The CuO powder after calcination (see section 3.1.1). (b) Cu_2O and Cu powder of a crushed pellet (see section 3.1.2). The two powders are easily distinguishable due to their colors. By exposing them to a specific temperature and oxygen partial pressure, they can change into the other oxide.

Other copper oxides exist, too. Copper peroxide (CuO_2) is unstable, and copper(III) oxide (Cu_2O_3) has not been obtained as pure solid but is suggested to have superconducting properties [28]. Finally, paramelaconite (Cu_4O_3) is another semiconductor with tetragonal symmetry [18, 28]. Cu_4O_3 is used in thin film heterojunction solar cells, but it has not been reported as bulk material [28]. Furthermore, it is found to be kinetically stable up to 250℃ in air [28]. The heterojunction reported was formed with gallium nitride (GaN) on a sapphire substrate. However, the obtained photovoltaic parameters are lower than those of a comparable Cu_2O/GaN heterojunction under AM 1.5G (global air mass) [18, 28]. The Cu_2O is the most promising copper oxide utilized in a solar cell.

1.1.2. Zinc Oxide

Initially, zinc oxide (ZnO) was regarded as a suitable substrate for GaN and other materials, due to its availability as a large bulk single crystal. However, its unique properties led ZnO to be considered as a functional material for electronic and photonic devices [45-49]. ZnO is a semiconductor with a wide band gap between 3.37 eV to 3.44 eV, and an excitation binding energy of 60 meV [50-55]. Its melting point is regarded as 1975℃, well above the melting points of CuO and Cu_2O [29, 43, 56]. The width of the bandgap allows ZnO to be utilized in optoelectronics in the blue/UV region [45-50].

Nonetheless, its electric conductivity remains an issue because its electrical and optical properties are easily affected by small concentrations of native point defects (as little as 10^{-4} cm^{-3} or 0.01 ppm) [50]. ZnO is n-type in most, if not all, cases, and the cause remains heavily discussed [50, 57-59]. ZnO has a hexagonal wurtzite crystal structure (space group: P6mc, $a = 0.325$ nm, $c = 0.521$ nm), and the Zn^{2+} and O^{2-} ions have tetrahedral coordination, in planes stacked alternately along the c-axis [16, 60]. This stacking results in polar basal surfaces, leading to a normal dipole moment, spontaneous polarization along the c-axis, and divergence in surface energy [60]. Furthermore, ZnO has a sizeable free-exciton binding energy of 60 meV, suggesting reasonable excitonic emission at room temperature or higher temperatures [50, 61, 62]. The oscillator strength of excitons is generally much larger than that of direct electron-hole transitions in direct band-gap semiconductors. Due to this large exciton binding energy, ZnO is a promising material for optical devices based on exciton effects [50, 63]. The combination of a large electromechanical coupling in ZnO and the low symmetry of the wurtzite crystal structure leads to strong piezoelectric and pyroelectric properties [50, 60, 64-71]. ZnO has an intense luminescence, with a spectrum peak at 495 nm and a half width of 0.4 eV. This makes

ZnO qualified for phosphor applications [50]. Moreover, ZnO has high thermal conductivity and as a consequence has a high efficiency of heat removal during device operation [50, 72, 73]. All in all, ZnO displays one of the richest families of nanostructures among materials [60].

1.1.3. Coexistence

Two phases that coexist are neighbors in a phase diagram under any condition where the phases exist. Hence, the two substances do not intermix beyond a certain amount, forming two, rather than one phase, even at elevated temperatures. Determining the respective solubility accurately for the system at hand is a significant step in manufacturing a material with two phases, separated by a well-defined boundary. The solubility of Cu_2O in ZnO at 1095℃ and $p_{O2} = 0.21$ atm is 0.48 mol%, and the solubility of ZnO in Cu_2O at the same conditions is 0.63 mol% [29]. While both phases are solid for the stated values, increasing the temperature liquefies the copper phase and increases its capacity to take up ZnO [29].
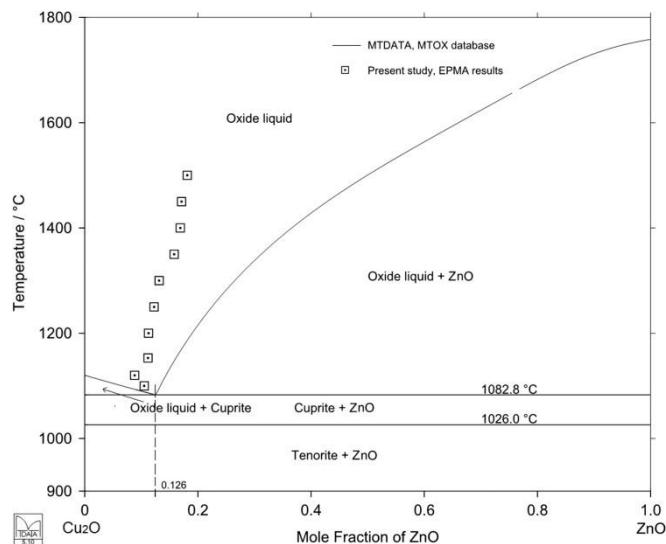
Figure 3: The phases obtained plotted in a temperature versus mole fraction of ZnO plot. The binary eutectic point was found to be 1082.8℃ at 0.126 mole fraction ZnO (plot by L. Xia *et al.*, published in [29]).

1.2. Hypothesis, Approach, and Methodology

The diffusion and inevitable destruction of a traditional p-n-junction at elevated temperatures limit the use of these devices. A thermodynamically stable p-n-junction would overcome these limitations and the resulting need for cooling in today's technology. A coexistent junction does not diffuse, but keeps its initial element distribution, and does not disintegrate. However, finding two materials that are simultaneously thermodynamically stable, and effectively act as

p-n-junction has proven to be difficult. Furthermore, it was previously reported that atomically sharp junctions between Cu_2O and ZnO are difficult to obtain [16].

Several studies have reported the successful formation of the interface, but with PV efficiency results well below the theoretical limit [14, 74, 75]. The formation of CuO at the interface observed in two publications indicates an excess of oxygen [16, 17]. This formation creates a problem due to the lower band gap of CuO, for example in photovoltaic applications, where the CuO does not contribute to the photocurrent but absorbs photons, preventing them from reaching the Cu_2O [13]. Removing excessive oxygen by introducing oxygen-poor atmospheres could prevent the formation of CuO. It is, however, not ensured that this process will yield a steady state composition. A combination of density functional theory (DFT) and experimental work will reveal the likelihood and stability of an atomically sharp interface between Cu_2O and ZnO.

1.2.1. Hypothesis

We hypothesize that the Cu_2O – ZnO junction can be made with two domains that have no concentration gradients of elements within them due to the interface, if the oxygen activity is kept under control during the manufacturing process and usage. While preventing CuO formations is indispensable to this, manufacturing and experimental methods determine the sharpness, and the stability of the interface is determined by the composition itself. We further suggest that such a stable and sharp hetero-interface between coexistent materials may exhibit properties (e.g., thermal stability) superior to those of traditional inter-diffused, and thus blurred, p-n-junctions.

1.2.2. Approach and Limitations

Before manufacturing the junction, a study of the calcination and sintering behavior of Cu_2O, and ZnO rich Cu_2O has to be completed. This will reveal the conditions and setup allowing the formation of Cu_2O. The starting method will be the sol-gel method, and the influence of the different parameters during the process will be investigated. The powders will be analyzed by x-ray diffraction (XRD).

Using the particles obtained in the sol-gel method, pellets will be pressed, and the influence of the sintering atmosphere and temperature will be investigated. A ProboStat^{TM} (NorECs AS ProboStat^{TM}, Oslo, Norway) will be used to ensure that the oxygen partial pressure

1. Introduction

can be controlled. Both, a scanning electron microscope (SEM) and XRD, will be used to characterize the pellets and determine the best conditions to manufacture Cu_2O pellets. Simultaneously, a ZnO pellet will be manufactured to obtain both a ZnO and Cu_2O target.

Using pulsed laser deposition (PLD), the two oxides will be deposited in a thin film manner. The pellets manufactured during the previous step will be used as a target. The parameters used during the deposition as well as the order of deposition will be recorded. Finally, the thin-film samples will be examined by (scanning) transmission electron miscroscope ((S)TEM) observations, in order to characterize the obtained junctions. The information gained among each step will be used to adjust the manufacturing process in order to create a near-perfect junction.

The project is limited to the study of the combination of Cu_2O and ZnO as materials itself, and the coexistent oxide p-n-junction thereof. This includes electrical TEM/STEM analysis, SEM analysis, XRD and DFT calculations. The DFT calculations serve the purpose of determining the most stable interface, and the energy difference between a system with CuO interlayer and one without.

1.2.3. Methodology

An overview will be established by observing the formation behavior of copper oxides at different temperatures with the sol-gel method. Simultaneously, the DFT calculations will indicate which phases can be expected, and how stable each phase is in combination with ZnO. The combination of both, sol-gel experiments and DFT will yield parameters used during the manufacturing of various pellets. Moreover, the previously observed behavior at the junction can be explained by evaluation of these experiments.

The sample production, adjusted by the sol-gel and DFT results, consists of making pellets in a ProboStat, depositing the thin film by PLD, and preparing samples for the TEM. During the sintering of the samples, the atmosphere, temperature, and the subsequent cooling procedure can be varied. The PLD allows us to change the deposition order, substrate temperature, atmosphere, and various laser-related parameters. All of these parameters have to be optimized in order to deposit a good p-n-junction on a Si wafer. The thin films of both Cu_2O and ZnO will have no specific orientation.

The samples characterized by (S)TEM. (S)TEM can provide significant structural and chemical information, such as the orientation relationship of the heterostructure, the sharpness of the interface, strain relaxations mechanism (e.g., through misfit dislocations (MDs)), and the

existence of different phases. These results will be compared to the DFT results, and influence the growing process of additional samples.

1.2.4. Expected Results and Impact

The project aims to develop a coexisting system that serves as an efficient p-n-junction. The thermodynamic stability of the Cu_2O – ZnO-junction will be determined through TEM analysis and DFT calculations. Either theoretical reasoning of the instability of the interface in combination with an inability to obtain it practically, or inconclusive data but practical inability to obtain a pure interface by these methods can lead to its dismissal. However, the process does allow for the characterization of the Cu_2O – ZnO junction, determining its ability to serve as a p-n-junction, and gain insight for coexistent systems in general.

In the case of a formation of a functional p-n-junction with results near the theoretical value, the way to research cost-efficient manufacturing processes, and designs of gates based on these materials would be opened. Additionally, different devices, such as solar panels, could be realized, too. Further enhancing the performance and simplifying the manufacturing process of functioning coexisting p-n-junctions could result in a significant shift in the semiconductor industry, at least for high-energy applications. In the case of dismissing Cu_2O – ZnO as a p-n-junction, research conducted worldwide would have to shift its approach because it has been shown that the material cannot be efficiently used to create these junctions. Nonetheless, the principles found within this project are fundamental and can be extended to new systems.

1.2.5. Outline of the Thesis

In this thesis, the relevant theory will be introduced and discussed in section 2. First, a few mathematical constructs will be stated, used later in the thesis. Second, classical thermodynamics will be used to determine the vital Gibbs free energy. Third, the formation of native defects and their implications on the respective oxide are discussed, before the theory for semiconductors will be stated, introducing the band gap, carrier concentration, and thermoelectricity. Fourth, the p-n-junction is under scrutiny, shining a light on the difference between homojunctions and heterojunctions, and introducing the concept of rectification. Finally, system specific theory, such as Gibbs free energy of formation for Cu_2O and ZnO are stated, before a literature review of the current state of research on copper oxide based p-n-junctions is given. In section 3, the synthesis methods and experiments conducted during this

1. Introduction

M.Sc. program will be stated, and the results are shown in section 4. This includes sol-gel synthesis, pellet manufacturing, thin film deposition by PLD, TEM sample preparation and observations, and DFT calculations. Finally, in section 5, the results are discussed, and a conclusion is drawn in section 6 before an outlook to future experiments is given.

2. Theory and Literature Review

The studies of semiconductor include several topics. First, the theory to discuss crystals will be introduced, enabling the description of CuO, Cu_2O, and ZnO. Second, thermodynamics will be reviewed followed by defect chemistry of the ZnO and Cu_2O. Fourth, semiconductors will be introduced including the bandgap and intrinsic carrier concentration before, fifth, the p-n-junction is discussed in more detail, emphasizing the difference between homojunctions and heterojunctions. The TEM and DFT will be introduced, stating the most important principles of each. Finally, the connection to Cu_2O – ZnO heterojunctions is stated, including thermodynamic considerations and Cu_2O-based p-n-junctions.

2.1. Real Space, Reciprocal Space, and the Brillouin Zone

Investigating a subject with physical chemistry, statistical mechanics, solid-state physics, DFT, or TEM often leads to the concept of two different spaces, real space, and reciprocal space. Moreover, studying crystals leads to the concept of the Brillouin zone. These mathematical concepts help to describe the properties of the system and take advantage of symmetry and motif of crystals.

2.1.1. Lattice Properties of Crystals

Any crystal structure can be described by specifying a repeating element and its translational periodicity. The repeating element, usually many atoms, is replaced by a lattice point, and all lattice points have the same atomic environment. Atoms and lattice points situated on corners, faces and edges are shared with neighboring cells [9, 11, 76, 77].

The unit cell is the smallest building block. The elementary unit of volume, the unit cell, can describe the entire (perfect) lattice by being repeated in all three directions. It is defined either by three non-planar lattice vectors ($\vec{a}, \vec{b}$, and $\vec{c}$), or by the length of these vectors and angle between them. The origin of the unit cell can be described by a translational vector $\vec{r}_g = u\vec{a} + v\vec{b} + w\vec{c}$, and the atom position within the unit cell $\vec{r}_k = x\vec{a} + y\vec{b} + z\vec{c}$. There are seven different axial systems used [9, 76]. 14 different Bravais lattices can describe the point lattices. Crystals can further be classified by symmetry, without taking into account their translational symmetry. There are 32 point groups or crystal classes. Symmetry elements can utilize

11

translational elements, e.g., glide (reflection and translation within the unit cell) and screw axis (turn and translation within the unit cell). If one takes into account the classification, 230 different space groups exist [76].
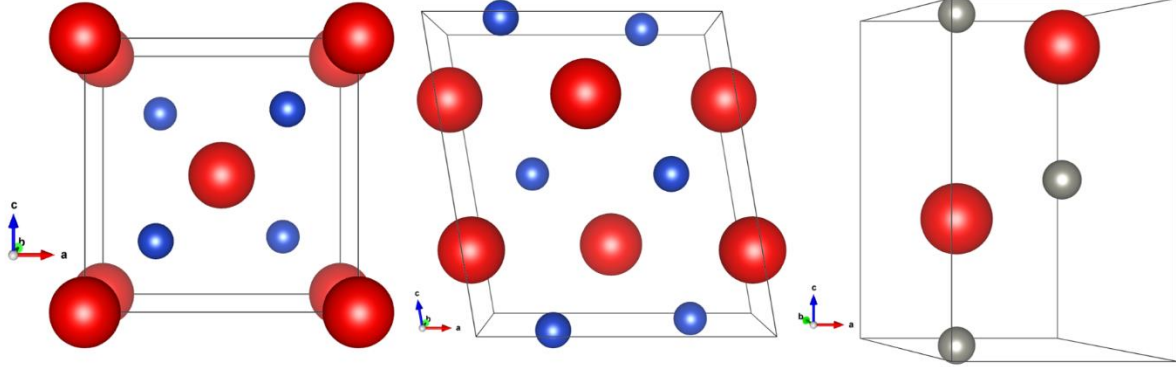

Figure 4: The crystal structures of the three crucial oxides in this thesis. The structures are Cu₂O, CuO, and ZnO (from left to right). The structures are created by using the lattice parameters stated below and the x, y, z values in Table 1. Moreover, the oxygen (red) is larger than the copper (blue) or zinc (grey) due to the ionic radii type used.

The Cu_2O has the space group $Pn\bar{3}m$ with a lattice parameters $|\vec{a}| = |\vec{b}| = |\vec{c}| = 0.427$ nm. The other common copper oxide phase, CuO, has the monoclinic space group C2/c (full name C1 2/c 1). The lattice parameters are: $|\vec{a}| = 0.468$ nm, $|\vec{b}| = 0.342$ nm, $|\vec{c}| = 0.513$ nm, and $\beta = 99.54°$ [78]. The third important oxide is the zinc oxide, with the space group $P6_3mc$ and the lattice parameters $|\vec{a}| = |\vec{b}| = 0.325$ nm, $|\vec{c}| = 0.522$ nm, and $\gamma = 120°$. The x, y, and z values of the atoms are shown in Table 1.

2.1.2. Reciprocal Space

The reciprocal space and the real space are connected through a simple relation: $\vec{a}^*\vec{a} = 1$ (same for $\vec{b}$ and $\vec{c}$). Additionally, the atom position within the unit cell, as described above, $\vec{r}_k = m\vec{a} + n\vec{b} + p\vec{c}$, with $\vec{a}$, $\vec{b}$, and $\vec{c}$ the primitive unit cell translational vectors in real space, and m, n, and p integers. For the reciprocal space $\vec{r}^* = m\vec{a}^* + n\vec{b}^* + p\vec{c}^*$ with $\vec{a}^* = \frac{\vec{b}\times\vec{c}}{V_{cell}}$, and $V_{Cell} = \vec{a} \cdot \vec{b} \times \vec{c}$ (similar for $\vec{b}$ and $\vec{c}$). In no way does this state that $\vec{a}$, $\vec{b}$, and $\vec{c}$ are orthogonal [9, 76]. The real lattice vector and the corresponding reciprocal lattice vectors are parallel only in the case of orthogonal systems. A reciprocal lattice is a convenient way of visualizing diffraction.

Table 1: The x, y, and z values for the atom position within the unit cell $\vec{r}_k$ for cuprous oxide, cupric oxide and zinc oxide.

Cuprous Oxide				Cupric Oxide			
Atom:	x	y	z	Atom:	x	y	z
O	0.00	0.00	0.00	O	0.00	-0.58	0.00
Cu	0.25	0.25	0.25	Zn	0.25	0.25	0.00

Zinc Oxide			
Atom:	x	y	z
O	0.3333	0.6667	0.3824
Zn	0.3333	0.6667	0.0000

2.1.3. Brillouin Zone

The Brillouin zone is the reciprocal unit cell, with $\vec{k}$ a wavevector. The first Brillouin zone is set around the wavevector $\vec{k} = \vec{0}$, meaning it goes from no momentum to its boundaries, $-\frac{\pi}{a}\vec{e}$ and $\frac{\pi}{a}\vec{e}$ in each direction (with a the length of the respective translational vectors in the direction $\vec{e}$). Hence, it can be defined that the first Brillouin zone encloses all $\vec{k}$ points closer to $\vec{0}$ than any other reciprocal lattice point [11]. The second Brillouin zone would be the $\vec{k}$ points with $\vec{0}$ as the second closest reciprocal lattice point. Every Brillouin zone has exactly the same volume as the other ones. Finally, the Brillouin zone has inversion symmetry because all fundamental lattice types show symmetry under inversion operation in any lattice point [9, 11].

2.2. Classical Thermodynamics

Classical thermodynamics determines the phase formed under given conditions. It does not indicate how the transformation from one to the other phase occurs, or if the reaction occurs due to kinetics. Below the essential points about thermodynamics as utilized in the experimental section are stated. A more extensive take on classical thermodynamics is given in Appendix A.

2.2.1. Thermodynamic Potential Functions

While only the internal energy has been used as a function of state with the dimension energy at the beginning of Appendix A, others can be created by adding any other functions of state with dimension energy. Four of those known as thermodynamic potential functions have a significant role in determining the equilibrium states under different constraints [79]. The first is the internal energy, U, describing the energy of a system [79]. The second is the enthalpy, H.

For reversible isobaric processes the enthalpy describes the heat absorbed by the system [10]. The third is the Helmholtz free energy. A positive change in the Helmholtz free energy represents reversible work done on the system by the surrounding, and a negative change describes reversible work done by the system on the surrounding. Finally, the Gibbs free energy remains constant for isothermal-isobaric processes.

The mathematical descriptions of these four potential functions reveal their usefulness in different experimental setups, i.e., with different constraints. Equations (1) – (4) show the potential functions for systems with two degrees of freedom and the corresponding derivatives.

The internal energy : $\qquad$ U $\qquad$ $dU = TdS - pdV$ $\qquad$ (1)

The enthalpy: $\qquad$ $H = U + pV$ $\qquad$ $dH = TdS + Vdp$ $\qquad$ (2)

The Helmholtz energy: $\qquad$ $F = U - TS$ $\qquad$ $dF = -SdT - pdV$ $\qquad$ (3)

The Gibbs energy: $\qquad$ $G = U - TS + pV$ $\qquad$ $dG = VdP - SdT$ $\qquad$ (4)

Their usefulness and differences can best be seen in their differential form. Each of the differential potential functions has two terms corresponding to their respective degrees of freedom. The independent variables are as follows: $U = U(S, V); H = H(S, p); F = F(T, V); G = G(p, T)$, where p is the pressure, V the volume, T the temperature and S the entropy. If any of these potentials are known in terms of their variables, the information about the system is complete, and any parameter of state can be calculated. The function of state useful for the experiments described in section 3 is the Gibbs energy because, during these experiments, the temperature and pressure can be set and held constant.

2.2.2. The Gibbs Energy

The determination of whether a reaction occurs spontaneously can be achieved by evaluating dS for isolated systems, or dF and dG for non-isolated systems [80]. While the Helmholtz energy is useful for systems with constant volume and temperature, the Gibbs energy is useful in determining whether the reaction is spontaneous under constant pressure and temperature. By evaluating

$$dU \leq TdS - pdV \qquad (5)$$

where the equality holds for reversible reactions, the following can be expressed under constant T and p,

$$d(U - TS + pV) \leq 0. \qquad (6)$$

By using the definition of $G = U - TS + pV$ (eq. (4)) it follows, that

$$dG \leq 0 \qquad (7)$$

for spontaneous processes. Equilibrium is reached when $dG = 0$. Integrating the exact differential $dG = -SdT + Vdp$ at constant temperature $(T_1 = T_2)$ yields

$$\Delta G = -\underbrace{\int_{T_1}^{T_2} SdT}_{=0} + \int_{p_1}^{p_2} Vdp = RT\ln\frac{p_2}{p_1} \qquad (8)$$

for one mole of an ideal gas. By standardizing the pressure to 1 atm, and adding $\Delta G°(T)$,

$$\Delta G = \Delta G° + RT\ln\frac{p_2}{1\,\text{atm}} \qquad (9)$$

where ΔG is the difference in Gibbs energy between initial and final state, $\Delta G°$ the molar Gibbs energy difference at temperature T and one bar pressure. In equilibrium $\Delta G = 0$ ($\Delta G = \int_{S_1}^{S_2} dG = 0$, where S_1 is the initial and S_2 the final state),

$$\Delta G° = -RT\ln\frac{p_2}{1\,\text{atm}} \qquad (10)$$

Furthermore, in equilibrium, the equilibrium coefficient K can be expressed using the partial pressure. Assuming low pressures and ideal gases, the activity, $a_i = \frac{p_i}{p°}$, where p_i the partial pressure of species i with activity a_i and $p°$ the reference pressure [79, 80]. For a reaction,

$$\Delta G° = -RT\ln K. \qquad (11)$$

The difference in Gibbs energy can be expressed by $\Delta G = \Delta H - T\Delta S$. This states the balance between increasing the entropy and decreasing the enthalpy in a system with constant pressure and temperature [80]. The enthalpy dominates the low-temperature range, and the entropy governs the high-temperature range. Another way to derived $\Delta G°$ is given in Appendix A.

As an example to evaluate the $\Delta G°$ the reaction

$$4\text{Cu} + \text{O}_2(g) = 2\text{Cu}_2\text{O} \qquad (12)$$

is evaluated. At $T = 298.15$ K, the corresponding $\log K$ is $\log K = 25.908$ [81]. In turn, the oxygen partial pressure can be expressed in terms of the partial pressure as $\frac{p_{\text{O}_2}}{p°} = 10^{-25.908}$. Hence, the $\Delta G° = -147.883$ kJ/mol compare to -146 to -149 kJ/mol found in literature [82, 83].

2.3. Native Defects in ZnO and Cu₂O

Native or intrinsic defects are materials imperfections involving an additional number of a constituent element, or lack thereof. Vacancies describe a missing atom on a regular atom site; interstitials mark additional atom on interstices in the lattice, and anti-sites point to atoms on the wrong site, e.g., Zn on an O site [50, 84]. The Kröger-Vink (K-V) notation can be used to
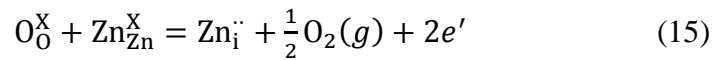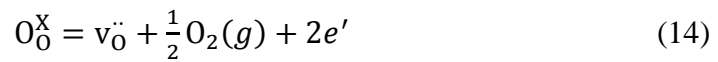
identify and describe the nature of the defect quickly. Using A_S^C for a defect, and $[A_S^C]$ for the concentration of said defect, the type (either atom-type or vacancy) can be stated in A, the site is denoted by S, and the effective charge in C by using $\cdot$ for a positive, and $'$ for negative effective charges [85]. The concentration of each defect depends on its formation energy (E_f) [9, 86]:

$$c = N_{\text{Sites}} \exp\left(-\frac{E_f}{k_{\text{B}}T}\right) \tag{13}$$

where N_{Sites} is the number of sites per unit volume, the particular defect can occupy. Hence, the higher the formation energy of each defect, the lower the concentration of said defect [50]. The ground state energy of each defect can be calculated using DFT [87, 88]. However, its formation energy depends on the growth and annealing condition. This includes the availability of the species, expressed in the chemical potential. Furthermore, the energy of formation of a charged defect depends on the Fermi level. The two materials at hand will be discussed separately in order to determine the implications of the defect on the materials.

2.3.1. Native Defects in ZnO

For ZnO, it is essential to understand the formation of defects, as they affect the electronic and optical properties. Native defects are considered significant in ZnO because the oxide shows high levels of unintentional n-type conductivity. Possible native defects resulting in an n-type ZnO can be oxygen vacancies ($v_O^{\cdot\cdot}$) or zinc interstitials ($Zn_i^{\cdot\cdot}$). The formation of the defects can be expressed by

$$O_O^X = v_O^{\cdot\cdot} + \frac{1}{2}O_2(g) + 2e' \tag{14}$$

$$O_O^X + Zn_{Zn}^X = Zn_i^{\cdot\cdot} + \frac{1}{2}O_2(g) + 2e' \tag{15}$$

where O_O^X is O on O sites, Zn_{Zn}^X is Zn on Zn sites, $Zn_i^{\cdot\cdot}$ a doubly charged Zn on an interstitial site, $v_O^{\cdot\cdot}$ a zinc vacancy, $O_2(g)$ oxygen gas, and e' electrons. The law of mass action leads to the two equilibrium constants, k_1 and k_2, as

$$k_1 = [v_O^{\cdot\cdot}]n^2 p_{O_2}^{\frac{1}{2}} \tag{16}$$

$$k_2 = [Zn_i^{\cdot\cdot}]n^2 p_{O_2}^{\frac{1}{2}} \tag{17}$$

with n the electron concentration and p_{O_2} the oxygen partial pressure. Assuming that the electrons and the two defects compensate each other perfectly to have an electrically neutral material as in $n = 2[Zn_i^{\cdot\cdot}] + 2[v_O^{\cdot\cdot}]$. This enables the determination of the relationship between

the electron concentration n and the oxygen partial pressure. First, the oxygen vacancy can be expressed by $[v_O^{\cdot\cdot}] = \frac{1}{2}(n - 2[Zn_i^{\cdot\cdot}])$. The eq. (16) can be rearranged to

$$p_{O_2}^{-\frac{1}{2}} = \frac{n^2}{2k_1}(n - 2[Zn_i^{\cdot\cdot}]). \tag{18}$$

By subsequently substituting eq. (17) in to eq. (18) yields the dependency

$$p_{O_2}^{-\frac{1}{2}} = \frac{n^2}{2k_1}\left(n - 2\frac{k_2}{n^2}p_{O_2}^{-\frac{1}{2}}\right). \tag{19}$$

This can be solved to get the dependency of the oxygen partial pressure to the electron concentration,

$$p_{O_2}^{\frac{1}{4}} = \sqrt{\frac{1}{2n^3}(k_1 + k_2)}. \tag{20}$$

Utilizing the conductivity, described in section 2.4.3, the conductivity can be expressed as a function of the oxygen partial pressure

$$\sigma(p_{O_2}) = e\mu \cdot \sqrt[3]{\frac{k_1 + k_2}{2}} p_{O_2}^{-\frac{1}{6}}. \tag{21}$$

The availability of oxygen during formation determines the formation energy of an oxygen vacancy. For example:

$$E_f(v_O^q) - E_{tot}(ZnO) + \mu_O + q(E_F + E_{VBM}) \tag{22}$$

where $E_{tot}(v_O^q)$ is the total energy of a supercell with the oxygen vacancy with charge q, $E_{tot}(ZnO)$ is the total energy of the same supercell with a perfect ZnO crystal structure, μ_O the chemical potential of oxygen, and $q(E_F + E_{VBM})$ the energy of the charge q, depending on the Fermi level E_F and the valence edge energy E_{VBM} [50]. The oxygen vacancy has been thought of as the origin of the n-type ZnO. However, DFT calculations demonstrated that these vacancies are deep donors, rather than shallow donors that would contribute to the n-type conductivity [50]. Nonetheless, these defects could be relevant in compensating p-type ZnO.

Zinc interstitial can occupy the tetrahedral and octahedral sites in the ZnO wurtzite structure. The tetrahedral site would put the Zn atom in the proximity of one Zn and one O atom, with a distance of ~$0.833d_O$ (where d_O is the Zn $-$ O distance). The octahedral site has an environment of three Zn and three O atoms as closest neighbors with a distance of ~$1.07d_O$.
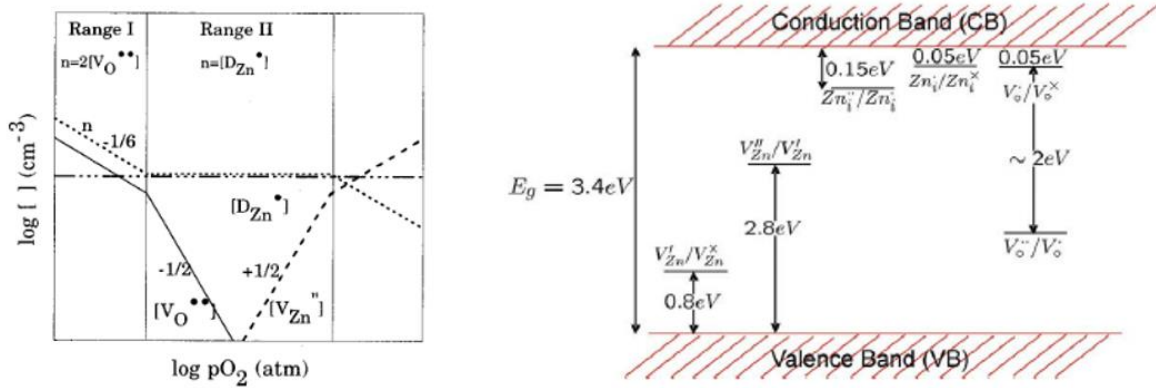
Figure 5: On the left the Brouwer diagram of defects in ZnO. Range I is dominated by oxygen vacancies, representing an oxygen deficient situation. Range II shows a range of oxygen partial pressures dominated by donor charged impurity on a zinc site. However, instead of $[D_{Zn}^{\cdot}]$ one can imagine $[OH_O^{\cdot}]$ with a similar effect if the concentration of $OH_O^{\cdot}$ is fixed. The unlabeled region would be dominated by zinc vacancies, however, it is incorrect as there is no charge compensating species emerging with the zinc vacancies [89] (as found in [89]). On the right is the energy level of native defects [90] (as found in [90]) .

The geometric conditions suggest that Zn takes the octahedral site, which has been previously observed [50, 86, 91]. Moreover, the zinc interstitial forms an a_1 state with two electrons above the conduction band edge. The two electrons, which will transfer to conduction band states, stabilize this defect. Hence, Zn interstitials donate two electrons to the conduction band and act as shallow donors [50]. Zinc vacancies, the last native defect in ZnO with low formation energy, are deep acceptors. They can act as compensating defects in n-type samples [50]. While the defects $v_O^{\cdot\cdot}$, $Zn_i^{\cdot\cdot}$, and v_{Zn}'' have the lowest formation energies (together with interstitial oxygen), only v_{Zn}'' exists in modest concentrations under equilibrium conditions according to DFT calculations [50, 86, 91]. Both $v_O^{\cdot\cdot}$ and $Zn_i^{\cdot\cdot}$ have too high formation energies under n-type conditions to appear in significant amounts. This suggests that neither of the two is the reason for the n-type conductivity of ZnO. Instead, it has been suggested that hydrogen, binding to oxygen is the cause of the defect [92, 93]. However, the reasons for the n-type ZnO remains a point of discussion. Whatever the dominant reason may be, it is evident that native defects compensated by electrons, such as $Zn_i^{\cdot\cdot}$ and $v_O^{\cdot\cdot}$, have much lower formation energies under semi-insulating conditions, and push the material towards an n-type material. Hydrogen bonded to oxygen on oxygen site, $OH_O^{\cdot}$, adds to that push. Hence, donor type defects are favored in ZnO.

Table 2: The energies for the formation of the defects under different conditions are shown below. For the n-type condition, the Fermi energy (E_F) has the value of the gap (E_g), and for the semi-insulating case, the Fermi level was placed in the middle of the gap.

Defect	n-Type Conditions [eV] $E_F = E_g$	Semi-insulating Conditions [eV] $E_F = E_g/2$	Source
$Zn_i^{\cdot\cdot}$	6.98	3.55	[91]
v_{Zn}''	2.97	6.40	[91]
$v_O^{\cdot\cdot}$	-	4.53	[91]
O_i''	5.14	8.57	[91]

2.3.2. Native Defects in Cu₂O

On the other side of a possible junction is Cu₂O, a p-type semiconductor. Copper vacancies are native defects in Cu₂O [74, 94]. The formation of vacancies can be described by

$$\frac{1}{4}O_2 \rightleftarrows \frac{1}{2}O_O^X + v_{Cu}' + h^{\cdot} \tag{23}$$

with O_O^X a neutral anion on anion site, v_{Cu}' a singly ionized cation vacancy, and $h^{\cdot}$ an electron-hole [94]. Moreover, doubly negatively charged oxygen interstitials are the dominant defect on the oxygen sub-lattice within the Cu₂O [44, 95], with

$$\frac{1}{2}O_2 \rightleftarrows O_i'' + 2h^{\cdot} \tag{24}$$

where O_i'' is the doubly charged oxygen interstitials.

The law of mass action leads to the two equilibrium constants, k_3 and k_4,

$$k_3 = [v_{Cu}']p \cdot p_{O_2}^{-\frac{1}{4}} \tag{25}$$

$$k_4 = [O_i'']p^2 \cdot p_{O_2}^{-\frac{1}{2}} \tag{26}$$

Assuming that the electron holes and the two defects v_{Cu}' and O_i'' compensate each other according to the neutrality condition $p = [v_{Cu}'] + 2[O_i'']$, the relation between the hole concentration p and the oxygen partial pressure can be derived [95]. Starting by substituting the copper vacancies by $[v_{Cu}'] = p - 2[O_i'']$, the oxygen partial pressure in eq. (25) can be expresses as

$$p_{O_2}^{\frac{1}{4}} = \frac{1}{k_3}(p^2 - 2[O_i'']p) \tag{27}$$

and, using eq. (26), the concentration of defects can be expressed as a function of p

$$p_{O_2}^{\frac{1}{4}} = \frac{1}{k_3}\left(p^2 - 2 \cdot \frac{k_4 p_{O_2}^{\frac{1}{2}}}{p}\right). \tag{28}$$

This can be simplified to

2. Theory and Literature Review

$$2p_{O_2}^{\frac{1}{4}} = -\frac{pk_3}{2k_4} + \sqrt{\left(\frac{pk_3}{2k_4}\right)^2 + \frac{2p^3}{k_4}}. \tag{29}$$

Using the conductivity, as shown in section 2.4.3, it can be related to the oxygen partial pressure by,

$$2p_{O_2}^{\frac{1}{4}} = -\frac{k_3}{2k_4}\frac{\sigma}{e\mu} + \sqrt{\left(\frac{k_3}{2k_4}\frac{\sigma}{e\mu}\right)^2 + \frac{2}{k_4}\left(\frac{\sigma}{e\mu}\right)^3}. \tag{30}$$

Moreover, the two constants can be calculated by using the Gibbs free energy described in section 2.2.2. The Gibbs free energy can be used to describe the equilibrium constants by

$$K_i(T) = \exp\left[\frac{\Delta G_i}{k_B T}\right] \tag{31}$$

where i indicates the defect species. Using the differential equation stated in eq. (4), and substituting the differential in eq. (2) into the equation leads to

$$\Delta G_i = \Delta H_i - T\Delta S_i \tag{32}$$

where ΔG_i, ΔH_i, and ΔS_i are the Gibbs free energy, the enthalpy and the entropy for the formation of either a charged copper vacancy and a hole, or for a charged oxygen interstitial and two holes. For the reaction $\frac{1}{4}O_2(g) \rightleftarrows \frac{1}{2}O_O^X + v_{Cu}' + h^{\cdot}$ the values

$$\Delta H_{v_{Cu}} = 1.8 \pm 0.2 \text{ eV} \tag{33}$$

$$\Delta S_{v_{Cu}} = (9 \pm 0.1) \times 10^{-3}\frac{\text{eV}}{\text{K}} \tag{34}$$

have been shown for $900 \text{ K} < T < 1250 \text{ K}$ [95]. Moreover, the reaction $\frac{1}{2}O_2 \rightleftarrows O_i'' + 2h^{\cdot}$ the values

$$\Delta H_{O_i} = 3.1 \pm 0.1 \text{ eV} \tag{35}$$

$$\Delta S_{O_i} = (14 \pm 0.2) \times 10^{-3}\frac{\text{eV}}{\text{K}} \tag{36}$$

have been determined for $900 \text{ K} < T < 1250 \text{ K}$ [95].

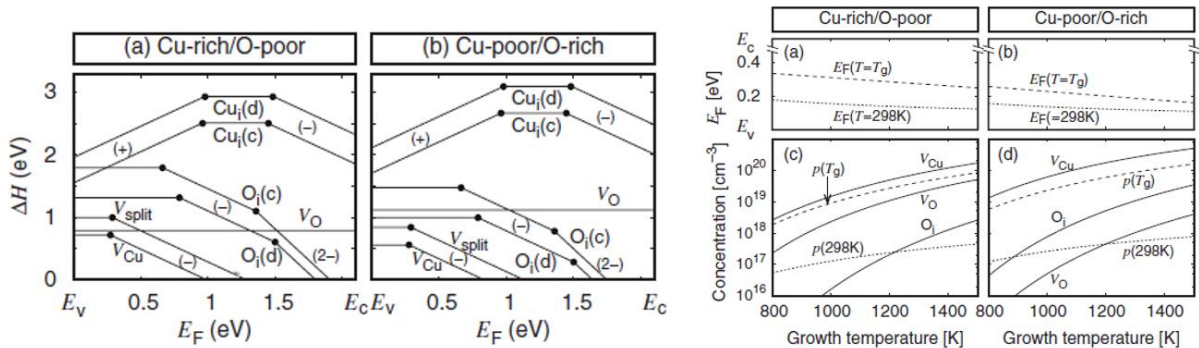Figure 6: The ΔH (eV) of defects plotted against the E_F (eV) in (a) Cu-rich or O-poor environment and (b) Cu-poor or O-rich environment. The lowest energies are shown, with the dot symbolizing ionization points [96]. Furthermore, on the right, the E_F plotted against the growing temperature in Kelvin, as well as the concentrations of defects plotted against the temperature in Kelvin [96] (as found in [96]).

2.4. Semiconductors

In a simplified band scheme of a semiconductor, as shown in Figure 7, the valence band is filled, and an energy gap E_{Gap} is above it before the empty conduction band follows. The lowest point in the conduction band is the conduction band edge, and the highest point in the valence band is called valence band edge. The definition of the band gap is the difference between the two [9].
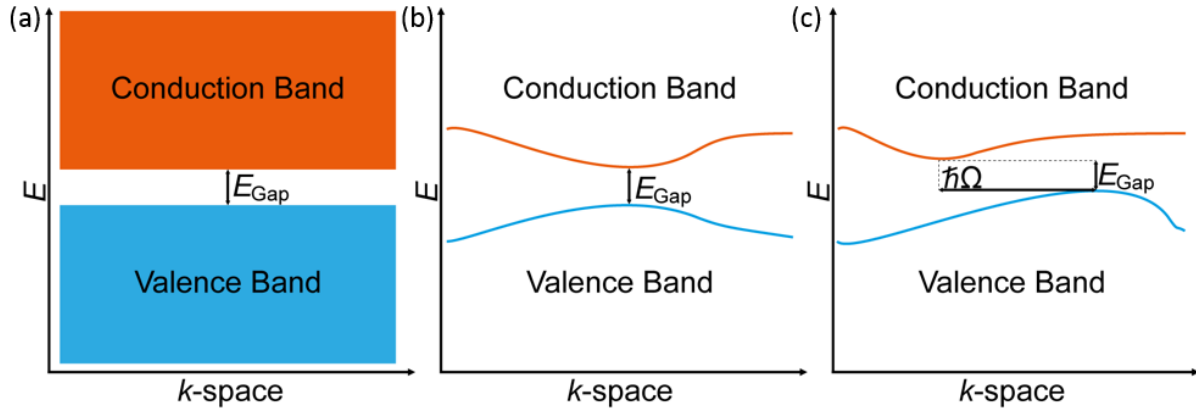

Figure 7: (a) A simplified band structure, including the filled valence band in the bottom, followed by the band gap, and finally the unoccupied conduction band. (b) An example of a direct band gap, where valence band and conduction band edges are located at the same $\vec{k}$. (c) An exemplary depiction of the indirect band gap, with valence band edge and conduction band edge at different $\vec{k}$.

2.4.1. The Band Gap

A band gap is the energy an electron has to overcome to go from the valence band into the conduction band. As such, the intrinsic conductivity and intrinsic carrier concentration are dominated by $\frac{E_{\text{Gap}}}{k_{\text{B}}T}$ [9]. A low temperature generally leads to a low concentration and conductivity. There are two distinct kind of band gaps. The first is the direct band gap, where valence band edge and conduction band edge are aligned at the same k-vector ($\vec{k}$) in reciprocal space. Hence, the band gap is $E_{\text{Gap}} = \hbar\omega_{\text{Gap}}$, with absorption frequency ω_{Gap}, and $\hbar$ the reduced Planck's constant [9].

The second kind of band gap is the indirect band gap. Characteristic of this kind of band gap is that not only E_{Gap} has to be overcome, but also a wave vector $\vec{k}$. In other words, the valence band edge and conduction band edge are not at the same $\vec{k}$ [9], as shown in Figure 7. A phonon of energy $\hbar\Omega$ is emitted in this process, leading to the required minimal energy to overcome the gap of

$$\hbar\omega = E_{\text{Gap}} + \hbar\Omega. \tag{37}$$

The phonon has almost no energy, but almost all the momentum needed to change from the valence band edge to the conduction band edge. The low energy ensures that the process can occur at low energy; however, the momentum transfer makes radiative recombination in indirect semiconductors slow [9]. Moreover, the reverse effect, used in photovoltaics, light absorption, is dependent on the availability of phonons in the material. Light can penetrate indirect semiconductors much farther than direct semiconductors because the incoming photon barely carries any momentum with it. Hence, a phonon within the material and an incoming photon are needed to overcome the band gap of an indirect semiconductor [9, 11].

This implies two important principles: First, indirect semiconductor solar cells must be much thicker (typically hundreds of microns) than direct semiconductor solar cells (typically thin films). The thickness increases the chance of phonons and photons interacting [9, 11]. Second, the temperature dependency of the efficiency of indirect semiconductors is higher than the one of direct semiconductors because the number of phonons increases with temperature [9, 11].

2.4.2. Intrinsic Carrier Concentration

To obtain the carrier concentration, a single parabolic band edge is considered. The chemical potential μ helps to express the number of electrons that are excited to the conduction band at temperature T [9]. For simplicity, $E - \mu \gg k_{\text{B}}T$ is assumed for the conduction band, where E is the energy of the band edge. Hence, the Fermi-Dirac distribution becomes

$$f_e(\vec{E}) \approx \exp\left[\frac{\vec{\mu} - \vec{E}}{k_{\text{B}}T}\right] \tag{38}$$

where f_e is the probability that a conduction electron orbital is occupied. This is valid for $f_e \ll 1$ [9].

The energy of such an electron in the conduction band can be expressed in terms of energy of the conduction band edge, E_C, plus the energy created by being away from the edge [9]

$$\vec{E}_e = \vec{E}_C + \frac{\hbar^2 \vec{E}^2}{2m_e}. \tag{39}$$

The effective mass, m_e, here is the mass of an electron. The density of states at the energy $\vec{E}$ is [9]

$$D_e(\vec{E}) = \frac{1}{2\pi^2}\left(\frac{2m_e}{\hbar}\right)^{\frac{3}{2}}(\vec{E} - \vec{E}_C)^{\frac{1}{2}}. \tag{40}$$

The corresponding electron density in the conduction band is

$$n = \int_{E_C}^{\infty} D_e(\vec{E}) f_e(\vec{E}) d\vec{E} = \frac{1}{2\pi^2} \left(\frac{2m_e}{\hbar}\right)^{\frac{3}{2}} \exp\left(\frac{-\vec{\mu}}{k_B T}\right) \int_{E_C}^{\infty} (\vec{E} - \vec{E}_C)^{\frac{1}{2}} \exp\left(\frac{-\vec{E}}{k_B T}\right) d\vec{E} \quad (41)$$

which yields

$$n = 2 \left(\frac{m_e k_B T}{2\pi\hbar^2}\right)^{\frac{3}{2}} \exp\left[\frac{\vec{\mu} - \vec{E}_C}{k_B T}\right]. \quad (42)$$

The distribution function for holes can be expressed with the electron distribution function: $f_h = 1 - f_e$ [9]. Consequently,

$$f_h(\vec{E}) = 1 - \frac{1}{\exp\left[\frac{\vec{E} - \vec{\mu}}{k_B T}\right] + 1} = \frac{1}{\exp\left[\frac{\vec{\mu} - \vec{E}}{k_B T}\right] + 1} \approx \exp\left[\frac{\vec{E} - \vec{\mu}}{k_B T}\right] \quad (43)$$

with $E - \mu \gg k_B T$. Corresponding to the case of the electron, this can yield a density of hole states [9]

$$D_h(\vec{E}) = \frac{1}{2\pi^2} \left(\frac{2m_h}{\hbar}\right)^{\frac{3}{2}} (\vec{E}_V - \vec{E})^{\frac{1}{2}} \quad (44)$$

with the energy of the valence band edge, $\vec{E}_V$. Moreover, the hole density is [9]

$$p = \int_{-\infty}^{E_V} D_h(\vec{E}) f_h(\vec{E}) d\vec{E} = 2 \left(\frac{m_h k_B T}{2\pi\hbar^2}\right)^{\frac{3}{2}} \exp\left[\frac{\vec{E}_V - \vec{\mu}}{k_B T}\right]. \quad (45)$$

By multiplying the electron density, eq. (42), with the hole density, eq. (45), the equilibrium relation with an energy $\vec{E}_{Gap} = \vec{E}_C - \vec{E}_V$ is obtained [9]

$$np = 4 \left(\frac{k_B T}{2\pi\hbar^2}\right)^3 (m_e m_h)^{\frac{3}{2}} \exp\left[\frac{-\vec{E}_{Gap}}{k_B T}\right]. \quad (46)$$

By only assuming $E - \mu \gg k_B T$, the eq. (46) is valid for intrinsic and doped materials. Additionally, the product np is constant and independent of impurity levels [9].

For intrinsic semiconductors, n_i is equal to p_i, where i denotes the intrinsic property [9], as in

$$n_i = p_i = 2 \left(\frac{k_B T}{2\pi\hbar^2}\right)^{\frac{3}{2}} (m_e m_h)^{\frac{3}{4}} \exp\left[\frac{-\vec{E}_{Gap}}{2k_B T}\right]. \quad (47)$$

The exponential dependency on $\left[\frac{-\vec{E}_{Gap}}{2k_B T}\right]$ is clearly visible. Moreover, the Fermi level, or chemical potential of the charge carrier can be determined from the edge of the valence band by

$$\exp\left[\frac{2\vec{\mu}}{k_B T}\right] = \left(\frac{m_h}{m_e}\right)^{\frac{3}{2}} \exp\left[\frac{\vec{E}_{Gap}}{k_B T}\right] \quad (48)$$

leading to

$$\vec{\mu} = \frac{1}{2} \vec{E}_{Gap} + \frac{3}{4} k_B T \ln\frac{m_h}{m_e}. \quad (49)$$

If $m_h = m_e$, then the Fermi level is in the middle of the gap [9].

2.4.3. Intrinsic Mobility

Defined as the magnitude of the drift velocity per unit electric field, $\vec{\mu}_M = \frac{|v|}{\vec{E}_{\text{Field}}}$, the mobility, $\vec{\mu}_M$, is positive for both electrons and holes [9]. Nonetheless, their respective drift velocities are opposite in the same field. The sum of the electron and hole contributions defines the electrical conductivity, σ [9]

$$\sigma = (ne\mu_{M,e} + pe\mu_{M,p}). \tag{50}$$

The mobility of both holes and electrons depend on the temperature by a power law [9]. In the intrinsic region, the conductivity has a dominating exponential dependency on the temperature because of the carrier concentration as shown above.

2.5. The p-n-Junction

The importance of p-n-junctions is well established. Hence, improving them is a focal point of an entire industry, leading to impressive progress over the past few decades [4, 7, 8, 17, 97, 98]. Decreasing the size, while maintaining or even improving the lifetime and robustness of the junction is both challenging and necessary, for example for the continuous development of more powerful and faster computers. A coexistent p-n-junction has, theoretically, two advantages: it is an atomically sharp junction, and thermodynamically stable. In order to create a coexistent p-n-junction, for example with Cu_2O and ZnO, the fundamental working principles, theory and current stand of the research for p-n-junctions have to be understood. Using the Si homojunction as a straightforward and well-understood example, the steps necessary to create and understand a coexistent p-n-junction with Cu_2O and ZnO are developed below.

2.5.1. Homojunction

A classical, for example, Si-based, homojunction consists of an acceptor-doped domain (p-doped), containing mobile electrons holes in the valence band, and a donor-doped one (n-doped) containing mobile electrons in the conduction band. Examining each side by itself reveals some fundamental rules. The p-doped domain is doped with atoms having one valence electron less than Si, e.g., boron (B). This doping creates mobile electron holes and negatively

charged immobile B-atoms. Since one hole is created per B-atom, the domain remains electrically neutral (see Figure 8).
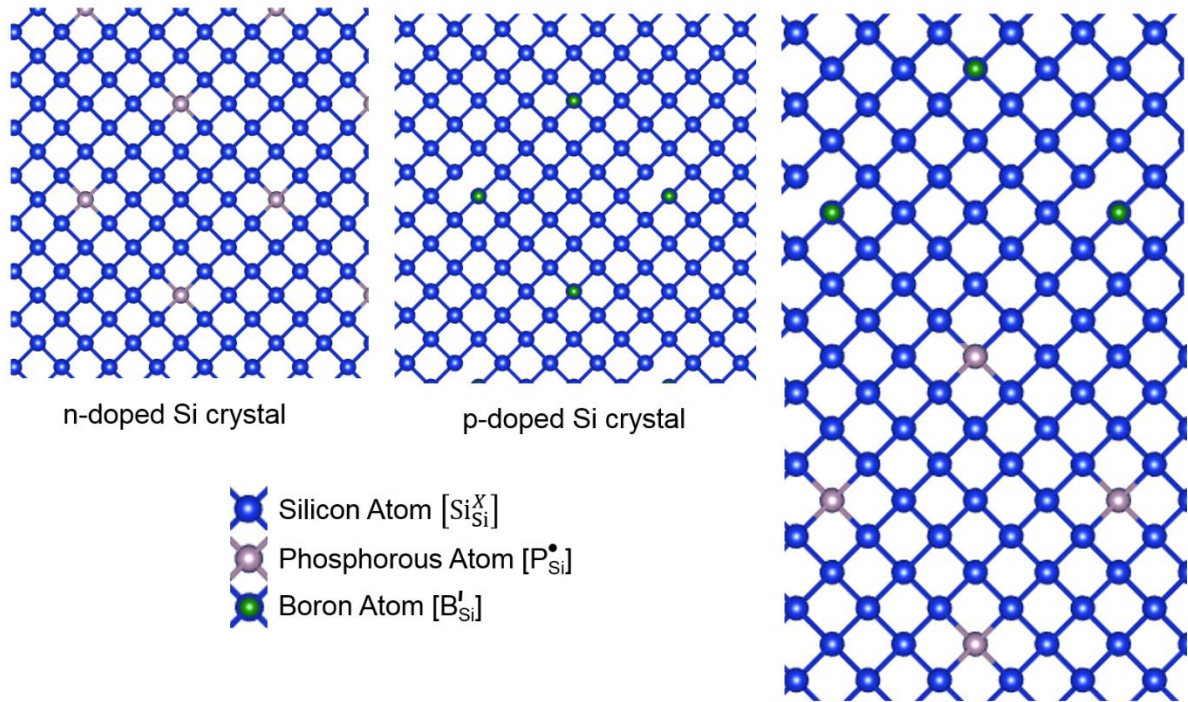

Figure 8: The crystal structure of Si, with foreign atoms in the ideal case. The n-doped Si crystal is doped with P-atoms located on regular Si sites ($P_{Si}^{\cdot}$). The p-doped Si crystal, however, is doped with B-atoms, also on regular Si sites ($B_{Si}^{\prime}$). The overall crystal structure is not changed, and forming a p-n-junction is possible without including strain on the domains in the ideal case.

The n-doped domain, however, is doped with atoms having one valence electron more than Si, e.g., phosphorous (P). This doping results in a mobile electron and a positively charged, immobile P-atom per foreign atom introduced (see Figure 7). Again, the domain remains electrically neutral overall. Both the p- and n-side have no net charge. Nonetheless, they contain highly mobile, but different, charge carriers. It is vital to have precise control over the number of dopants, as even slight variations can lead to widely different properties [99].

Formation of a p-n-Homojunction

The chemical potential μ of the n-doped system is near the top of the band gap, just below the conduction band edge, while the chemical potential of the p-doped system is near the bottom of the band gap, just above the valence band edge. The electrochemical potential balances upon formation and remains constant across a junction for both majority carriers in thermal equilibrium [11]. For holes, the chemical potential can also be expressed in a simpler form of eq. (49):

2. Theory and Literature Review

$$\tilde{\mu}_h = \mu_h^0 + k_B T \ln \rho(\vec{r}) + e\varphi(\vec{r}) \tag{51}$$

where ρ is the electron concentration, $\vec{r}$ the position within the sample, and φ the electrostatic potential, and μ_h^0 the standard electrochemical potential. Combining the two domains allows the mobile electron and holes to diffuse into the p- and n-domain, respectively. While the electrochemical potential stays constant over the junction (see Figure 9), a small flow of electrons from the n- to the p-domain occurs without any external applied field [11]. The electrons crossing the junction quickly recombine with a hole once they crossed the junction. This is expressed in a recombination current J_{nr}. A current J_{ng}, representing the electrons generated thermally in the p-region and forced to the n-region by the "built-in" field, balances J_{nr}. Consequently, with the applied external field being zero,

$$J_{nr}(0) + J_{ng}(0) = 0. \tag{52}$$

Otherwise, electrons would accumulate on one side of the barrier.
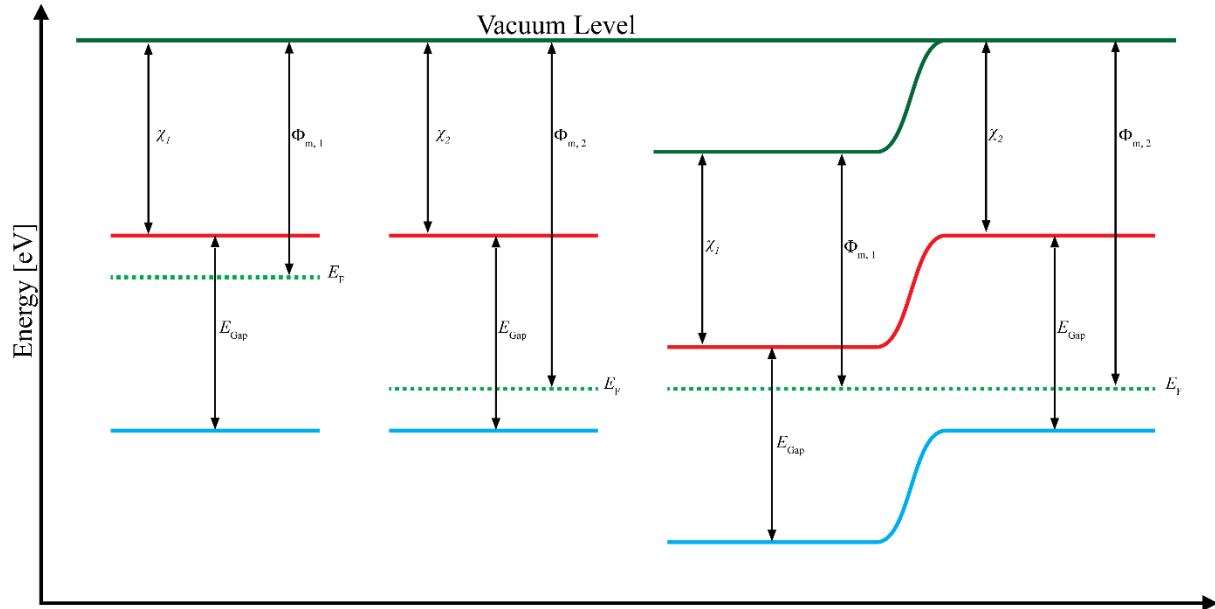
Figure 9: The band structure of n- doped and a p- doped band structure of the same semiconductor, as well as a p-n junction formed by them (e.g., n-doped and p-doped Si). The energy difference between the vacuum level and the conduction band before the formation of the junction are named χ_1 and χ_2. The energy difference between the vacuum level and the Fermi-level are named $\Phi_{m,1}$ and $\Phi_{m,2}$. E_{Gap} labels the band gap.

The immobile isovalent dopants create the "built-in" electric field across the junction within the respective domains. The built-in potential is a thermodynamic effect stemming from the difference in chemical activity of charged species on the two sides of the junction (see eq. (51)) [11, 19]. It is intuitive that the distribution of electrons and holes is not uniform within those charged domains. As the charge carriers leave their respective domain and recombine with each other in "pair-annihilation" process, a gain of E_{Gap} per recombination is generated [11].

The region around the junction has no net free charge carriers and is called depletion region or space charge region [19]. More specifically, if one moves an electron across the junction, and lets it recombine with a hole, the energy E_{Gap} is gained, but one has to pay an energy cost of $-e\Delta\varphi$. Thus, the larger the depletion region becomes (creating a large $\Delta\varphi$), the more unfavorable recombination becomes [11]. The matching of the chemical potential of the p- and n-domain in equilibrium represents the fact that the electrostatic potential compensates the drop in band energy. However, the resulting electric field across the junction is the basis of operations of diodes, transistors, and solar cells [11].

Rectification

Rectification is a property of a p-n-junction. It allows current to pass with ease in one direction, but barely in the other one. As shown in Figure 10, there are four mechanisms able to create a current. Two involve a band change (①️ and ②️), and two do not involve any band changes (③️ and ④️). In mechanism ①️, electrons can be excited from the valence band into the conduction band in the p-domain, via thermal excitation [11]. Some of the excited electrons will move on into the n-doped domain. Analogously, holes can be thermally excited from the conduction band into the valence band (process ②️), and some continue to flow to the p-domain in the valence band.
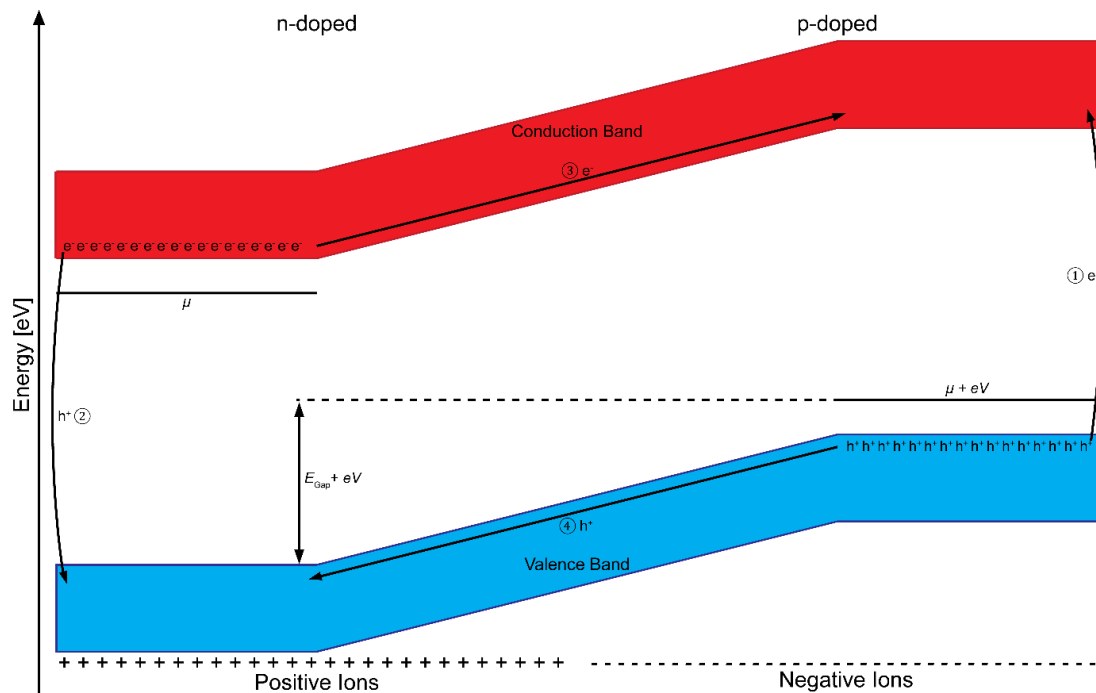

Figure 10: The band diagram of a p-n-junction with applied bias. The p-doped side is bent down (+eV is negative). Without any applied voltage the current is zero. However, for negative applied bias, the current passes easily (only process ③️ and ④️ are affected). For a positive applied voltage, the current hardly passes.

Both excitation processes result in several charge carriers excited proportional to $\exp\left(-\frac{E_{\text{Gap}}}{k_{\text{B}}T}\right)$ [9, 11], as shown in section 2.4.2. Moreover, the current generated by both charge carriers flow in both cases towards the p-domain. This results in a current of [11]

$$I_{\text{Right}} \propto \exp\left(-\frac{E_{\text{Gap}}}{k_{\text{B}}T}\right). \tag{53}$$

Furthermore, electrons can climb from the n- to the p-domain in the conduction band (process ③). Without any applied voltage, they have to climb exactly E_{Gap}. This is again a thermally activated process, and the resulting current is proportional to $\exp\left(-\frac{E_{\text{Gap}}}{k_{\text{B}}T}\right)$. A similar process is possible for holes, which have to climb down in the valence band, to get from the p-domain to the n-domain (process ④). The resulting current is again proportional to $\exp\left(-\frac{E_{\text{Gap}}}{k_{\text{B}}T}\right)$. Both charge carriers recombine after a successful climb with their counterpart [11].

Applying voltage to the junction, however, influences only specific processes. Process ① and ② are unaffected by the applied voltage [11]. Consequently, the current I_{Right} is unaffected, and eq. (53) is still valid. Meanwhile, the applied voltage leads to a change in process ③ and ④. While the direction of the current is opposite the one of processes ① and ②, with or without an applied voltage, the electron and hole have to climb $E_{\text{Gap}} + eV$ up and down, respectively [11]. The resulting current is given by

$$I_{\text{Left}} \propto \exp\left(-\frac{E_{\text{Gap}} + eV}{k_{\text{B}}T}\right) \tag{54}$$

where eV is the applied voltage [11].

The resulting total current is the summation of I_{Right} and I_{Left}, including their direction. Both currents need to have the same proportionality constant because without any applied voltage the total current needs to be zero. Thus, the total current is stated by the diode equation and is given by

$$I_{\text{Total}} = I_{\text{Right}} + I_{\text{Left}} = J_S(T)\left(\exp\left(\frac{-eV}{k_{\text{B}}T}\right) - 1\right) \tag{55}$$

with the saturation current $J_S(T) \propto \exp\left(\frac{-eV}{k_{\text{B}}T}\right)$ [11]. From the plot in Figure 11, it is easily observable that current passes easily in one direction (forward biased direction), and hardly in the other one (reverse biased direction).
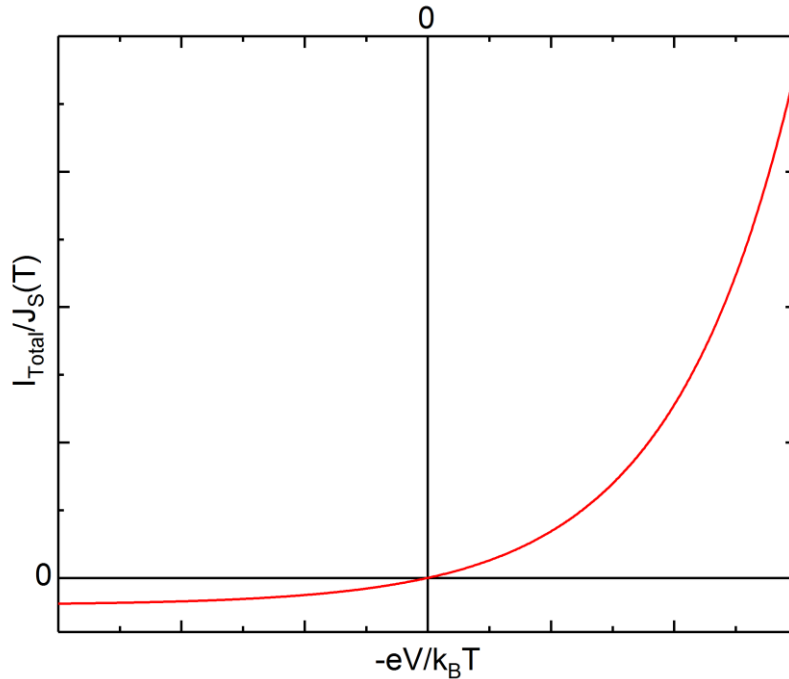
Figure 11: The rectifying behavior of a p-n-junction. It is evident that the reverse biased direction has a much higher resistivity than the forward biased direction. Additionally, it shows that the forward biased direction has slightly more resistive behavior than an ohmic device.

2.5.2. Heterojunction

Cu_2O – ZnO form a heterojunction. While the underlying fundamental working principle of a heterojunction is similar to the homojunction, there are significant differences. Heterojunctions can be grouped in many types based on their architecture [100]. A first distinction is the kind of materials used, for example, metal/semiconductor junction, or semiconductor/semiconductor junction. The first one is generally referred to as Schottky type junction [100]. However, discussing it in more detail goes beyond the purpose of this work. Semiconductor heterojunctions can be further grouped by the majority charge carriers of each semiconductor, for example, two n-type semiconductors form a n-n type heterojunction, two p-type semiconductors build a p-p type one, and one p- and one n-type semiconductors form a p-n type heterojunction [100]. Moreover, they can be built using the same chemical composition but different phases, resulting in a phase-type heterojunction; by utilizing different crystal facets of a single semiconductor, called a facet-type heterojunction; or by layer-by-layer stacking of different two dimensional materials resulting in a van der Waals type heterojunction [100-102], like Cu_2O – ZnO.

2. Theory and Literature Review

The semiconductor heterojunctions can form three different band alignments, depending on the materials, as shown in Figure 12 [100, 103]. Type I alignment consists of a semiconductor that has a valence band more positive than the second one. Additionally, the first semiconductor has a conduction band more negative than the second one ($\chi_1 + E_{Gap,1} > \chi_2 + E_{Gap,2}$ and $\chi_1 < \chi_2$) [100]. For type II alignment the conduction band of the first semiconductor is more negative than the conduction band of the second one, and the valence band is less positive for the first semiconductor than the second one ($\chi_1 + E_{Gap,1} < \chi_2 + E_{Gap,2}$ and $\chi_1 < \chi_2$) [100]. Type III has a semiconductor with both the valence and conduction band more negative than the ones of the second semiconductor ($\chi_1 + E_{Gap,1} < \chi_2$) [100]. For type I and type II the initial Fermi level of the two semiconductors, located at the energies $\Phi_{s,1}$ and $\Phi_{s,2}$, respectively, can be at different energies with respect to each other, either $\Phi_1 > \Phi_2$ or $\Phi_1 < \Phi_2$ generating two different subtypes, type 1 and type 2, respectively [100].

In type I-1 semiconductors, free electrons flow from the first semiconductor to the second one during the formation of the junction. This flow results in a space charge region around the interface with the first semiconductor side positively charged and the second semiconductor side negatively. The direction of the resulting field is indicated in each of the figures and is in this case from the first to the second semiconductor [100, 104]. By photoexcitation, holes can move from the first semiconductor to the second semiconductor, but electrons cannot travel in the same direction. However, electrons from the second semiconductor will move towards the first semiconductor, but rather than cross the junction they accumulate due to a lower conduction band in the first semiconductor [100, 105]. For type I-2 semiconductors, holes accumulate at the interface on the second semiconductor side. Electrons can flow from the first to the second semiconductor. Hence, in both cases, charge carriers accumulate at the interface on the side of the semiconductor with the smaller bandgap. This promotes recombination [100, 104, 105].

In type II-1 heterojunction the Fermi level of the first semiconductor is higher than that of the second semiconductor. This forces electrons generated in the first semiconductor as well as holes generated in the second one away from the interface [100, 106]. However, holes generated in the first semiconductor can recombine with electrons originating from the second one. This scheme of band alignment is often referred to as Z-scheme [102, 107-112]. A type II-2 heterojunction allows electrons generated in the first semiconductor to cross the junction and flow into the conduction band of the second one. Simultaneously, holes from the valence band of the second one can cross the junction and move the valence band of the first one [100].
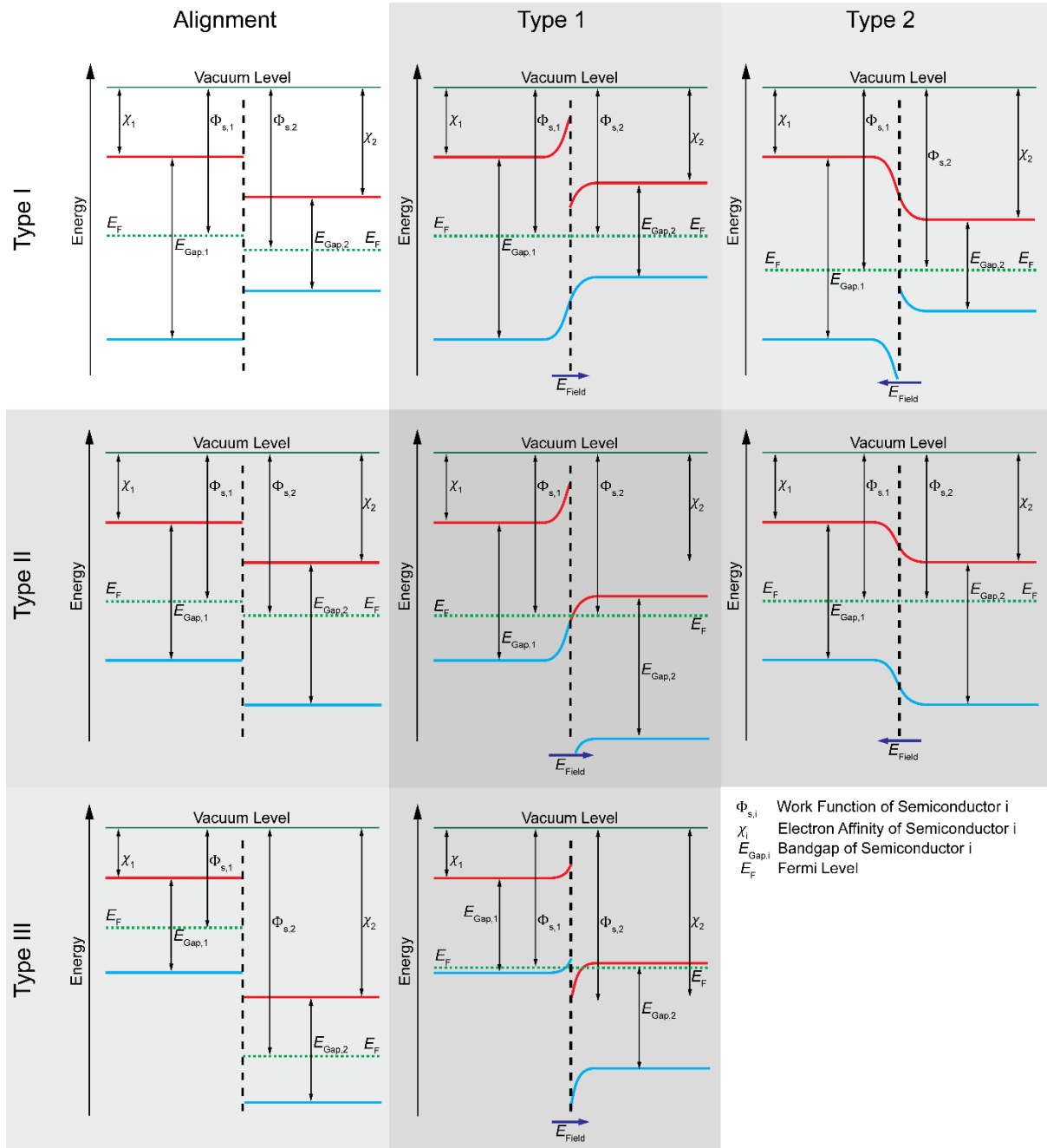
Figure 12: The alignment shows the band structure before equilibrating the Fermi energy. As is shown, there are two different subtypes for type I and type II band alignments. For type 1 subtypes, (type I-1 and type II-1) the Fermi energy of the first semiconductor is higher than the Fermi energy of the second semiconductor. Type 2 subtypes (type I-2 and type II-2) have a higher Fermi energy of the second semiconductor than of the first one, before equilibrating the Fermi level. Type III heterojunctions have only one subtype.

A type III-1 heterojunction is unable to pass electrons or holes across the junction despite holes in the first semiconductor and electrons in the second semiconductor moving towards the junction [100, 103, 113]. The band alignments of heterojunctions make them excellent junctions to separate photo-generated charge carriers [100, 114, 115]. The Cu_2O – ZnO interface forms a type II-2 band alignment [116], where Cu_2O takes the position of the

first semiconductor, with its bandgap $E_{\text{Gap},1}$ =1.7 − 2 eV [18, 28], and ZnO takes the place of the second semiconductor with a bandgap $E_{\text{Gap},2}$ = 3.37 − 3.44 eV [50-55].

2.6. Transmission Electron Microscopy

TEM is a method that provides structural and chemical information on atomic scale. The resolution limit depends highly on the instrument, mode, operator, aberrations, and corrections thereof. Complementary information can be obtained by working in both image and diffraction-mode and by combining spectroscopies (e.g. EDS, EELS). After a brief introduction to the instrument at hand, the techniques used are described in more detail below.

The apparent study was conducted in a JEOL 2100F microscope, operated at 200 kV. The main parts of a TEM are an electron gun, several lenses, a probe holder, and detectors encased in a vacuum tube. As is visible in Figure 13, the dominant part of the microscope is a long, vertical tube. Several screens and connected computers ease the usage of the instrument and allow the precise control and monitor of several vital parameters.

Figure 13: A representation of a JEOL 2100F depicting the TEM used during the experiments. The centerpiece is a large, vertical tube, containing the gun, lenses, detectors, and the sample.

2.6.1. The Electron Source

A gun is characterized by the beam brightness β_0, coherence, and stability. The brightness can be related to the beam diameter d_0, divergence angle α_0, and beam current i_e, by [76]

$$\beta_0 = \frac{4i_e}{(\pi d_0 \alpha_0)^2}.$$ (56)

The brightness depends therefore on the current density per unit solid angle of the source. In the case of a thermionic source, it increases linearly with acceleration voltage. A brighter source

has higher angular accuracy. It is crucial to have an optimal brightness to obtain a fine probe [76].

Moreover, the source should be coherent. It should be temporal coherent, meaning that the waves are in step with one another (low energy spread), and spatially coherent, meaning the electrons should originate from the same spot (small source size) [76].

A Schottky field emission gun (FEG) is used as a source in the JEOL 2100F. Field emission guns utilize a positive electrode placed near the tip, and a potential is applied between the tip and the anode (extraction voltage). This causes the electrons to overcome the work function of the filament. A second anode accelerates the electrons to the desired voltage (> 100 kV). The sharp tip (diameter $d \sim 100$ nm) is usually made of tungsten and can act as an excellent point source, which can make demagnification action by the first condenser lens obsolete [76, 77]. The absence of thermal energy spread can make the beam highly monochromatic, resulting in a reduced spread of electrons. FEGs are usually a hundred times brighter, have a lower total current, but a higher current density, and require a higher vacuum than thermionic emission guns [76, 77].

2.6.2. The Lenses

Lenses have the role of focusing, projecting, and magnifying the information obtained in their objective plane. The thin lens equation is [117],

$$\frac{1}{f} = \frac{1}{d_1} + \frac{1}{d_2} \tag{57}$$

where f is the distance between the lens and back focal plane, d_2 the distance between the lens and image plane, and d_1 the distance between the lens and objective plane. If the distance d_1 is smaller than f, no real image can be formed. Defining the magnification as $M = \frac{d_2}{d_1}$ leads to $d_2 = f\left(1 + \frac{1}{M}\right)$ meaning that the higher magnification, the weaker the lens [76].

A focused lens means that, in theory, the beam converges precisely in the image plane. An over-focused lens has a convergent beam above the image plane and an under-focused lens below. TEM images that are in focus have minimum contrast. However, a weak under-focused lens yields a more parallel beam [76].

Electromagnetic lenses work by having a current running through their magnetic yoke, which generates a magnetic field along the gap. The magnetic lenses act as convex lenses, and the beam is deflected. They take all rays from a single point in an objective plane and recreate

a point in the image plane. Parallel rays are focused in a single point in the focal plane of the lens. The focal length can be varied by changing the field between the pieces [76]. Furthermore, the field is weaker on the optical axis and most influential to the sides. The fields are inhomogeneous along the lenses length but have axial symmetry. Moreover, those lenses have limited collection angles and imperfections such as spherical and chromatic aberrations, diffraction spreading and astigmatism [76].

Spherical aberrations have a blurring effect by different convergent positions between electrons passing near the lens center and those passing off-axis. The aberration coefficient is positive, meaning rays traveling furthest from the optical axis are focused strongest. The diameter for the disk of least confusion (d_s) measures the extent of the blurring effect [76]

$$d_s = \frac{1}{2} M C_S \alpha^3 \tag{58}$$

with M the magnification, C_S the aberration coefficient, and α the aperture angle.

Chromatic aberrations cause a blurring effect due to variation in energy of electrons passing through the lens. The extent is given by the diameter of the disk of least confusion for chromatic aberrations (d_c). The aberration coefficient (C_c) is approximately 1 mm and becomes smaller with the focal distance becoming shorter. The disk of least confusion for chromatic aberrations is

$$d_C = \frac{\Delta E}{E} C_C \alpha \tag{59}$$

with ΔE the aperture angle, E the acceleration voltage, and α the aperture angle. The cause of chromatic aberration are non-chromatic electron sources and inelastic scattering events from thick specimens [76].

Additionally, diffraction spreading causes limitations, meaning a single point source will not be imaged as a point, even without aberrations, but as a disk. The Rayleigh criterion gives a diameter of

$$d_d = \frac{0.61\lambda}{\alpha} \tag{60}$$

with α the aperture angle, and λ the electron wavelength [76]. This also means, that if the intensities between two point sources reach 0.61 of the maximum intensity of the source they cannot be distinguished.

The beam passes from the source through the condenser lenses C1, C2, and C3, determining the brightness and spot size of the beam on the sample [76]. Furthermore, different apertures can be placed in the path of the beam. The condenser aperture limits the beam intensity, divergence and convergence angle, and eliminates the off-axis rays that suffer most

from the lens' imperfections [76]. The objective aperture defines the collection angle, controls the contrast in the image, and allows specific reflections to contribute to the image. The third aperture is the selected area aperture. It selects areas that contribute to the image or diffraction pattern formed (> 1 μm) [76].
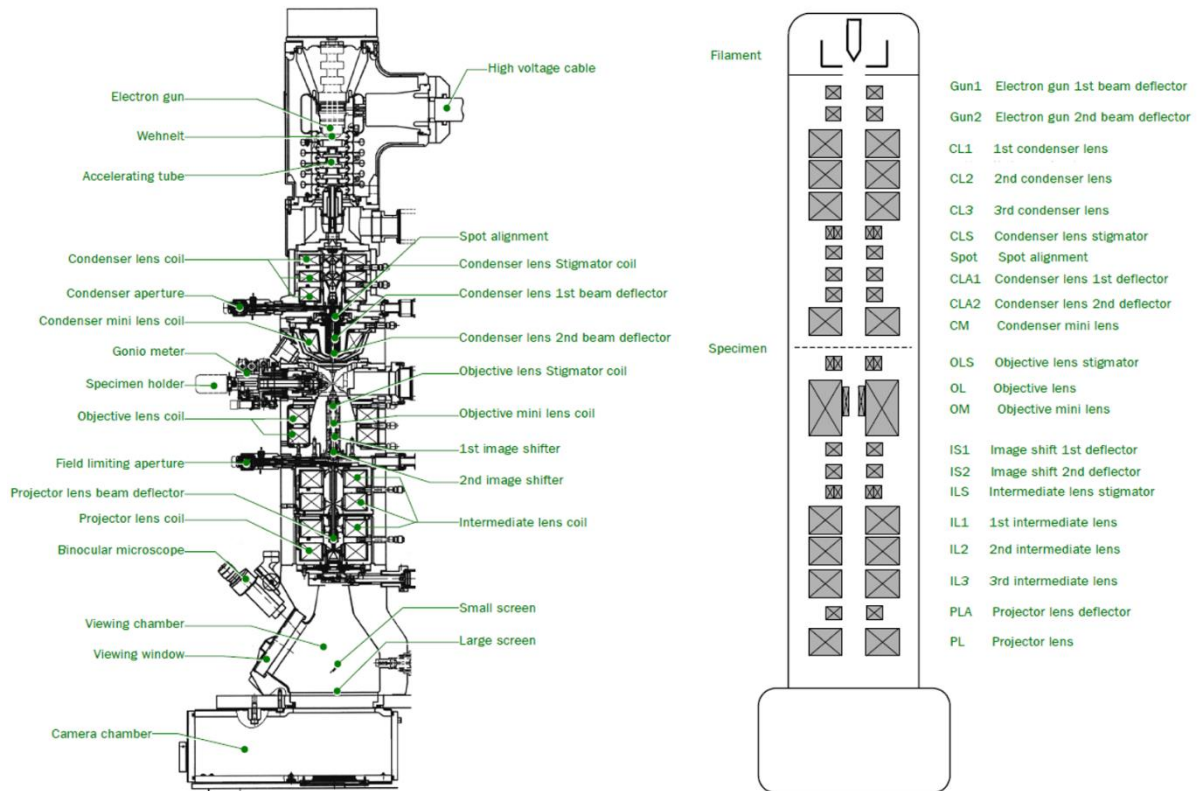
Figure 14: The layout of the TEM taken from the manual by JEOL Ltd. [118]. The gun is on top, followed by the condenser system, objective lenses, and imaging system.

The objective lens is the core of the TEM; its quality determines the quality of the results. Thus, objective lens imperfections should be reduced, corrected, or compensated. Rays leaving the specimen at the same angle subsequently converge in the back focal plane. This back focal plane contains the diffraction pattern, and the objective aperture is inserted in the back focal plane of the objective lens [76, 77].

The electrons travel along a helical path, meaning that in addition to the 180° rotation induced by each lens, an image rotation effect occurs. This results in rotation of the TEM images and diffraction patterns when changing the focus or magnification. The eucentric plane is a standard objective plane for the primary imaging lens of the microscope. The height of the specimen should be the eucentric plane. The sample can be tilted in the eucentric plane without getting out of focus [76].

Two principal operation modes were used in this study: a parallel beam, used for TEM imaging, and acquisitions of selected area electron diffraction (SAED) patterns, and the

convergent beam used for STEM imaging and spectroscopies [76]. They require high electron beam intensity in order to have images at high magnification, a small energy spread, and high brightness of the electron beam [76].

2.6.3. Modes of Operation

In this thesis TEM analysis was used in order to obtain structural and chemical information of the heterojunctions. Structural information was obtained by working in TEM-mode through TEM imaging and SAED patterns. In particular, SAED can be used to gain knowledge of the orientation relationship between different phases. Chemical information was obtained by applying spectroscopies (EDS, EELS) in STEM-mode.

A)   TEM-Mode

In TEM-mode bright-field imaging uses the transmitted or non-diffracted electrons to form an image. Hence, the intensity of any point on the image is defined by the sample thickness, atom type, and crystal structure of the sample displayed in that point. High-resolution TEM requires the use of a large objective aperture. It forms interference patterns from the phase relationship of the diffracted beams with the transmitted beam as a reference phase. The phase contrast is formed because the phase of the diffracted wave is preserved, and interferes constructively or destructively with the phase of the transmitted wave [76, 77]. HRTEM is useful to identify defects and studying atomic arrangements at the interfaces. The image resolution is a measure of spatial frequencies from the image amplitude spectrum (exit-surface wave function) into the image intensity spectrum (the Fourier transform of the image intensity). The resolution is affected by the phase of the diffracted beams exiting the sample, the objective lens, the aperture, imperfections, and thickness of the sample [76, 77].

SAED is a technique where the insertion of an aperture in the image plane results in the formation of a virtual aperture in the plane of the specimen. Electrons are falling inside the dimension of the virtual aperture will be allowed through into the imaging system to contribute to the diffraction pattern [76, 77].

Reciprocal Space and Diffraction

Interference describes waves interacting with each other while traveling along the same medium. The resulting wave-function is the sum of the two individual wave functions. Constructive interference is the displacement in the same direction. Destructive interference is the displacement in the opposite direction. Superposition of out of phase waves gives rise to both constructive and destructive interference [76, 77].

Diffraction is the spreading or bending of waves around obstacles and openings. Diffraction patterns are an angular distribution of scattering events. Amorphous materials do scatter, too, and show a radial distribution function, implying the average bond length [76, 77]. Diffraction is a cooperative phenomenon based on phase relationships between wavelets/wave-functions scattered coherently by the individual atoms (wave interference phenomenon). Figure 16 shows two experiments generating interference, one with slits and the other with atom columns.

The Laue condition states that $\vec{K} = m\vec{a}^* + n\vec{b}^* + p\vec{c}^* = \vec{g} + \vec{s}$, where $\vec{K}$ is the difference between the incident wave vector and diffracted vector, and $\vec{s}$ the difference between spot center and Ewald sphere. If $\vec{s} = 0$, then the special case of the Laue condition, Bragg's Law is valid with the equation $n\lambda = 2d \sin \Theta$, where n is an integer, λ the wavelength, d the spacing between planes, Θ the angle between the incident beam and the planes, as indicated in Figure 16. The Ewald sphere is a graphical representation of the Laue condition [76, 77]. A representation of it is shown in Figure 15. The Laue zones, groups of diffraction spot cut by the Ewald sphere, are grouped in zeroth, first, and higher order Laue zones. All the points in the zones fulfill the Laue condition, and they contain fewer and fewer spots [76, 77].
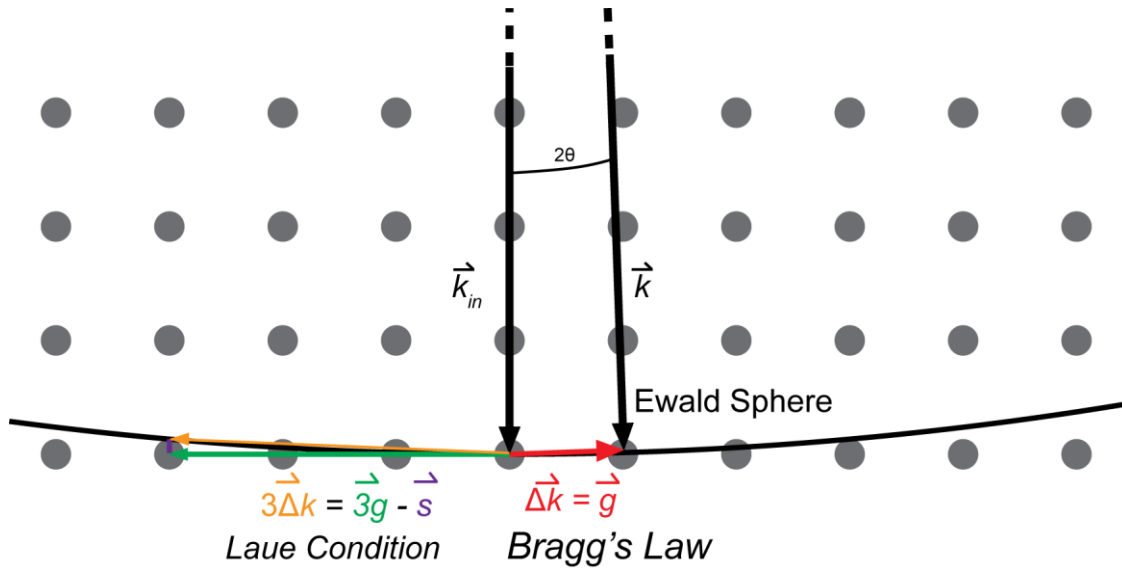
Figure 15: The Ewald sphere with its flat curvature. The flatness of it explains the extent of the zeroth Laue zone around the central peak usually shows numerous diffraction spots. Indicated in red is the condition satisfying Bragg's Law. The tri-colored scheme to the left depicts a diffraction point that will yield a weak point in the diffraction pattern.

Important information can be extracted by Diffraction patterns: a) they reveal whether a phase is crystalline or amorphous, b) the orientation of each crystalline structure can be determined, and the orientation relationship between different grains and materials can be determined, c) the cell parameters, for example, the lattice parameters, can be extracted by analyzing the diffraction pattern.
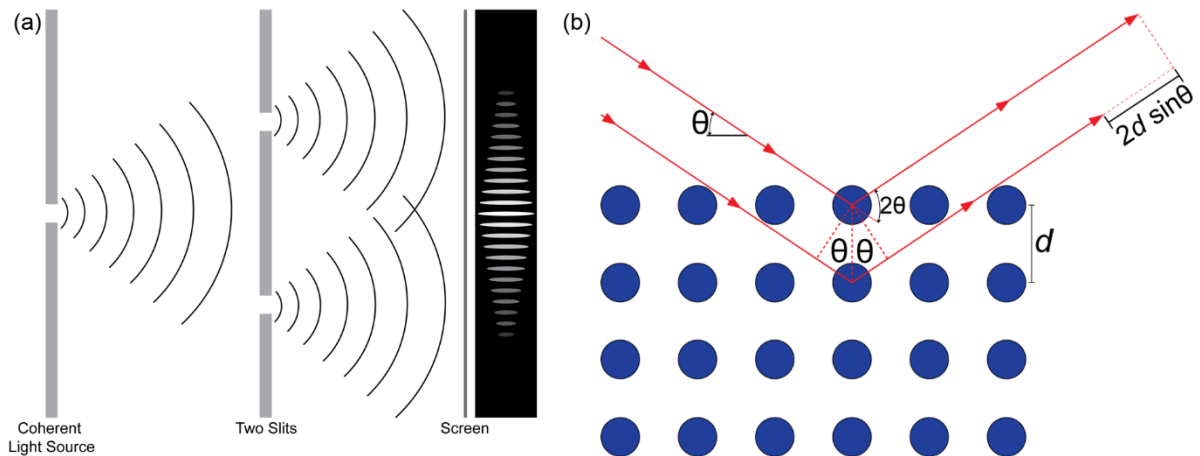
Figure 16: (a) The Young double slit experiment in a sketch. A single slit is used to make the waves coherent and in-phase, and the double slit forces the two waves to interfere [119]. (b) Bragg's law in a figure. The law states that if $n\lambda = 2d \sin \Theta$. The Laue condition is the extension of Bragg's law [76].

B)   STEM-Mode

STEM utilizes a converged beam forming a nano-sized probe, that is systematically scanned across the sample. In STEM imaging mode, elastically scattered electrons are utilized to form the image. For higher angles, ($\theta > 50$ mrad), the intensity recorded is close to proportional to the atomic number of the observed atoms squared (Z^2). Consequently, a chemical contrast is visible (Z-contrast). This type of image is referred to as high-angular annual dark field STEM (HAADF-STEM). The image is acquired differently than in TEM mode. The detector is doughnut-shaped around the central axis. In every pixel the signal generated on the entire detector creates the intensity displayed on the image [76, 77, 120]. The heavier an atom, the brighter its signal generated on the HAADF detector. Hence, HAADF-STEM images provide useful chemical information of the sample.
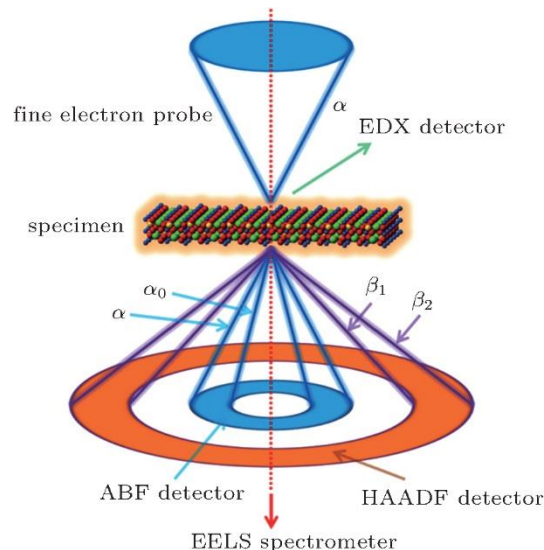
Figure 17: A schematic representation of a HAADF detector setup, used for Z-contrast imaging in STEM mode (found in [120]).

Energy Dispersive X-Ray Spectroscopy

EDS spectra are acquired using an x-ray detector within the TEM column [76, 77]. An x-ray, originating from an inelastic scattering event, generates a pulse of current in an x-ray detector [76, 77]. Such a detector should be producing a pulse for every x-ray, with a net charge proportional to the energy of the x-ray photon, while keeping a constant amplitude over time and have a large solid angle [76, 77]. These x-rays are characteristic and allow the chemical analysis of the targeted area of a specimen. In particular, the measured x-rays depend on the path and energy of the high-energy electron passing through the sample, the ionization cross-

sections of the elements, the fluorescence yields and the probabilities that the emitted x-ray reaches the detector [76, 77].

The x-rays are generated by ionizing an atom with the electron beam, and subsequent relaxation of said atom [76, 77, 121]. Hence, assuming an electron with the incident energy, and an x-ray traveling unhindered to the detector, the energy measured is unique to the type of atom [76, 77, 121]. Consequently, EDS can be used to determine the composition of a sample.

2.7. Density Functional Theory

Density functional theory (DFT) emerged as an essential technique in materials science and became increasingly wider used in scientific publications [122]. The theory is based on quantum mechanics, like many forms of computational chemistry and computational physics. DFT is enabling the study of atomistic properties of materials that are used in solar cells, light emitting materials, thermoelectric materials, catalysis, or batteries [122]. Its usefulness originates in its applicability to almost all materials. Furthermore, the rather large system size with up to one thousand atoms allows it to have a balance between accuracy and usability. Finally, it does not need empirical parameters. However, the variation of codes and differential functional has exploded over the past years, creating difficulties in obtaining comparable results [122]. The codes can be grouped into two main categories, molecular codes, used for molecules, and periodic codes. The latter can be divided into local orbital basis codes, all electron (augmented methods) codes, and plane wave and related (for example real space, and wavelet) codes [122], e.g., the Vienna Ab-initio Simulation Package (VASP). For the work at hand, VASP has been the code of choice. In order to support the choices made, and conclusions drawn below, a short introduction to the essential aspects of DFT is given.

2.7.1. Theoretical Background

A single atom can be described by giving the position of the nucleus and all its electrons. Similarly, an assembly of atoms can be described by giving the position of the nuclei and their electrons. The manifold heavier nucleus can be treated as very slow reacting compared to the electrons [122]. Consequently, electrons and nuclei can be treated separately, in two mathematical problems. This separation is the Born-Oppenheimer approximation. For any given nuclei-distribution, the lowest energy configuration (state) of the electrons can be found. The state with the lowest energy is called the ground state. Consequently, the ground state

energy E_0 can be expressed as a function of the nuclei, $E(\vec{R}_1, \dots, \vec{R}_N)$, with $\vec{R}_i$ the position of the i-th nuclei. This function is known as the adiabatic potential energy surface [122].

The time-independent, non-relativistic Schrödinger equation for a system with multiple electron interacting with multiple nuclei is

$$\left[-\frac{\hbar^2}{2m_e} \sum_{i=1}^N \nabla_i^2 + \sum_{i=1}^N V(\vec{r}_i) + \sum_{i=1}^N \sum_{j<i} U(\vec{r}_i, \dots, \vec{r}_j) \right] \psi(\vec{r}_1, \dots, \vec{r}_N) = E\psi(\vec{r}_1, \dots, \vec{r}_N) \quad (61)$$

with m_e being the electron mass, N the number of electrons, $\psi(\vec{r}_1, \dots, \vec{r}_N)$ the electronic ground state wave function, and E the ground state energy electrons [122]. Additionally, it is important to define the density $n(\vec{r})$ as

$$n(\vec{r}) = 2 \sum_i \psi_i^*(\vec{r}) \, \psi_i(\vec{r}) \quad (62)$$

where $\psi_i^*(\vec{r})$ is the complex conjugate of the wave function $\psi_i(\vec{r})$ [122]. With a suitable Schrödinger equation, and the definition of the electron-density, one needs to use two fundamental pillars of DFT: the Hohenberg-Kohn theorems, and the Kohn-Sham equations.

The first Hohenberg-Kohn theorem states:

The ground-state energy from the Schrödinger equation is a unique functional of the electron density. [122]

This means that there exists a one-to-one mapping between the ground-state wave function and the ground-state electron density. This mapping has been proven by Hohenberg-Kohn [122, 123]. Furthermore, it is equivalent to say that the ground state electron density uniquely determines all properties of the ground state. This means that a problem with N electrons has only three dimensions, instead of $3N$ (three for each electron) [122].

It is quite unfortunate that the first Hohenberg-Kohn theorem does not provide the function of the electron-density that can be used to solve the Schrödinger equation. The second Hohenberg-Kohn theorem states:

The electron density that minimizes the energy of the overall functional is the true electron-density corresponding to the full solution of the Schrödinger equation. [122]

If the exact form of the functional would be known, the electron-density could be varied until the energy is minimal. This is used with an approximate form of the functional.

The functional described by Hohenberg-Kohn theorem can be written in terms of single electron wave-functions (which are the base for the electron-density),

$$E_0[\psi_i] = E_{\text{known}}[\psi_i] + E_{\text{XC}}[\psi_i]. \quad (63)$$

The functional is split into two parts, the known part $E_{\text{known}}[\psi_i]$, and the exchange-correlation part $E_{\text{XC}}[\psi_i]$. The known part includes four contributions [122],

2. Theory and Literature Review

$$E_{known}[\psi_i] = -\frac{\hbar^2}{2m}\sum_i \int \psi_i^* \nabla^2 \psi_i \mathrm{d}^3 r + \int V(\vec{r})n(\vec{r})\mathrm{d}^3 r +$$

$$\frac{e^2}{2} \int \int \frac{n(\vec{r})n'(\vec{r}')}{|\vec{r}-\vec{r}'|} \mathrm{d}^3 r \, \mathrm{d}^3 r' + E_{ion}. \quad (64)$$

These terms are (in order of appearance): the electron kinetic energies, the Coulomb interactions between electrons and nuclei, the Coulomb interactions between pairs of electrons, and the Coulomb interaction between pairs of nuclei. The exchange correlations part includes all terms disregarded in the known terms.

Kohn and Sham showed that the task to find the electron density could be achieved by solving a set of equations, each involving only one single electron. These are the Kohn-Sham equations, and they are of the form

$$\left[-\frac{\hbar^2}{2m}\nabla^2 + V(\vec{r}) + V_H(\vec{r}) + V_{XC}\right]\psi_i(\vec{r}) = \epsilon_i\psi_i(\vec{r}). \quad (65)$$

The first potential, $V(\vec{r})$, is the known part of the total energy functional ($E_{known}[\psi_i]$) [122]. It defines the interactions between the electron and the set of nuclei. The second potential term is the Hartree potential,

$$V_H = e^2 \int \frac{n(\vec{r})}{|\vec{r}-\vec{r}'|} d^3 r'. \quad (66)$$

It describes the interaction between the electron and the total electron density defined by all electrons. This includes self-interaction of the electron.

A Coulomb interaction of an electron with itself is unphysical. Hence, it has to be corrected. This correction term is part of the exchange-correlation term [122]. Formally, the exchange-correlation functional can be defined as

$$V_{XC}(\vec{r}) = \frac{\delta E_{XC}(\vec{r})}{\delta n(\vec{r})}. \quad (67)$$

To solve the Kohn-Sham equation, the Hartree potential needs to be defined. To define the Hartree potential, the electron density has to be known [122]. The electron density is known if the single electron functions are known. Finally, to know the single electron wave function, the Kohn-Sham equations have to be solved. The cycle can be broken by following the steps below [122].

1. An initial, trial electron density $n(\vec{r})$ has to be defined.
2. The Kohn-Sham equation has to be solved using the trial electron density to define the single particle wave equations, $\psi(\vec{r})$.
3. A new electron density has to be calculated, using the single particle wave function, $n_{KS}(\vec{r}) = 2\sum_i \psi_i^*(\vec{r})\,\psi_i(\vec{r})$.

4. Comparing the initial electron density with the new electron density yields whether a ground state has been found. In that case, they are equal to each other. If not, the initial electron density has to be updated.

2.7.2. Implementation

In practice, all the calculations solved on a computer have to be finite, meaning, for example, infinite summations cannot be calculated. However, the mathematics behind DFT often include integrals over an infinite number of points and infinite sums. In order to have reliable, reproducible results, all the calculations have to be converged [122]. Convergence means that the solution found by DFT calculations is an approximate representation of the real solution, which is more and more accurate the more computational resources are utilized during the calculation. However, this convergence does not automatically make the DFT calculations physically accurate because the two mathematical problems, one defined by the Schrödinger equation and one by DFT, are not the same. As shown above, DFT includes an unknown potential, whereas the Schrödinger equation does not [122].

The calculations of a single point in k-space would require a summation over an infinite number of reciprocal lattice vectors, $\vec{G}$ (defined like $\vec{r}^*$, and additionally $\vec{G} \cdot \vec{r} = 1$, see section 2.1.2). Bloch's theorem states that the solution of the Schrödinger equation can be expressed as

$$\phi_{\overline{k}}(\vec{r}) = \exp(i\vec{k} \cdot \vec{r}) u_{\overline{k}}(\vec{r}) \tag{68}$$

where the functions $\exp(i\vec{k} \cdot \vec{r})$ are called plane waves, $\vec{r}$ a vector in real space, $\vec{k}$ is a vector in reciprocal space, and $u_{\overline{k}}(\vec{r})$ a periodic potential with the periodicity of the supercell, with the form

$$u_{\overline{k}}(\vec{r}) = \sum_{\vec{G}} c_{\vec{G}} \exp[i\vec{G} \cdot \vec{r}] \tag{69}$$

with $c_{\vec{G}}$ the respective weighting of the terms [122]. Using eq. (69) in eq. (68) yields

$$\phi_{\overline{k}}(\vec{r}) = \sum_{\vec{G}} c_{\vec{k}+\vec{G}} \exp[i(\vec{k} + \vec{G}) \cdot \vec{r}]. \tag{70}$$

As argued above, infinite sums, as in eq. (69) and eq. (70), are hardly useful in computational physics or chemistry. However, simple solutions for the obtained Schrödinger equation exist, all with the kinetic energy [122]

$$E = \frac{\hbar^2}{2m} |\vec{k} + \vec{G}|^2. \tag{71}$$

Moreover, solutions with lower energy are typically more significant. Hence, a cutoff energy can be introduced, determining the energy up to which the solutions are included in the calculation [122]. This cutoff energy is defined as [122]

$$E_{\text{cutoff}} = \frac{\hbar^2}{2m} G_{\text{cutoff}}^2 \tag{72}$$

and the solutions for the Schrödinger equation change to

$$\phi_{\vec{k}}(\vec{r}) = \sum_{|\vec{k}+\vec{G}|<G_{\text{cutoff}}} c_{\vec{k}+\vec{G}} \exp\left[i(\vec{k}+\vec{G}) \cdot \vec{r}\right]. \tag{73}$$

However, to ensure the validity of this solution, the cutoff energy has to be determined, by evaluating the convergence concerning the cutoff energy beforehand [122].

DFT utilizes the Brillouin zone and *k*-space in order to reduce the number of calculations. The integrals in reciprocal space are evaluated at the possible values of $\vec{k}$ only, rather than over the entire real space [122]. Moreover, methods like the Gaussian quadrature can be used to approximate the integrals. There are three main points to be considered for integrals:

1. Computing the function at several discrete points and summing up the resulting values with a suitable weighting allows the approximation of an integral

2. The sum converges to the exact value of the integral for a more significant number of points and well behaved numerical methods.

3. The placement and weighting of the functional evaluations determine the rate of convergence.

The number of *k*-points in each direction has to be determined before calculating any systems [122]. Hence, a convergence criterion used during the experimental part is introduced in section 3.2.1 concerning the *k*-point density.

2.8. Gibbs Free Energy for the Formation of Cu₂O and ZnO

The Cu₂O – ZnO junction has some material specific background that needs to be established before investigating the junction further. The intrinsic defect chemistry of both materials has already been stated above, but the formation dependency of the oxide on the partial pressure and temperature will be established.

The Gibbs energy per mole for a system can be used to determine, e.g., whether a phase will be favored over another under certain conditions. The influence of both temperature and oxygen partial pressure can be studied before carrying out experiments. At hand are the two

most stable copper oxide phases and copper itself. As they are frequently encountered when dealing with either one of them, the conditions of formations have to be discussed. Equation (11) uses the temperature explicitly, and the oxygen partial pressure as part of the equilibrium constant K. These values are stated in Table 3 for the copper oxides, and Table 4 for ZnO, and are used in Figure 18. The log K is directly related to the pressure and in this case the oxygen partial pressure. Plotting the values of the oxygen partial pressure versus the temperature yields a plot that visually allows the determination of the most stable phase under any set condition for the range of the data.

Table 3: The temperature and corresponding log K for CuO and Cu_2O are shown, as taken from the book: "Thermochemical Data of Pure Substances" by I. Barin and G. Platzki [81]. These values are the basis of the plot in Figure 18.

Cupric Oxide ($2Cu + O_2 = 2CuO$):		Cuprous Oxide ($4Cu + O_2 = 2Cu_2O$):	
T [K]	log K	T [K]	log K
298.15	22.476	298.15	25.908
300.00	22.308	300.00	25.724
400.00	15.523	400.00	18.293
500.00	11.469	500.00	13.840
600.00	8.780	600.00	10.877
700.00	6.870	700.00	8.766
800.00	5.445	800.00	7.187
900.00	4.343	900.00	5.964
1000.00	3.468	1000.00	4.989
1100.00	2.755	1100.00	4.194
1200.00	2.165	1200.00	3.534
1300.00	1.669	1300.00	2.979
1397.00	1.243	1400.00	2.474
NDPT: ($Cu_2O + O_2$) = 1397.00 K		1500.00	2.000
		1516.7	1.927
NDPT = Normal Decomposition Point		1600.00	1.704
		1700.00	1.468
		1800.00	1.260
		1900.00	1.077
		2000.00	0.914

Figure 18 shows the dominant phases under given conditions. Under ambient conditions, CuO and ZnO are the most stable phases. Moreover, it displays that a combination of very low oxygen partial pressure and high temperature (log P_{O_2} < -10, T > 800°C) lead to

pure Cu and depending on the specific conditions Zn or ZnO. A successful formation of Cu_2O depends on a low oxygen partial pressure, which slowly increases with increasing temperature. Fortunately, ZnO is readily formed under these conditions. Thus, the formation of a Cu_2O – ZnO p-n-junction depends solely on the successful formation of the Cu_2O phase. Furthermore, there are conditions under which the copper phase would be liquid or even gaseous and the ZnO still solid.

Table 4: The temperature and corresponding log K for ZnO are shown, as taken from the book: "Thermochemical Data of Pure Substances" by I. Barin and G. Platzki [81].

| Zinc Oxide (2 Zn + O₂ = 2ZnO):		Zinc Oxide (cont.):	
T [K]	log K	T [K]	log K
298.15	56.146	1500.00	5.703
300.00	55.768	1600.00	4.692
400.00	40.517	1700.00	3.803
500.00	31.374	1800.00	3.017
600.00	25.286	1900.00	2.316
700.00	20.936	2000.00	1.687
800.00	17.612	2100.00	1.121
900.00	15.028	2200.00	0.609
1000.00	12.962	2248.00	0.380
1100.00	11.273	2300.00	0.172
1200.00	9.777	2400.00	-0.201
1300.00	8.205	2500.00	-0.542
1400.00	6.862	Melting Point = 2048 K	
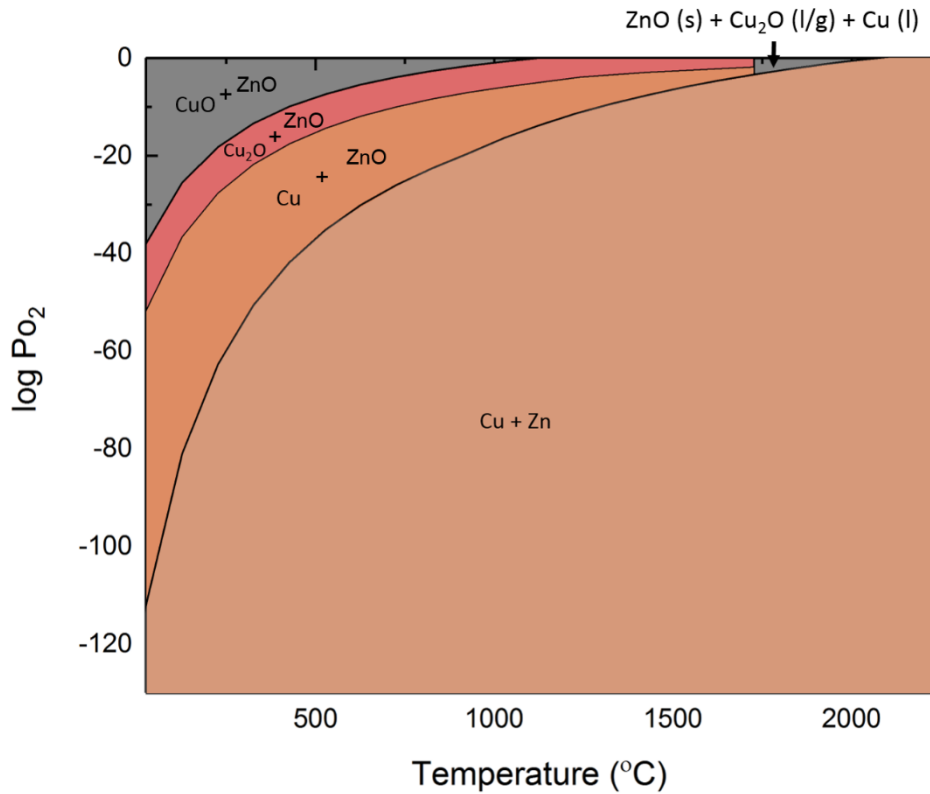
Figure 18: The log p_{O2} plotted versus the temperature, based on the values in Table 3 and Table 4. It shows how narrow the range for a successful formation of Cu_2O is. The CuO and Cu phases dominate the plot, which is an explanation of why they are frequently encountered while working with Cu_2O. Moreover, a wide area for a successful formation of ZnO is visible. The Zn phase dominates the extremely low Po_2 and high-temperature regime.

2.9. Copper Oxide-Based p-n-Junctions

Cu_2O was considered multiple times as a semiconductor for a variety of applications throughout the 20th century [18, 97, 124-126]. Before the discovery of the point contact transistor (1947), and the metal oxide semiconductor field effect transistor (1960), Cu_2O was thought of as a possible material for a Schottky junction within rectifiers in radio receivers. However, the simplicity of single crystal Si and Germanium, available both as p-type and as n-type in combination with these inventions considerably lowered these efforts [18, 97, 127]. Not at last due to the first oil crisis, materials for solar cell applications were in focus in the last quarter of the 20th century [128-130]. Cu_2O was considered one of them, primarily because of its high refractive index in the visible spectrum. However, leading up to the 21st century the power conversion efficiency, η, of Cu_2O -based solar panels barely reached 1% [18].

2. Theory and Literature Review

Table 5: A selection of reported conversion efficiencies (η) and the air mass (AM) are listed by year. The G indicates global, and the D indicates direct.

Heterojunction	Year	Conversion Efficiency η (%) at (AM)	Ref.
Cu_2O/ZnO	1980	0.14	[126]
Cu_2O/ZnO:Al	2004	1.2 (2)	[131]
Cu_2O/i-ZnO/ZnO	2006	0.4 (1.5)	[24]
Cu_2O/ZnO:Ga	2006	1.52 (2)	[23]
Cu_2O/AZO		1.42 (2)	
Cu_2O/ZnO	2006	2 (1.5G)	[132]
Cu_2O/ZnO	2007	1.28 (1.5)	[133]
Cu_2O/ZnO/ZnO:Al	2008	3.83 (1.5)	[134]
Cu_2O/CH_3CN (p-Cu_2O /liquid junction)	2011	1.5 (1.5)	[135]
Cu_2O/ZnO	2011	3.85 (1.5G)	[14]
GaN/Cu_4O_3	2012	0.009 (1.5G)	[28]
n-Si/CuO	2012	0.41 (1.5D)	[136]
Cu_2O/ZnO (bilayer)	2012	0.6 (1.5G)	[137]
Cu_2O/ZnO (nanowire)		0.4 (1.5G)	
Cu/Cu_2O (semiconductor-liquid junction solar cells, I^-/I_3^- electrolyte)	2012	3.13 (1.5G)	[138]
Cu_2O/a-ZTO/ZnO:Al	2013	2.64 (1.5G)	[139]
Cu_2O/Ga_2O_3/ZnO:Al	2013	5.38 (1.5G)	[140]
ZnO/CuO/copper oxide nanopowder	2014	2.88 (1.5)	[12]
CuO/Cu_2O	2015	0.64 (1.5)	[141]
n-Si/CuO:N	2015	1.0 (1.5)	[38]
p-μc-Si:H/i-a-Si:H/n-CuO_x	2015	3.04 (1.5)	[142]
Cu_2O:Na/Al_xGa_{1-x}/ZnO:Al (x = 0.025)	2015	6.1 (1.5G)	[98]

Cu_2O can be both the absorber, and the substrate for depositing an n-type wide band gap semiconductor. The very first heterojunction solar cell based on a Cu_2O-ZnO junction with a third layer, a transparent conducting oxide (TCO), on top of the junction was introduced in 1980 [126]. Its η was reported as 0.14%. A list of the reported solar cells involving copper oxides and their conversion efficiency is given in Table 5. A considerable amount of research effort was dedicated to studying the formation techniques of Cu_2O in the years leading to the new millennium [143-147], and the insights gained was used in the more recent years to improve the junction considerably.

A review of efforts in until the early 1980s has been given by Rakhshani, already indicating CuO and Cu_2O formation at low temperatures [127]. Moreover, the necessity to identify an n-type semiconductor for the junction [148], lead to an investigation into several conducting oxides, In_2O_3, In_2O_3:Sn (ITO), ZnO, ZnO:Al (AZO) and ZnO-In_2O_3 in 2004 [131].

While In_2O_3 and ITO ($\eta = 0.03\%$, AM 2) yielded poor conversion efficiencies, ZnO and AZO yielded conversion efficiencies of 0.9% (AM 2) and 1.2% (AM 2), respectively. These results suggested that both ZnO and AZO are suitable as TCO [131].

A Cu_2O – ZnO heterojunction solar cell on glass was reported in 2006 [24]. Simultaneously, it was concluded that the sequence of deposition by radio frequency (rf) magnetron sputtering has a significant influence on the properties of the junction. If ZnO was deposited first, better rectifying behavior and a η of 0.4% was observed, in comparison to no photovoltaic effects in samples with Cu_2O deposited first [24]. Identifying suitable n-type semiconductors which can be deposited onto a Cu_2O substrate has already been reported in [131]. However, establishing that the order of deposition influences the results allowed determining that fewer defects formed in one order of deposition than in the other [24].

The η of all the manufactured junctions remained below 2%, far below the theoretical limit of 20% at AM 1 [129]. Utilizing Cu_2O substrates, different deposition techniques, such as DC magnetron sputtering, rf magnetron sputtering, PLD, and vacuum arc plasma evaporation (VAPE), were investigated [23]. The AZO film properties were highly dependent on the substrate temperature and the sample orientation and positions in the sputtering systems of the DC magnetron and rf magnetron sputtering setup. These materials properties influence the junction between Cu_2O and AZO directly [23]. Moreover, it indicates that DC magnetron and rf magnetron sputtering are not suitable techniques to form a junction between Cu_2O and ZnO. Instead, PLD and VAPE, both avoiding ion bombardment of the Cu_2O surface, became the techniques of choice, and are frequently used [23]. The reported η for PLD fabricated junctions is 1.42%, and for VAPE manufactured junctions it is 1.52% in 2006 [23].

Later in the same year, the first publication describing a Cu_2O-ZnO p-n-junction with a conversion efficiency over 2% was printed [132]. The architecture of the device consisted of four layers plus a gold contact. The contact on the back of a Cu_2O substrate, followed by ZnO, ITO and magnesium fluoride (MgF_2) ($Au/Cu_2O/ZnO/ITO/MgF_2$) showed a η of 2.01% under AM 1.5G illumination [132]. As a reference measurement, an $Au/Cu_2O/ITO/MgF_2$ junction was used, with a measured lower η. However, it is believed that the performances of both junctions were influenced negatively by defects at the heterointerface [132].

It was not until 2011 that a Cu_2O based heterojunction showed a η of more than 3% [14]. A Cu sheet was oxidized in a three-step process before ZnO and AZO were deposited on top. In this setup, the AZO acts as a window layer, and either gold or Cu_2S (copper sulfide) were used as back contact [14]. The junction parameters were measured as a function of the

2. Theory and Literature Review

ZnO film thickness and the maximum $\eta = 3.83$ (AM 1.5G) for $30 - 50$ nm thick ZnO [14]. The reference junction, Cu_2O/AZO, had a maximum $\eta = 1.6\%$ suggesting that the ZnO buffer layer improves the contact quality to Cu_2O [14]. Further investigation of the junction, with a ZnO thickness of $0 - 150$ nm for the Cu_2O/ZnO/AZO junction revealed a $\eta = 4.08\%$ for a ZnO thickness of 50 nm in 2012 [149]. It was also determined that the built-in potential for CuO/ZnO/AZO is higher than for a Schottky junction [149]. The thicker active layer, due to the low carrier concentration in ZnO, lead to a broader photo-voltage spectrum below 460 nm due to the formation of said heterojunction [149].

To improve the conversion efficiency even more, gallium oxide Ga_2O_3 was utilized as a buffer layer instead of ZnO [140]. The G_2O_3 was undoped and n-type, and the junction according to the architecture Au/Cu_2O/Ga_2O_3/AZO was built [140]. The change of oxide was motivated due to the smaller conduction band offset (ΔE_C) between Cu_2O and Ga_2O_3 due to the electron affinity χ of Ga_2O_3 is between Cu_2O and ZnO [140, 150]. The smaller difference theoretically leads to a higher conversion efficiency. Like in the ZnO based junctions, the Ga_2O_3 layer thickness influenced the properties of the junctions. After optimizing the thickness, a η of 5.38% was achieved [140].

The highest achieved η of 6.1% was reported in 2015 [98]. The substrate used was a Na doped Cu_2O. The doping decreased the resistivity but did not decrease the Hall mobility. As a buffer layer, aluminum gallium oxide $((Al_{0.025}Ga_{0.975})_2O_3)$ was used. Moreover, AZO acted as a window layer, and the MgF_2 was used as an antireflection layer [98].

Different architecture types were utilized, too. Atomic layer deposition (ALD) was used to create an amorphous zinc tin oxide (a-ZTO) onto a Cu_2O. The junction Au/Cu_2O/a-ZTS/ZnO:Al at optimized conditions showed a η of 2.65% [139]. The reduction of the thickness of a-ZTS increased the η to 3.06% at $70°C$ deposition temperature [151]. Moreover, introducing Cu_2O:N between the Cu_2O and the gold contact reduced the contact resistance [152]. Finally, Cu_2O films can also be utilized as hole transport layers in perovskite solar cells [153]. The development of Cu_2O-based solar cells shows the activity in the field and the potential to improve performance. Moreover, it is of interest to obtain a copper-based junction, for example, Cu_2O – ZnO, which operates close to its theoretical limit.

CuO-based junctions have not been studied for as long as Cu_2O based junctions. However, in the past ten years, the junctions have been researched more extensively [37, 38, 136, 154-156]. These junctions are typically formed on Si wafers, by depositing thin films of CuO. Thermal oxidation has not been reported. However, reactive magnetron sputtering was

used to fabricate a p-CuO/n-Si junction [136]. The η of the optimized structure was 0.41% under AM 1.5G illumination for the Cu/p-CuO/n-Si/Al device structure in 2012. Furthermore, an rf argon sputtering of CuO onto n-Si(100) was utilized. Subsequently, the sample was annealed in nitrogen at 300℃, and a photo-voltage was observed (0.41% (AM 1.5D)). However, a Cu rich oxide was recorded at the interface, too [136]. Improving the manufacturing method by sputtering CuO at two different powers, the first one lower than the second one, improved the η to 1.21% [37]. These steps were implemented after studying the origin of the Cu-rich layer and the formation of a native SiO layer at the junction [37]. In another study, Al/Ti/p-CuO/n-Si/Ti/Al showed a η of almost 1% [38]. Moreover, the copper-rich phase at the interface showed a mixture of CuO and Cu_2O [38].

The effects of doping on these junctions were investigated in 2015 [142, 155]. The effects of the N concentration and annealing temperature on the crystal structure were studied. Specifically, a concentration of 1.5% N in the Ar flow during the deposition did not change the crystal structures, but higher concentrations forced the formation of CuO and Cu_2O phases. The samples were annealed at 300℃ [155]. Furthermore, doping the CuO with Ti up to 0.099 at% reduced the resistivity of CuO [156]. The influence of the pressure during the rf magnetron sputtering at high working pressure (30 mTorr) showed better crystal quality than one at lower working pressure (3.5 mTorr) [157].

The n-type CuO has not been reported until recently. In 2015, n-type CuO was deposited onto intrinsic i-a-Si:H by utilizing non-stoichiometric CuO_x. The η of 3.04% was observed, and could be further increased to 4.79% by utilizing a thin n-doped hydrogenated microcrystalline Si (n-µc Si:H) depletion assisting layer between the two [142]. A solar cell with Ti/p-CuO/n-Cu_2O/Au setup showed a η of 0.64% after annealing [141]. Moreover, utilizing a Cu_4O_3/GaN solar cell showed a η of 0.009% [28]. The variety of junctions availability shows the interest in stable, earth-abundant low-cost materials, and efficient solar cells [158-164]. Copper Oxides have bandgaps suitable for single junctions and tandem junction solar cells, suiting the requirements as a future solar cell. However, there is need of improving manufacturing techniques as well as industrializing them [165-169]. Multitudes of different Cu-based structures, besides Cu_2O – ZnO have been suggested and tested [170-180].

The radius of the individual grains should be as small as possible to reduce the average diffusion time, and the number of recombination, and consequently maximizing the conversion efficiency [12]. The average diffusion time, τ_d, from the bulk of a given material to its surface upon production of a charge carrier due to an incoming photon is:

$$\tau_d = \frac{r^2}{D\pi^2} \tag{74}$$

where r is the grain radius and D the diffusion coefficient [12].

It is crucial to comprehend the charge carrier transport at the interface of such a junction. Hence, understanding the band alignment of the two materials at hand is an essential step in optimizing its properties. A charge separation, as desired in a solar cell, should have a band alignment of type II or type III [180], and see above. ZnO with copper oxide forms a type II band alignment, favored for a perfect solar cell assembly [181]. Finally, if radiative recombination at the interface is avoided and proper alignment of the valence band of the p-type material with the conduction band of the n-type material is given, then the theoretical value of V_{OC} is given [182].

The relations between Cu_2O and ZnO was believed to be heteroepitaxial, due to the relatively small lattice mismatch of 7.6% of the $Cu_2O(111) - ZnO(0001)$ interface [16, 75]. It has been reported that the $CuO - ZnO$ interface is favorable both in strain and interface energy. This favorable situation can explain why a 5 nm thick CuO layer is formed between ZnO and Cu_2O [16, 17]. Moreover, it is an explanation for the apparent mismatch between the theoretical value and measured conversion efficiency values in the lab. In order to increase the performance of $Cu_2O - ZnO$ devices, existing methods have to be altered, or new procedures developed to create a junction that is inherently less favorable, energetically.

3. Experimental

Various experiments were conducted throughout the M.Sc. project. The sol-gel experiments prepared the foundation by resulting in powder samples later used in the creation of the pellets. By sintering the pellets, targets for the PLD were created, and the thin film deposition was enabled. To confirm the phase of various samples created, the advantages of the XRD, SEM, and TEM were used. An overview of these experiments is shown in Table 6.

Table 6: An overview of the experiments conducted, the techniques used, and the purpose of these experiments.

Experiments:	Techniques:	Purpose:
Sol-gel Experiments	Sol-gel, SEM, XRD	Creation of powders, Study of calcination behavior
Pellet Experiments	Sintering, SEM, XRD	Creation of pellets from powder Study of sintering behavior
PLD Experiments	PLD	Creation of thin film p-n-junctions
TEM Experiments	TEM Mode: Imaging + SAED STEM Mode: Imaging + EDS	Structural and chemical characterization
DFT Experiments	DFT calculations (PBE functional)	Theoretical study of interface stability

3.1. Preparation

The samples observed in the TEM had to be fabricated and prepared. The conditions for manufacturing powders, the sintering process for pellets, and deposition parameters for the thin films are explained below. Moreover, the TEM sample preparation is stated.

3.1.1. Sol-Gel Synthesis

Different sol-gel samples were manufactured. The difference between the samples is the amount of ethylene glycol, desired ZnO content, calcination temperature, and calcination time. To illustrate the process through which the powders were obtained, one example is explicitly stated below. For all the samples the initial conditions are indicated in Table 7.

A beaker was filled with 140 ml deionized water (H_2O) and 3 ml ethylene glycol ($HOCH_2CH_2OH$) to fabricate a powder containing 0.5 wt% ZnO and 99.5 wt% Cu_2O. The glass with the mixture was heated on a heating plate to 80℃ while being stirred. The copper(III)

nitrate hemipentahydrate ($Cu(NO_3)_2 \cdot 2.5\,H_2O$) and zinc nitrate hexahydrate ($Zn(NO_3)_2 \cdot 6\,H_2O$) were weighted, and the 16.2 g and 0.05 g, respectively, were added to the beaker. Slowly 3 g of citric acid ($C_6H_8O_7$) was added to the solution. The color of the mixture was a deep blue (see Figure 19 (a)). Once all the citric acid was added, the opening of the beaker was covered by aluminum foil, and the beaker left on the heating plate at 80℃ for 60 min, while being stirred. Finally, the glass was moved to a heating cabinet at 120℃, and left overnight (more than 12 h).
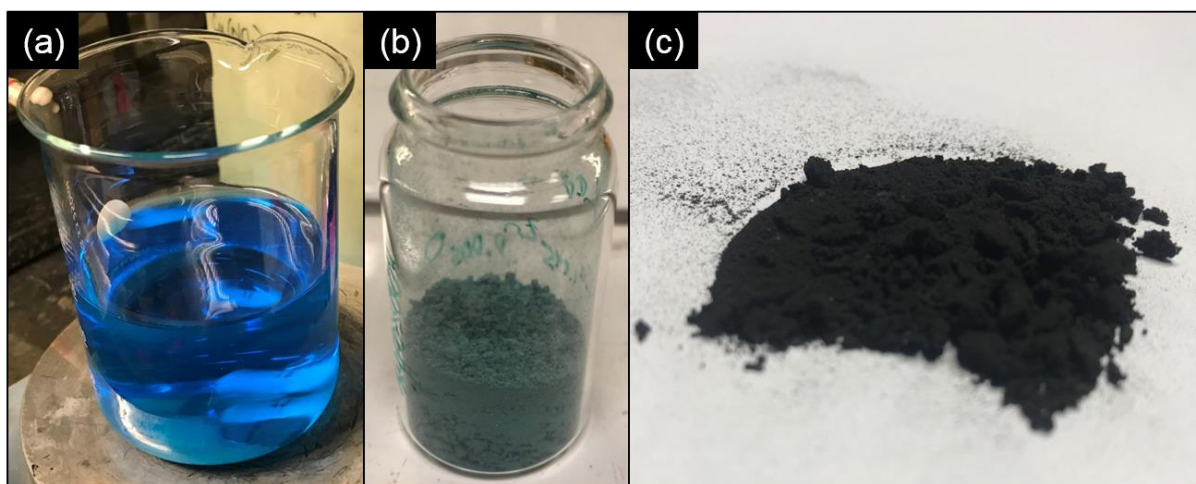

Figure 19: In (a) the mixture H_2O, $HOCH_2CH_2OH$, $Cu(NO_3)_2$, $Zn(NO_3)_2$, and $C_6H_8O_7$ on the heat plate just before covering with aluminum foil is shown. The color was a deep, see-through blue for all the samples. In (b) the obtained compound before calcination is seen. A blue-green color is characteristic for this step. The powder was subsequently heated to force a combustion reaction, and calcined in the furnace. The final powder is shown in (c). All samples appeared rather dark. However, samples 9 and 10 were slightly brighter than the rest.

The color of the now solid compound was blue-green, as shown in Figure 19 (b). After transferring all of it to a glass vial, small amounts of it were heated in an additional beaker to 250℃ to provoke a combustion reaction. The processed powder, now black, was given into an alumina crucible and covered with an alumina lid, and calcined. A similar procedure was conducted for all the other samples, except sample 10. The tenth sample was calcined directly, without provoking the combustion reaction beforehand. As a measure of precaution, less powder was calcined at once for sample 10, and the sample split in two. An overview of all the parameters is given in Table 7.

Sample Calcination

Every sample was calcined in ambient oxygen partial pressure. The crucible was placed in the furnace and subsequently heated to the target temperature. It was held at the target temperature for a sample specific calcination time, before being cooled to room temperature again. The

heating and cooling rate were kept constant, being 100°C h^{-1} and −100°C h^{-1}, respectively. The resulting powders had black to grey-black color (see Figure 19 (c)), and were analyzed by XRD.

Table 7: The Cu$_2$O sol-gel sample name, amount of ZnO and ethylene glycol, as well as calcination temperature and time, are stated. Two temperatures and times indicate samples which have been calcined twice.

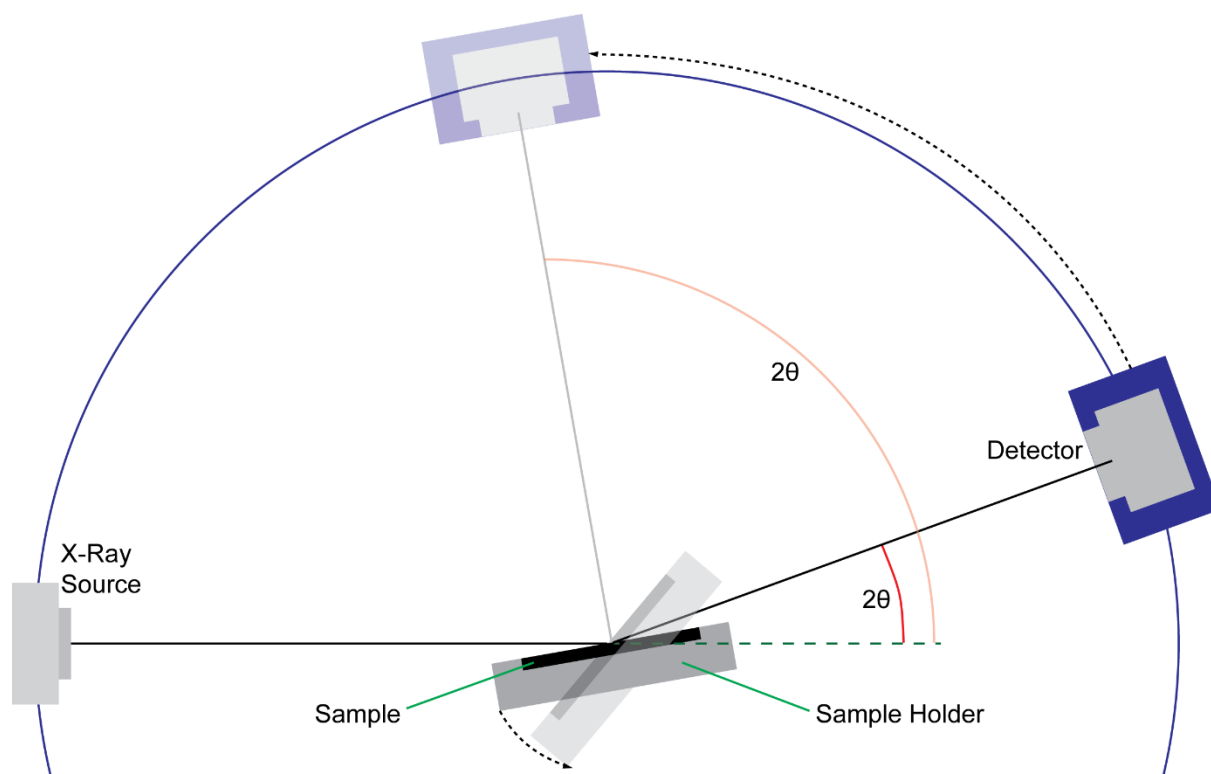| Sample:	ZnO (wt%):	Ethylene Glycol:	Calcination T:	Calcination t:
Sample 01	0.5	3 ml	900°C; 1050°C	4.5 h; 6 h
Sample 02	0.25	3 ml	900°C; 1050°C	4.5 h; 6 h
Sample 03	-	3 ml	900°C; 1050°C	4.5 h; 6 h
Sample 04	-	3 ml	350°C	10 h
Sample 05	-	5 ml	300°C	10 h
Sample 06	-	3 ml	300°C	10 h
Sample 07	-	3 ml	265°C	10 h
Sample 08	-	3 ml	285°C	12 h
Sample 09	10	3 ml	300°C	12 h
Sample 10	10	3 ml	200°C	12 h

Sol-Gel XRD Preparation

Figure 20: A sketch of the working principle of the Rigaku Miniflex X-Ray Diffractometer. The source is immobile, and the required tilting for the measurement is achieved by tilting the sample and moving the detector. Additionally, the 2θ angle is indicated.

3. Experimental

An XRD pattern was taken from every sample and they are shown in section 4. If a sample was calcined twice, an XRD pattern was taken after each calcination. A small amount of powder was transferred to a mortar and crushed to tiny particles by a pestle to prepare the sample for the analysis. If a marker was used, a well-characterized material, Si (NIST 640d), was added to detect shifts in the measurements due to the measurement setup. A small amount of the marker was added to the crushed powder sample and mixed with a small amount of isopropanol. After drying the mixture in air, the powder was transferred onto a sample holder and placed in the X-ray diffractometer (Rigaku Miniflex X-Ray Diffractometer). The working principle of the specific apparatus is shown Figure 20. An XRD pattern was taken, typically from $10°$ to $90°$, with $0.1°$ step-size, and $1.0°$ min^{-1}, if not stated otherwise. Additionally, one powder was observed by SEM.

3.1.2. Pellet Manufacturing

The powders fabricated according to the sol-gel method described in section 3.1.1 were used to make Cu_2O pellets. Moreover, ZnO powder was used to create ZnO pellets. The Cu_2O and ZnO pellets were sintered at different temperatures and atmosphere-composition due to thermodynamics as discussed in section 2.8. These pellets can be used in a variety of ways, e.g., as targets in a PLD thin film manufacturing method. Two distinct steps are needed to manufacture a pellet: the pressing and the sintering. There are a variety of parameters in both steps that can be altered to achieve the best result, and they are typically material dependent.

The powder for each pellet was crushed in a mortar with a pestle. It was then weighted, and the appropriate amount for the desired pellet size was given back into the mortar. For each gram of powder, 17 drops of binder (B60/B709, Mix with ethyl acetate) were added and mixed into the powder with a pestle. The powder-binder mix was then transferred into a die, with a pressing area according to Table 8. The diameter was typically chosen according to the subsequent setup and use of the pellet. Moreover, 1.5 g of powder was used for the smaller area, and 2.5 g of powder for the larger pellet. Additionally, three heavy pellets of 6 g were made, one with pure Cu_2O (Sigma Aldrich, CAS Number 1317-39-1), one with pure ZnO, and one with 3 g or Cu_2O and 3 g of ZnO. For these heavier pellets, the larger dye was used. For all the pellets fabricated, the pressure used was approximately six tons on the scale of the press (Atlas Manual Hydraulic Press 15T, Specac). Typically, a higher force results in a denser pellet. However, cracking of the pellet, as well as possible material changes have to be taken into

consideration. The force was applied to a different area when the diameter of the die changed. Thus, while the force remained the same, the pressure changed according to the total area:

$$p = \frac{F}{A} \tag{75}$$

where p is the pressure, F the force, and A the area. The differences are summarized in Table 8. These differences were especially crucial for the Cu_2O and their properties in the PLD.

Table 8: The Cu_2O powder samples and ZnO powders, with the corresponding pressing area, pressure, and final pellet name are stated. The smaller pellets were made with 1.5 g and the larger pellets with 2.5 g powder unless noted otherwise. For each pellet, 58800 N of force was used. Letters a and b indicate that two pellets have been manufactured using powder from the same sol-gel sample.

Powder Sample:	Area:	Pressure:	Pellet:
ZnO	4.91×10^{-4} m^2	11.98×10^7 Nm^{-2}	ZnO try
ZnO (4 times)	4.91×10^{-4} m^2	11.98×10^7 Nm^{-2}	ZnO 1 - 4
ZnO (6 g)	4.91×10^{-4} m^2	11.98×10^7 Nm^{-2}	ZnO (heavy)
Sample 01	4.91×10^{-4} m^2	11.98×10^7 Nm^{-2}	Cu_2O 1
Sample 02	4.91×10^{-4} m^2	11.98×10^7 Nm^{-2}	Cu_2O 2
Sample 03 a	1.33×10^{-4} m^2	44.24×10^7 Nm^{-2}	Cu_2O 3a
Sample 03 b	1.33×10^{-4} m^2	11.98×10^7 Nm^{-2}	Cu_2O 3b
Sample 04 a	4.91×10^{-4} m^2	11.98×10^7 Nm^{-2}	Cu_2O 4a
Sample 04 b	4.91×10^{-4} m^2	11.98×10^7 Nm^{-2}	Cu_2O 4b
Sample 05 a	1.33×10^{-4} m^2	44.24×10^7 Nm^{-2}	Cu_2O 5a
Sample 05 b	1.33×10^{-4} m^2	44.24×10^7 Nm^{-2}	Cu_2O 5b
Sample 06 a	1.33×10^{-4} m^2	44.24×10^7 Nm^{-2}	Cu_2O 6a
Sample 06 b	4.91×10^{-4} m^2	11.98×10^7 Nm^{-2}	Cu_2O 6b
Sample 07 a	4.91×10^{-4} m^2	11.98×10^7 Nm^{-2}	Cu_2O 7a
Sample 07 b	4.91×10^{-4} m^2	11.98×10^7 Nm^{-2}	Cu_2O 7b
Sample 08	4.91×10^{-4} m^2	11.98×10^7 Nm^{-2}	Cu_2O 8
Sample 09	4.91×10^{-4} m^2	11.98×10^7 Nm^{-2}	Cu_2O 9
Sample 10 a	1.33×10^{-4} m^2	44.24×10^7 Nm^{-2}	Cu_2O 10a
Sample 10 b	1.33×10^{-4} m^2	44.24×10^7 Nm^{-2}	Cu_2O 10b
Cu_2O (3 g)	4.91×10^{-4} m^2	11.98×10^7 Nm^{-2}	Cu_2O SA
Cu_2O (6 g)	4.91×10^{-4} m^2	11.98×10^7 Nm^{-2}	Cu_2O (heavy)
Cu_2O/ZnO	4.91×10^{-4} m^2	11.98×10^7 Nm^{-2}	Mix

Pellet Sintering

During the sintering process, two parameters can be controlled. The first is temperature. For the ZnO pellets, 1400℃ was chosen as temperature. The Cu_2O targets were sintered at various temperatures, given in Table 9. The second parameter adjustable in the sintering process was

3. Experimental

oxygen partial pressure. While the ZnO samples were sintered at ambient oxygen partial pressure, the Cu_2O targets were sintered in argon (Ar) and Harmix (95% Ar mixed with 5% H_2).

Table 9: The pellets, with the corresponding sintering temperature, ramp rate, sintering atmosphere (where argon is Ar, and Harmix is 95% Ar + 5% H_2), and cooling procedure are summarized in this table. The quenching procedure has no cooling rate, as the rate varied over the time of cooling.

Pellet:	Sintering T:	Ramp Rate:	Sintering Atmosphere:	Cooling Procedure:
ZnO try	1400°C	4.67°C min^{-1}	Ambient	Controlled, -4.67°C min^{-1}
ZnO 1 - 4	1400°C	4.67°C min^{-1}	Ambient	Controlled, -4.67°C min^{-1}
ZnO (heavy)	1400°C	4.67°C min^{-1}	Ambient	Controlled, -4.67°C min^{-1}
Cu_2O 1	1090°C	5°C min^{-1}	Ar	Quenching in Ar + Harmix
Cu_2O 2	1050°C	5°C min^{-1}	Ar	Quenching in Ar
Cu_2O 3a	1050°C	5°C min^{-1}	Ar	Controlled Ar, -10°C min^{-1}
Cu_2O 3b	1000°C	5°C min^{-1}	Ar	Controlled Ar, -10°C min^{-1}
Cu_2O 4a	1000°C	5°C min^{-1}	Ar	Quenching in Ar
Cu_2O 4b	1000°C	5°C min^{-1}	Ar	Quenching in Ar + Harmix
Cu_2O 5a	1025°C	5°C min^{-1}	Ar	Quenching in Ar + Harmix
Cu_2O 5b	1050°C	5°C min^{-1}	Ar	Quenching in Ar + Harmix
Cu_2O 6a	1000°C	5°C min^{-1}	Ar	Quenching in Ar + Harmix
Cu_2O 6b	1050°C	5°C min^{-1}	Ar	Quenching in Harmix
Cu_2O 7a	1025°C	5°C min^{-1}	Ar	Quenching in Ar + Harmix
Cu_2O 7b	1050°C	5°C min^{-1}	Ar	Quenching in Ar + Harmix
Cu_2O 8	1050°C	5°C min^{-1}	Ar	Quenching in Ar + Harmix
Cu_2O 9	1050°C	5°C min^{-1}	Ar	Quenching in Ar + Harmix
Cu_2O 10a	1073°C	5°C min^{-1}	Ar	Quenching in Ar + Harmix
Cu_2O 10b	1050°C	5°C min^{-1}	Ar	Quenching in Ar + Harmix
Cu_2O SA	425°C	5°C min^{-1}	Harmix	Controlled (Harmix),-10°C min^{-1}
Cu_2O (heavy)	475°C	5°C min^{-1}	Harmix	Quenching in Harmix
Mix	475°C	5°C min^{-1}	Harmix	Quenching in Harmix

For the Cu_2O samples, the cooling procedure was varied to find the ideal cooling conditions. The four appropriate cooling methods are: Controlled cooling in Ar, quenching in Ar, controlled cooling in Ar mixed with Harmix (95% Ar + 5% H_2), and quenching in Ar mixed with Harmix. The summary of all conditions is stated in Table 9. There are several experimental setup changes made. First, sample crumbling was observed in sample Cu_2O 4b. The setup was adjusted to prevent the crumbling of the bigger samples. Second, sample Cu_2O 5b was sintered twice, and the second time the ProboStat was flushed with Harmix before sintering. The

procedure was used for every sample but Cu_2O 4a, Cu_2O 4b, Cu_2O 5a, and the first sintering of Cu_2O 5b.

Moreover, while no sacrificial powder was used in the sintering process of Cu_2O pellets, for every ZnO pellet some sacrificial ZnO powder was used to prevent significant evaporation of ZnO from the pellet during the sintering (as observed in [181, 183]). The resulting pellets were observed by SEM. Some of the pellets were manufactured similarly than another pellet. Typically, one was treated as a possible target in a PLD, while the other one was characterized.

3.1.3. Pulsed Laser Deposition Fabrication

The PLD was used to deposit various thin films of Cu_2O and ZnO on Si substrates. During the deposition, a multitude of parameters can be controlled. The PLD itself offers various options to re-adjust mirrors and lenses. Several vital parameters were altered to obtain the films created, including moving and cleaning of mirrors and lenses. These parameters are the target to substrate height h, substrate temperature, substrate position, laser intensity, and the number of shots.
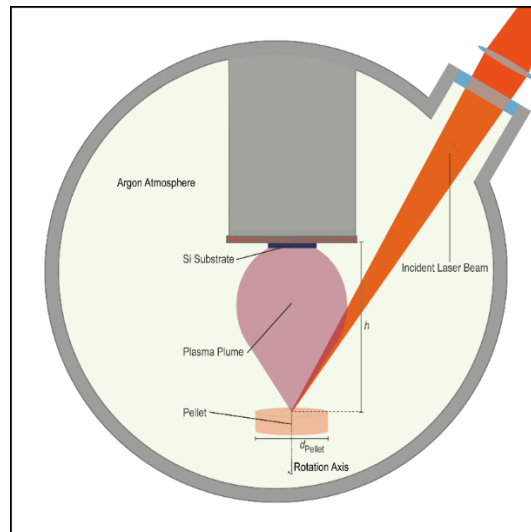

Figure 21: The PLD chamber with an incident laser beam, the rotating target pellet, created plasma plume, height h, and Si substrate on the heater.

The conditions for a successful deposition of each oxide were different, and they are stated in Table 10. The atmosphere during deposition was chosen to be Ar, with a pressure of 10^{-3} mbar. The temperature and height were varied for the different samples. The height of the substrate determines how close the plume is to the surface of the substrate and how uniform the film is deposited. In general, a higher substrate results in a more uniformly deposited film. However, the thickness of the film decreases. The temperature range of the PLD was between

3. Experimental

room temperature and 600℃. Higher temperature increases the quality of the film. However, in the case of Cu_2O, a temperature of 600℃ in combination with oxygen availability could result in the formation of CuO.

Table 10: The oxide and corresponding laser intensity and the number of shots with resulting film thickness as used and obtained in the PLD in the Electrochemistry Lab are shown.

Oxide:	Laser	Number of Shots:	Film Thickness:	Height h:
ZnO	190 mJ	10 000	~550 nm	5 cm
Cu_2O	200 mJ	30 000	~135 nm	5 cm

The best results were achieved by heating the substrate to 300℃. Moreover, the targets were rotated with 5 RPM. The corresponding number of shots and intensities for each target material are recorded in Table 10. The resulting films were observed by the TEM and showed uniform thickness. Of the 23 thin films manufactured during this work, only two had a visible plume while shooting at the Cu_2O target. The critical parameter was the intensity of the laser reaching the target and forming a plume. The stated intensities in Table 10 indicate the programmed intensities; however, before cleaning the lenses, only a fraction of it reached the target.

3.1.4. TEM Sample Preparation

The thin films were processed into a TEM samples. TEM samples are typically very thin ($\sim$ 10 nm for high-resolution TEM (HRTEM)). To observe the junction between the two-deposited films, the cross-section of the sample has to be studied. First, the samples were observed by an optical microscope, and a drawing of the features, including the dimensions, was made. Subsequently, an area of $\sim$3 × 6 mm or two areas of $\sim$3 × 3 mm was selected to make a so-called "sandwich". Crystal-bond was used to glue the sample on a glass substrate, and a micro-saw used to cut the pieces.

The pieces were arranged such that one piece was rotated 90° around the growing direction axis, and two-component glue used to glue the two films on top of each other. This reorientation enables the observation of both axis perpendicular to the growing direction in the TEM. The glue was cured for 10 minutes on a heat plate and then left overnight. The next day, the sample was cut into two in the direction perpendicular to the observed side.

The sample was then glued onto a holder with Loctite before thinned to 500 μm, on one side perpendicular to the observed side. The sample was then rotated in such a manner that the

other side could be thinned, and towards the end of the thinning process, a wedge was introduced. The wedge allowed the tip of the sample to be thinner than 50 µm. A copper ring was glued on top of the sample, such that the thinnest part of the sample was in the center of the ring. The part of the sample outside the copper ring was cut off, to ensure that the sample fits the TEM setup perfectly. The procedure is depicted in Figure 22.

After leaving the sample overnight, it was mounted in a PIPS II system (Precision Ion Polishing System II, Gatan Inc.) and thinned further. Due to the relative hardness of the film compared to the Si, the thinning process had to be controlled in such a manner that substrate and film survived the procedure. The samples were then studied in the JEOL 2100F.
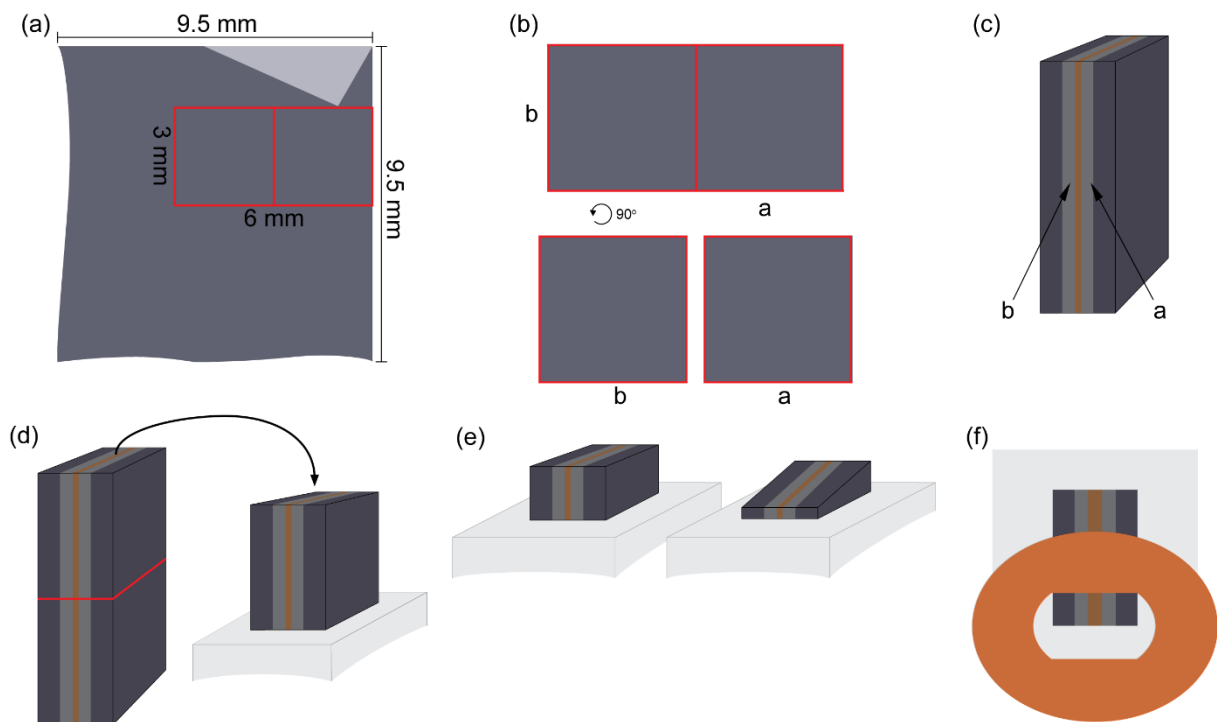

Figure 22: The preparation of the TEM sample. (a) shows a sample as observed, with a 3×6 mm area marked to cut out. The light area above indicates an area with no deposition. (b) shows the two 3×3 mm cuts, with a and b marking the observed sides, originally 90° to each other. (c) shows the sandwich with sides a and b marked again. (d) indicates the cut direction to half the sandwich, and half of the sandwich placed on a sample holder. (e) depicts a thinned sample on the left and the right a sample with a wedge, considerably thinner than the original sandwich. (f) shows the placement of the ring on the sandwich, before cutting off the parts outside the ring and using a PIPS II to thin the sandwich further.

3.2. Density Functional Theory Calculations

The interfaces calculated are selected according to the orientations of the ones encountered in literature. They are: for Cu_2O the [111] and [110], for cupric oxide the [100], and zinc oxide the [0001] orientation. This leads to the following interfaces of interest: Cu_2O (111) – ZnO (0001), Cu_2O (110) – ZnO (0001), CuO (100) – Cu_2O (111), CuO (100) – Cu_2O (110), and CuO

3. Experimental

(100) – ZnO (0001). To find the most stable, relative position for the two crystals of each interface, a multitude of interfaces, with one crystal slightly shifted relative to the other one was calculated, as illustrated in Figure 23. One hundred such shifts yield good coverage of the unit cell and have been calculated for each interface. The structures were created similar to the structures in [184].
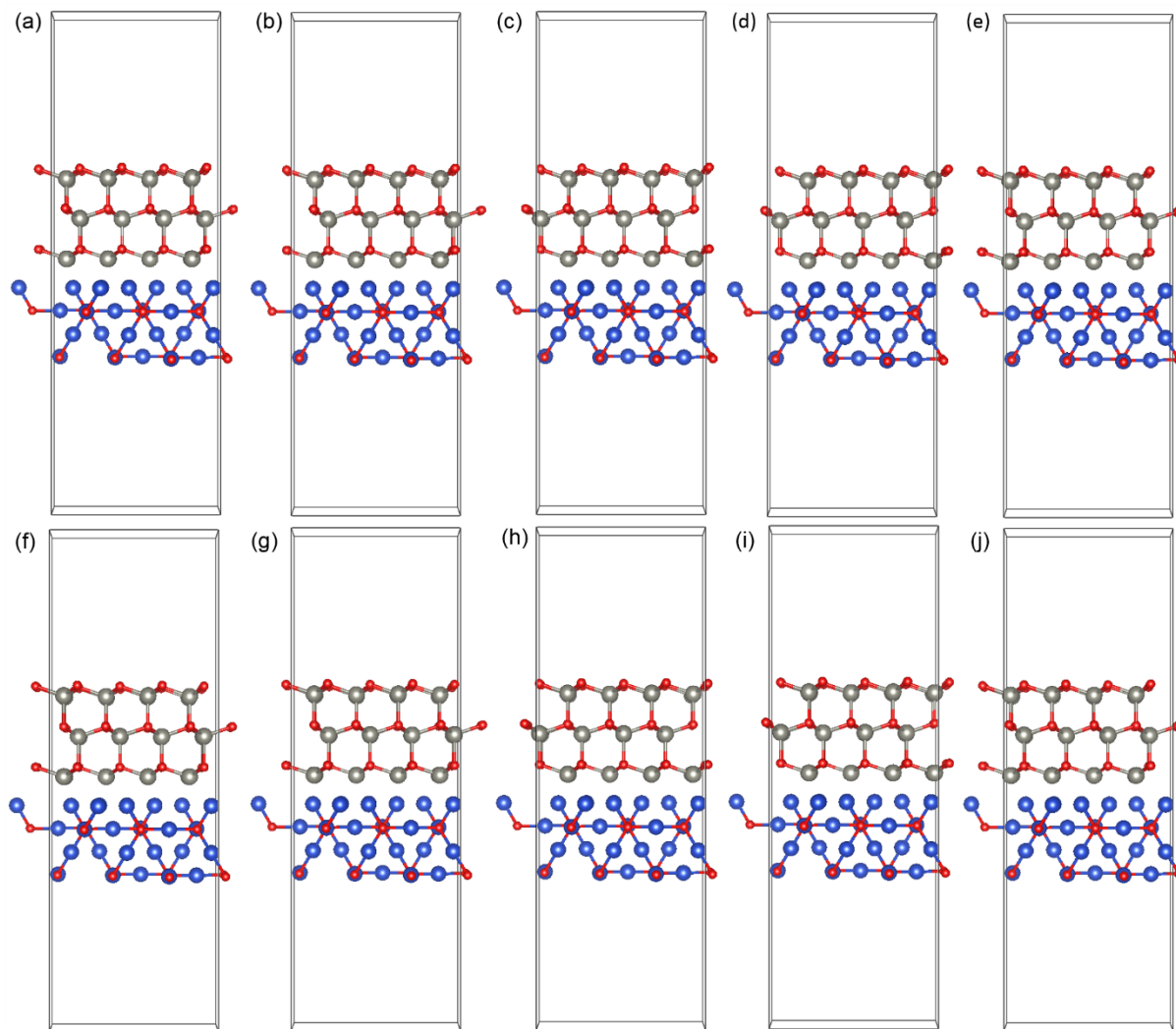

Figure 23: A series of ten interfaces between Cu_2O (110) (bottom structure) and ZnO (0001) (top structure). The ZnO is slightly shifted in each image (a) – (j). After the last image, the first position is assumed again. This procedure was repeated for all the interfaces.

While those one hundred different structures enable the calculation of the entire unit cell, it is essential to notice that only a quarter of the unit cell has been mapped. The other three quarters would yield similar results due to the symmetry of these unit cells. Moreover, while the movement of the slab defined the *a* and *b* coordinate of the moved crystals, the *c* direction was fixed by defining the minimal distance between the two closest atoms to 1.93 Å. Relaxing all these structures, and comparing the energy to the two slabs separated by vacuum was the

last step and yielded the energy gained by creating the interface. The potential used was a PAW with a PBE exchange-correlation function [185, 186].

3.2.1. Convergence

The convergence of the relative energy was ensured by systematically comparing the total energy of different energy cutoffs with each other and comparing them to another set of total energies. Subsequently comparing the total energy of different k-point densities to each other, and another set of total energies. For each of those properties, a convergence criterion has been defined beforehand, and all systems were adjusted to fit these criteria.

The first step was ensuring the minimum energy cutoff to ensure the convergence of relative energy if an atom was moved by 2×10^{-2} Å. A proper relative energy convergence occurred if

$$\frac{\Delta E_{\text{Relative}}}{\Delta E_{\text{Cutoff}}} < \frac{1 \text{ meV}}{50 \text{ eV}} \tag{76}$$

where $\Delta E_{\text{Relative}}$ is the difference in relative energies between the systems, and ΔE_{Cutoff} the difference in cutoff energies. The minimal cutoff energy fitting the criterion was used for each system.

The second step is determining the minimum k-point density needed to achieve the convergence in relative energy again. Two sets of calculations are used, where one set has an atom moved by 2×10^{-2} Å. The convergence criterion in this case was

$$\frac{\Delta E_{\text{Relative}}}{\Delta N_k} < \frac{1 \text{ meV}}{1} \tag{77}$$

where ΔN_k is the difference in the number of k-points in each direction. Again, the minimal number of k-points was determined for each system and used during the relaxation and calculations presented in section 4.

3.2.2. Calculations

The calculations conducted were based on the convergence values previously described. With these values, each interface was first calculated in its initial state without relaxing the structure. Additionally, the structures were relaxed, to minimize their energies before the relaxed structures were used as the input files for the re-calculation. Simultaneously, the two crystals were calculated in a slab configuration, meaning vacuum was introduced between the two

3. Experimental

oxides. The slab configuration allows the determination of the energy gained by forming an interface and two surfaces, rather than four surfaces.

Table 11: The a and b length for the bottom (a_B and b_B) and the top (a_T and b_T) oxide of the p-n-junction. The values d_1 and d_2 represent the fraction (a_B/a_T and b_B/b_T), respectively, indicating how similar the lengths are. The closer d_1 and d_2 are to whole numbers, the better the match between the cells.

Interface	Bottom	Top	a_B	b_B	a_T	b_T	d_1	d_2
1	CuO (100)	Cu$_2$O (111)	5.13	3.42	3.02	3.02	1.70	1.13
2	CuO (100)	Cu$_2$O (110)	4.68	5.80	4.25	5.07	1.10	1.14
3	Cu$_2$O (111)	ZnO (0001)	3.02	3.02	3.25	3.25	0.93	0.93
4	Cu$_2$O (110)	ZnO (0001)	3.70	5.23	3.25	5.63	1.14	0.92
5	CuO (100)	ZnO (0001)	3.42	8.55	3.25	8.60	1.05	0.99

This means that for each of the 5 interfaces 100 structures were created, calculated, relaxed, recalculated, and evaluated. Moreover, the slabs were calculated in the same manner, although only one per interface. Finally, the calculated energies are shown in section 4.4. Table 11 indicates how well the repeating motives in the direction of the supercell match. In Table 12 the height of the slabs as used in the interfaces as well as the number of anions and cations are listed.

Table 12: The height of the individual slab (first number: bottom, second number: top, one number: both) as well as the anions and cations of the oxides use in the interfaces.

Interface	Height (Å)	# Anions (B)	# Cations (B)	# Anions (T)	# Cations (T)
1	8.05, 7.39	12	12	26	52
2	10.46, 13.58	38	38	30	60
3	13.6	12	24	24	24
4	5.83, 5.40	12	23	24	24
5	8.15, 9.81	24	24	24	24

3.2.3. Limitations

The calculations, despite being limited in their scope, are limited by the functional, types of calculations, and models used. For example, surfaces can be classified by their termination, according to P.W. Tasker [187]. Type 1 contains equal number of anions and cations in each plane, and has thus neutral surfaces. Type 2 has charged planes, meaning a different number of anions and cations in each plane, but no dipole normal to the surface. Finally, type 3 describes a charged surface with a dipole normal to the surface. For the system at hand, the following

classification can be made: Cu_2O (110) and Cu_2O (111) are type 2, and all the others are type 3.

A second limitation is the choice of functional. The PBE functional notoriously underestimates the band gap of semiconductors. Among the biggest differences between measurement and calculated bandgap is ZnO. Hence, density of states plots and band properties will not be represented correctly [122]. The following electron configurations are used in the potential for the different elements:

- O: s2 p4
- Cu: d10 p1
- Zn: d10 p2

The third limitation originates by using a slab model. There are a two critical points that have to be taken into account: First, the slab must be thick enough such that surface-surface interactions within the slab do not occur, and a bulk like interior is given [122]. Second, to mimic a 2D periodicity in the 3D setup, a vacuum layer thick enough to shield the slab from interacting in one direction has to be introduced [122]. Moreover, the Tasker-classification has to be taken into account.

4. Results

The results obtained by the various experiments and calculations are shown below. An interpretation of the results will be given in section 5. The order of reporting is the same as in section 3.

4.1. Sol-Gel Synthesis

The XRD patterns of the powders are displayed below. The XRD's were taken in the Rigaku MiniFlex X-Ray Diffractometer. The diffractometer uses copper the K-α 1 energy, with a wavelength λ = 1.5406 Å and energy of 8.04 keV. All samples that contain Cu atoms show at least one copper oxide phase. Moreover, despite its usefulness, the Si tracer was not used in every sample.
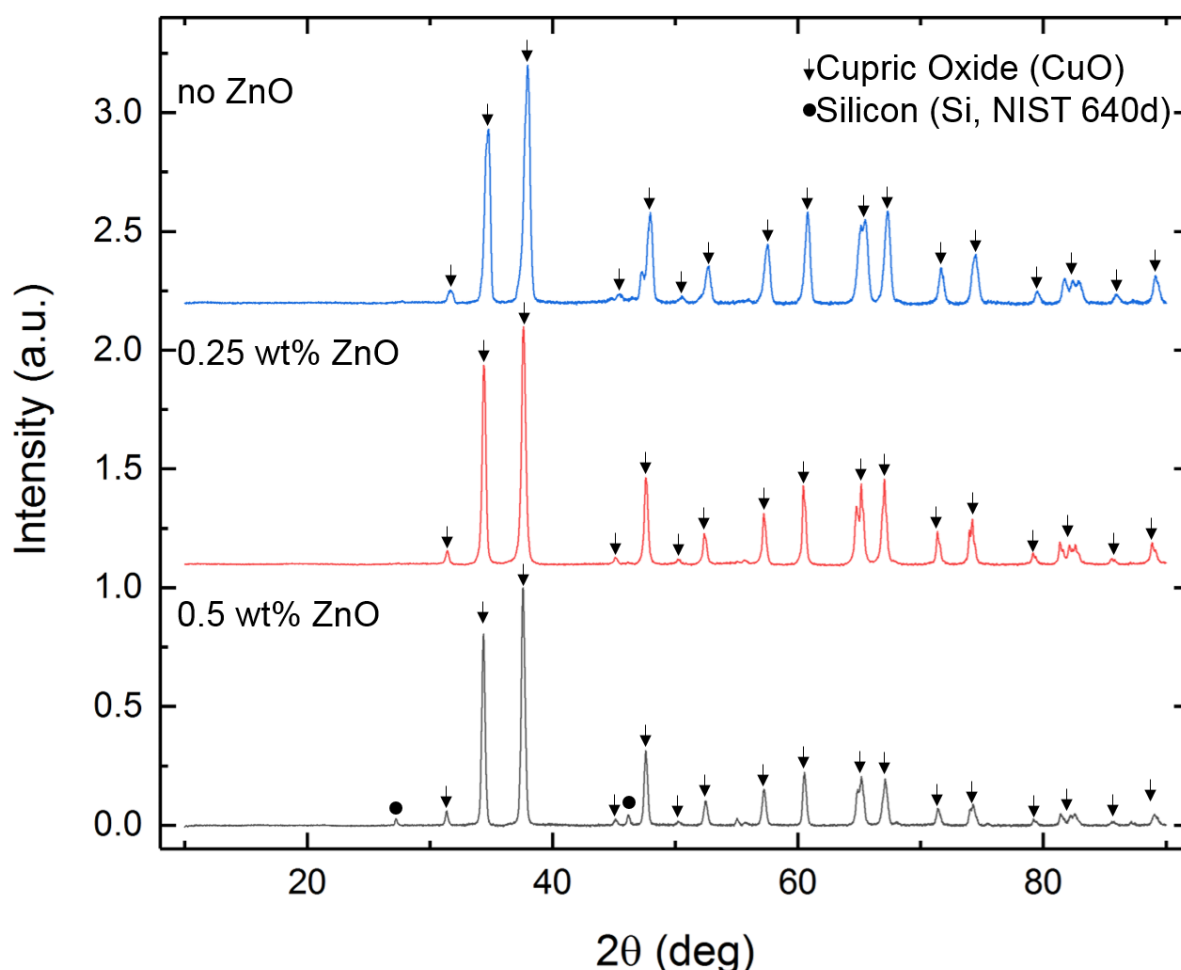

Figure 24: The XRD patterns for three samples calcined at 900℃. They differ in ZnO content in each sample. However, the graphs are similar, showing the same copper oxide phase. All the peaks, except the Si-tracer peaks in the bottom graph, corresponding to the CuO phase. The samples are sample 01 (black), sample 02 (red), and sample 03 (blue) of the sol-gel experiments.

4. Results

The XRD instrument measured the patterns with good comparability, as is evident in Figure 24. The patterns in Figure 24 depict samples calcined at 900℃. A Si marker was used in the lowest sample (sample 01, black). All other peaks have been identified as CuO phase. Figure 25 depicts XRD's of the same samples as in Figure 24. However, before taking an XRD, the samples were heated to 1050℃. The peaks have been identified to be the CuO, Cu_2O, and if used Si tracer phase (black and blue graph in Figure 25). No ZnO phase could be observed.
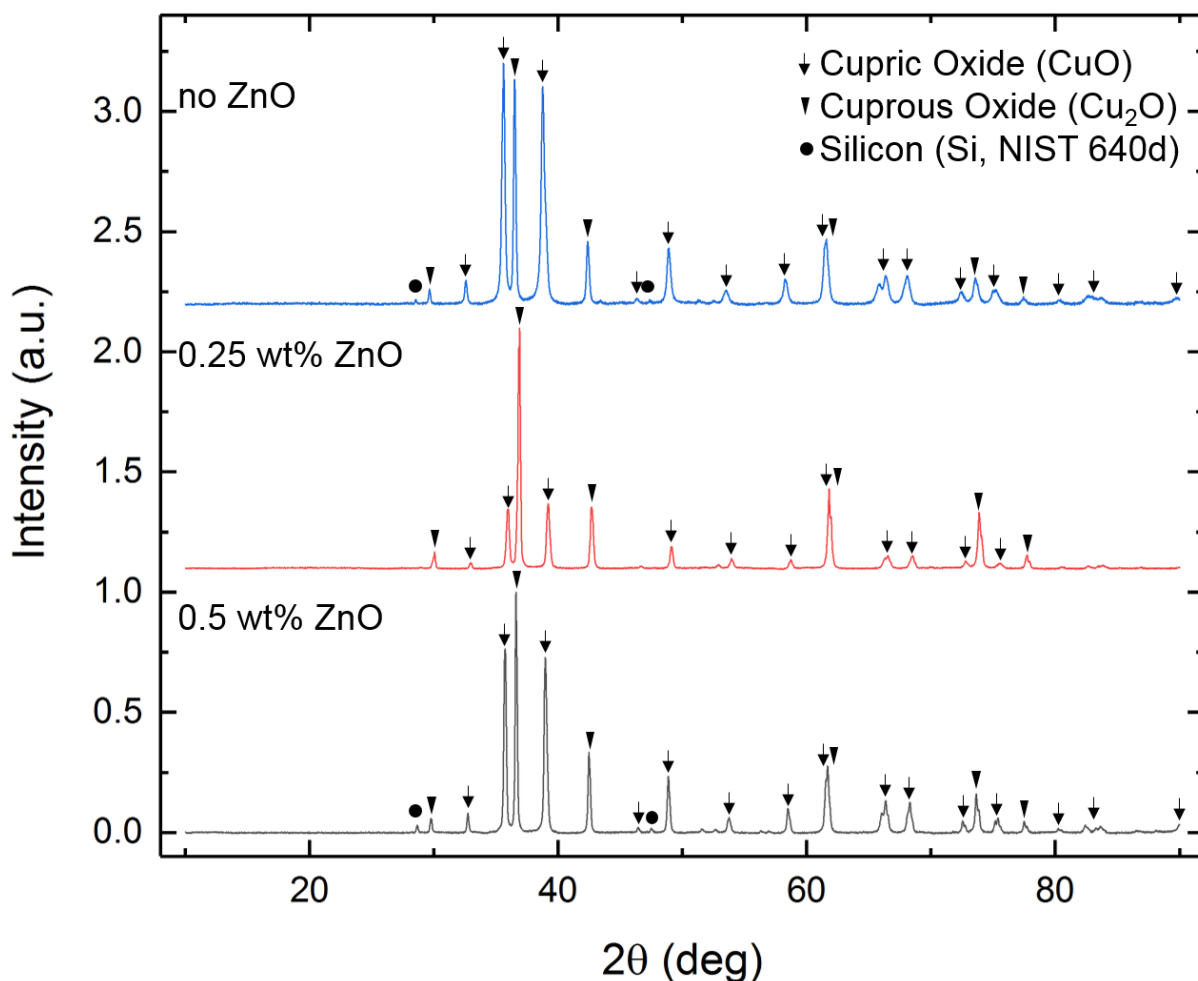

Figure 25: The XRD patterns of the same three samples as in Figure 24 after being heated to 1050℃. While they still differ in ZnO content, neither one shows a ZnO phase. However, all three show both, the Cu2O and the CuO phase. For sample 01 (black) and sample 03 (blue), the Si tracer was used.

The remaining samples were calcined at lower temperatures. In Figure 26, a sample calcined at 300℃ and two calcined at 350℃ are shown. Additionally, two had the normal concentration of ethylene glycol during the manufacturing process and one a higher one. The samples with a regular concentration of ethylene glycol show the Cu, CuO, and Cu_2O phases. The CuO peaks are lower in the low-temperature sample than in the higher temperature one.

Simultaneously, the Cu peaks are higher in the sample calcined at 300℃ than in the one calcined at 350℃.
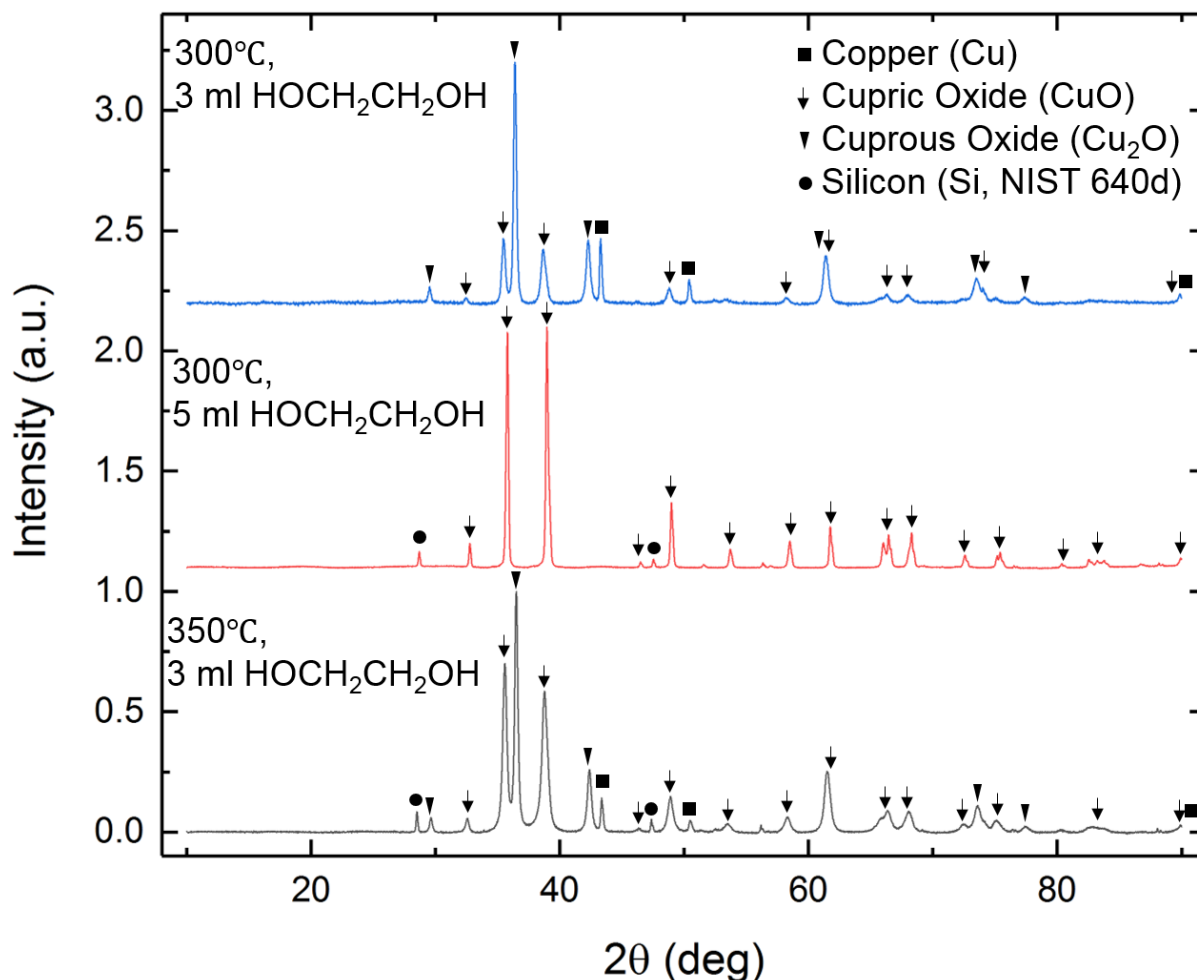

Figure 26: Three samples, where the bottom one is calcined at a higher temperature than the other two and the second sample (red) has a higher ethylene glycol content in the sample. A Si-tracer was used in those two samples. They correspond to sample 04 (black), sample 05 (red), and sample 06 (blue).

The sample with higher ethylene glycol concentration shows the CuO phase exclusively, besides the Si-tracer. Figure 27 shows three samples calcined at 285℃, 265℃ and 300℃, respectively. The two first samples show Cu, CuO, and Cu_2O, and the Si tracer in the pattern. They differentiate especially in the region from 50° to 70°. The sample sintered at 300℃ contained 10 wt% ZnO. It contained the Si-tracer, Cu, CuO, Cu_2O, and ZnO as separate phases.

The XRD of the last powder sample displayed, with 10 wt%, is shown in Figure 29. It reveals Cu, Cu_2O, and ZnO as phases in the sample. Moreover, an XRD of ZnO is depicted in the same figure. All the XRD plots were normalized, with their highest peak set as 1. Hence, the relative height between the peaks is comparable.
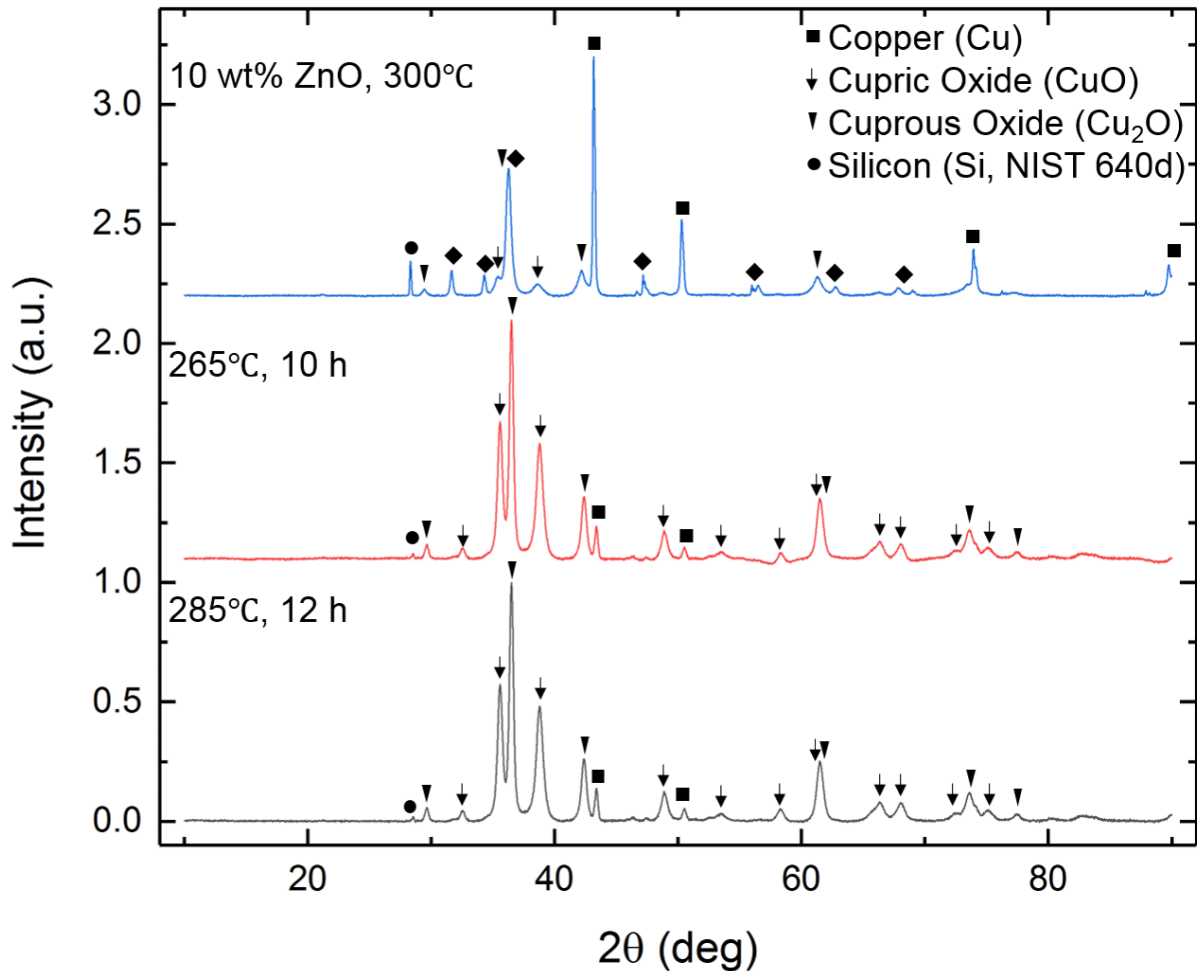
4. Results

Figure 27: Three different samples calcined at 285℃, 265℃, and 300℃, respectively. They all contained the Si-tracer, Cu, CuO, and Cu₂O. Also, the sample containing 10 wt% ZnO showed a clear ZnO phase. The corresponding samples are sample 07 (black), sample 08 (red), and sample 09 (blue).

All the XRD patterns presented in this section, including the ZnO pellet, show multiple orientations of every phase present. As the orientation of the grain is not of particular interest except in the thin films, the graphs with the respective orientation labeling are shown in Appendix C. Moreover, two of the sol-gel samples were observed by a scanning electron microscope and is shown in Figure 28. The images were taken after heating the samples to 900℃. The results will be interpreted in section 5.

The peak ratio of the two most prominent CuO orientations over all the powder samples differentiates substantially, especially in Figure 24, the red sample in Figure 25, and the red sample in Figure 26. In those graphs, the first prominent CuO peak ($2\theta \sim 36°$) appears smaller than the second large CuO peak ($2\theta \sim 39℃$). In contrary to other samples where the former is larger than the latter. This difference can also be found in the literature [188, 189].
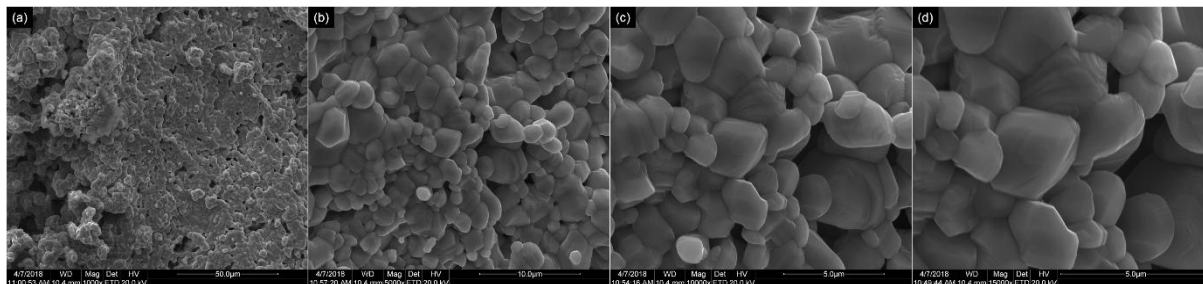
Figure 28: Four SEM pictures taken of sol-gel sample 01. (a) An overview of the powder observed is given, whereas (b), (c), and (d) reveal that the individual grains have a diameter of up to 2.5 μm. They agglomerate to bigger particles. No distinct second phase can be distinguished.
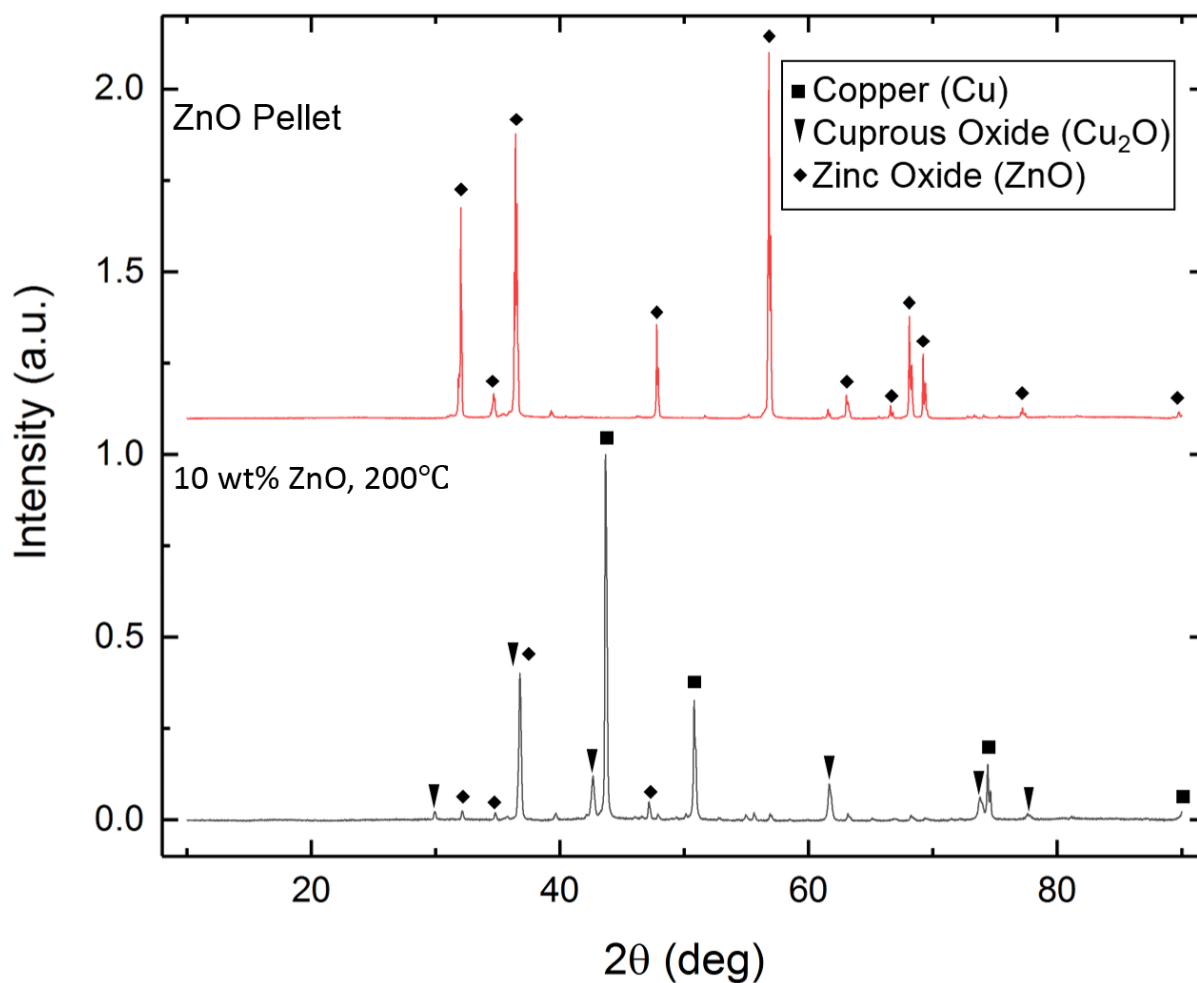

Figure 29: One powder sample and one ZnO pellet sample. The copper-based sample contained 10 wt% ZnO. The sample shows the Cu, Cu₂O, and ZnO phase. It is the sample 10 (black). The ZnO pellet (red) shows the ZnO phase, and no other.

4.2. Pellet Fabrication

The pellets created were studied before being used as targets for the PLD. Some of the pellets were broken apart to study the bulk properties of the material closer. The differences within the samples due to the change in sintering conditions will be discussed in section 5.

4. Results

The XRD results of the different pellets manufactured are shown below. The XRDs were taken of the surface if not noted otherwise. It is expected that the XRD will penetrate the surface of the pellets, and the bulk structure will dominate the graph, compared to the surface structure. Figure 30 shows three XRD patterns from two different pellets. One pellet was sintered at 1090°C, a surface XRD was taken, and the pellet was subsequently crushed, and another XRD was taken (black and red). The sample contained the Cu_2O, the CuO and the Cu phase. The second pellet was sintered at 1050°C. Its constitution included the Cu_2O phase and the CuO phase; however, the ratio between the peaks differs between each graph.
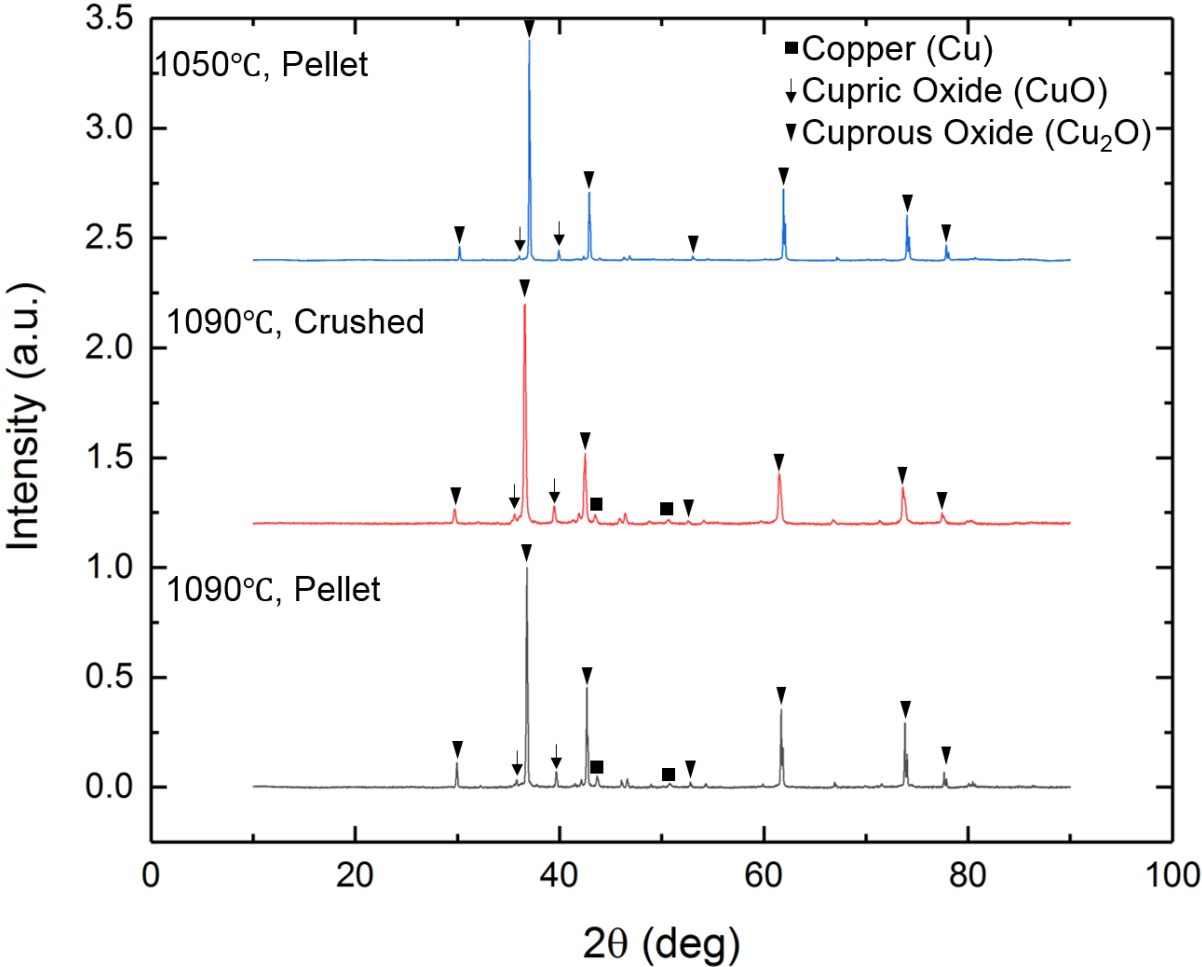

Figure 30: The XRD pattern for a pellet sintered at 1090°C, the crushed powder of that sample, and a sample sintered at 1050°C. The first pellet was quenched in Ar + Harmix, and the second pellet was cooled controlled in Ar. The quenched pellet had a Cu_2O, CuO, and Cu phase, while the other sample only had the Cu_2O and CuO phase. The samples displayed are Cu_2O 1 (black), the crushed Cu_2O 1 (red), and sample Cu_2O 3 (blue)
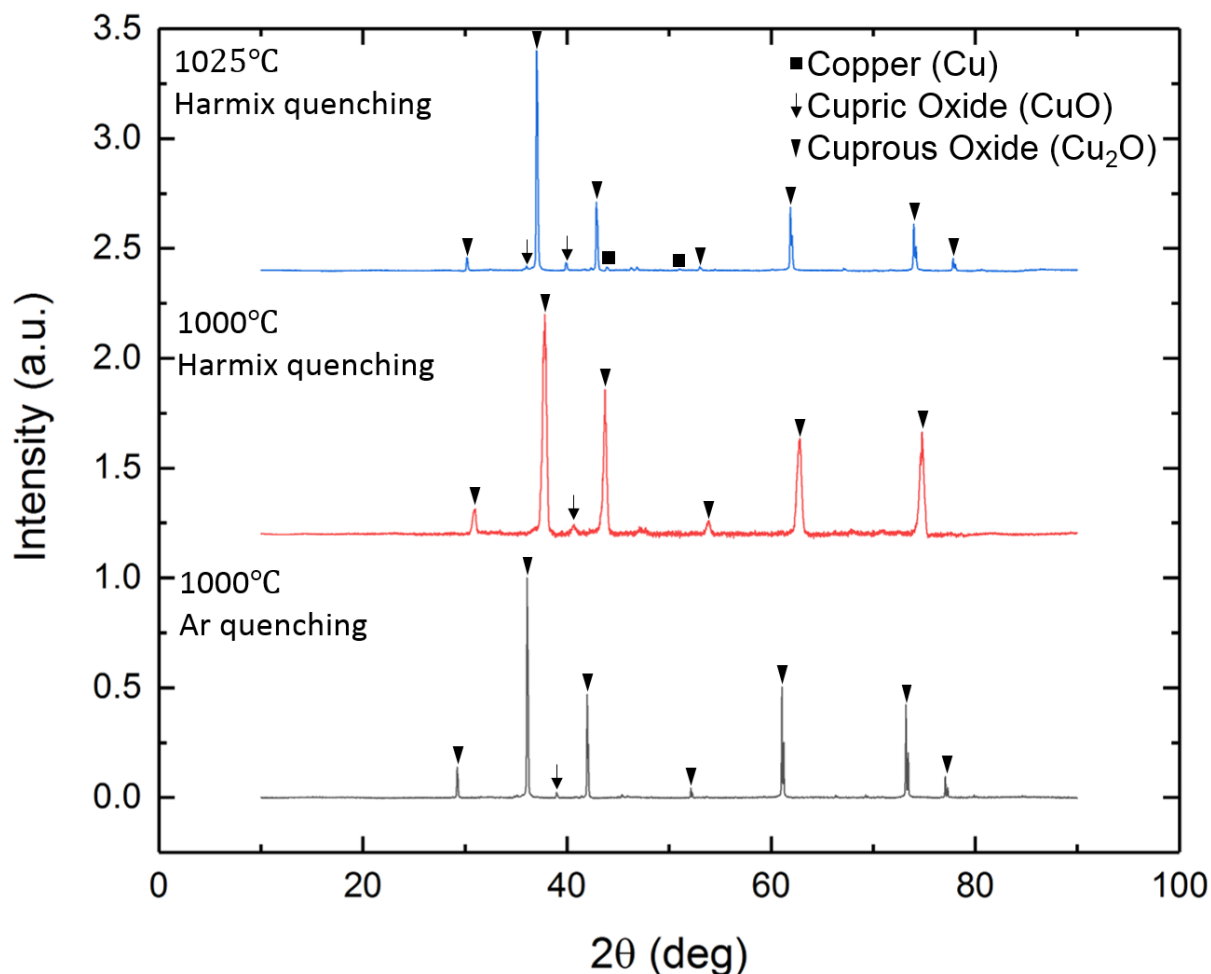
72

Figure 31: Three samples sintered at 1000°C, 1000°C, and 1025°C, respectively. The two of the samples were cooled by quenching them in Harmix, while one was quenched in Ar. All of the samples have peaks belonging to the Cu_2O phase, and the CuO phase. Additionally, the sample sintered at 1025°C and quenched in Harmix had Cu phase peaks. The samples correspond to Cu_2O 4a (black), Cu_2O 4b (red), and Cu_2O 5b (blue). Sample Cu_2O 4b was crumbled due to the experimental setup. Hence, the quality of the XRD is slightly worse than the others.

The three samples shown in Figure 31 have been sintered at 1000°C and 1025°C, respectively. The two samples sintered at the same temperature were quenched in different atmospheres. The difference in phases was that the sample sintered at 1025°C and quenched in Harmix showed an additional Cu phase. Moreover, the sample Cu_2O 4b (red) was crumbled due to the experimental setup. While the setup has been changed for other samples, the crumbled surface is visible in the XRD graph.

In Figure 32 the influence of flushing the Probostat with Harmix before heating is shown. While in the bottom plot (black) no Cu peak is visible, a sample in a ProboStat flushed with Harmix before sintering shows Cu_2O peaks. Reducing the sintering temperature to 1000°C reveals that the Cu peaks can be suppressed while the CuO peaks are minimal, too. Moreover, the Cu_2O peaks observed are well defined.
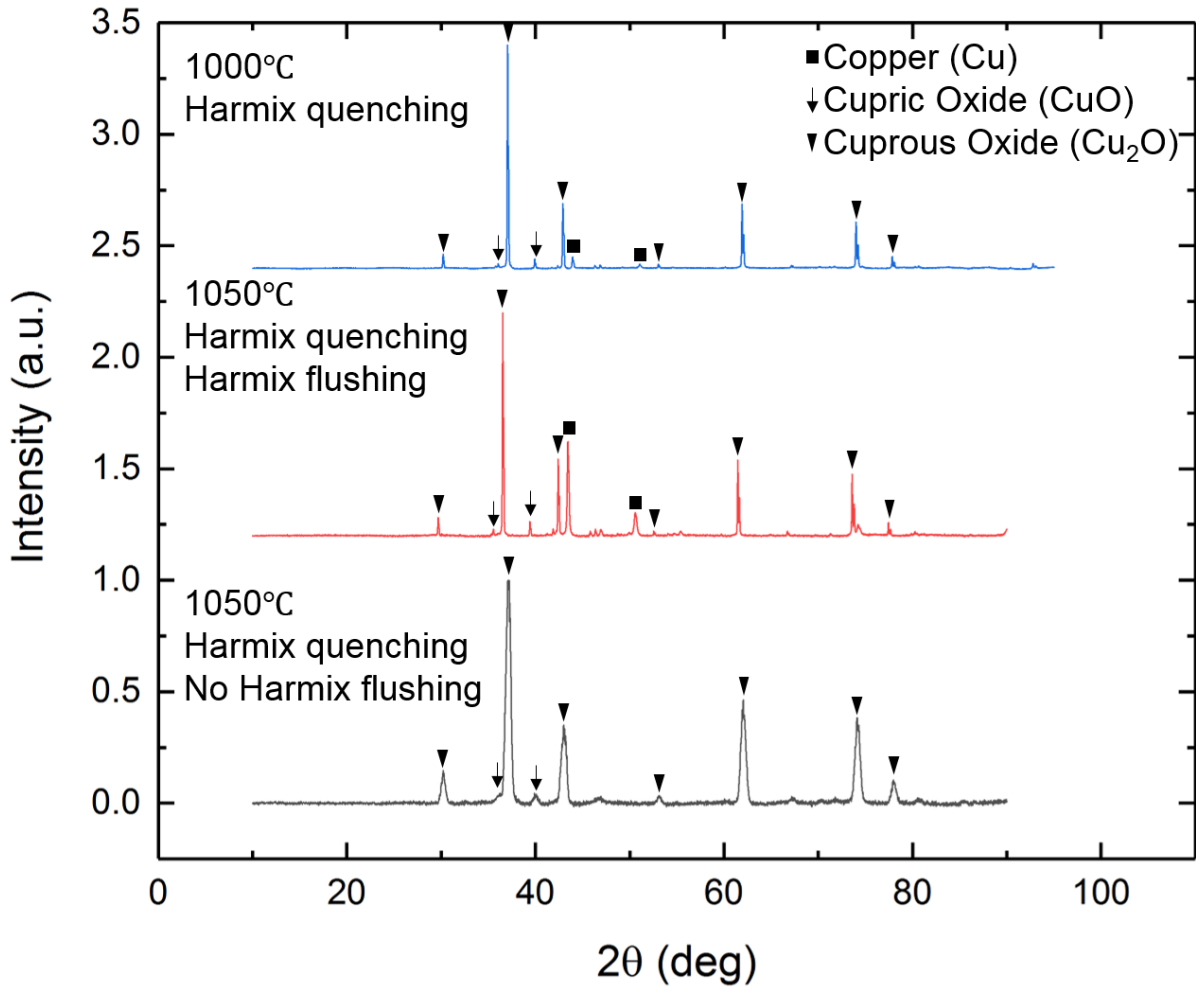
4. Results

Figure 32: The bottom two XRD graphs show the influence of Harmix flushing on the phases within the pellets. Without flushing, no Cu can be detected. With flushing significant Cu peaks are visible. Reducing the temperature to 1000℃ minimizes the Cu phase formed. The samples are Cu_2O 5b (black, and re-sintered red), and Cu_2O 6 (blue).

Finally, Figure 34 shows that despite high sintering carbon residues can survive in the bulk of the pellets. While the XRDs taken of the surface show the expected phases with Cu, CuO, Cu_2O, and ZnO, the crushed sample also showed carbon peaks at low 2θ angles. The SEM pictures were taken from different pellets. In Figure 33 (a) sample sintered at
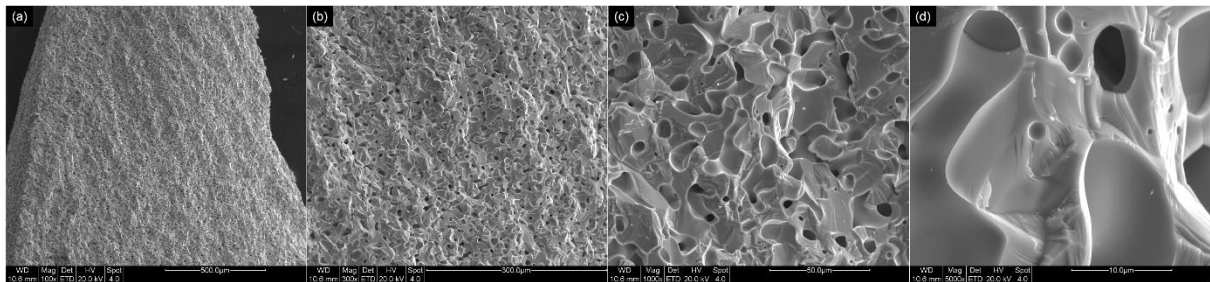

Figure 33: A SEM image of a sample sintered at 1050℃, and quenched in Ar + Harmix. The large pores within the sample are notable. (a) An Overview of the sample, wherein (b) and (c) the porosity can be seen. In (d) a close-up of one pore is shown, revealing the size of a few micrometers.

74

1050℃ is shown, revealing a porous sample with pores of a few micrometers diameter. The other sample sintered at 1050℃ (Cu_2O 10b) was also observed by SEM. Two large bright regions were discovered and displayed in Figure 35. While the sample still appeared to be porous, it seemed to be less so than the sample observed in Figure 33. The bright regions are located within the bulk.

The structural differences occur mainly on the surface of the pellet. These differences were taken into account to create the targets. To have a sequence of pellets made, Table 13 shows the order and the changes in the experimental setup. The pellets used in the PLD experiments are labeled. Moreover, it is evident that the bulk of all the samples is Cu_2O and only a thin cover layer of the surface has a different structure.
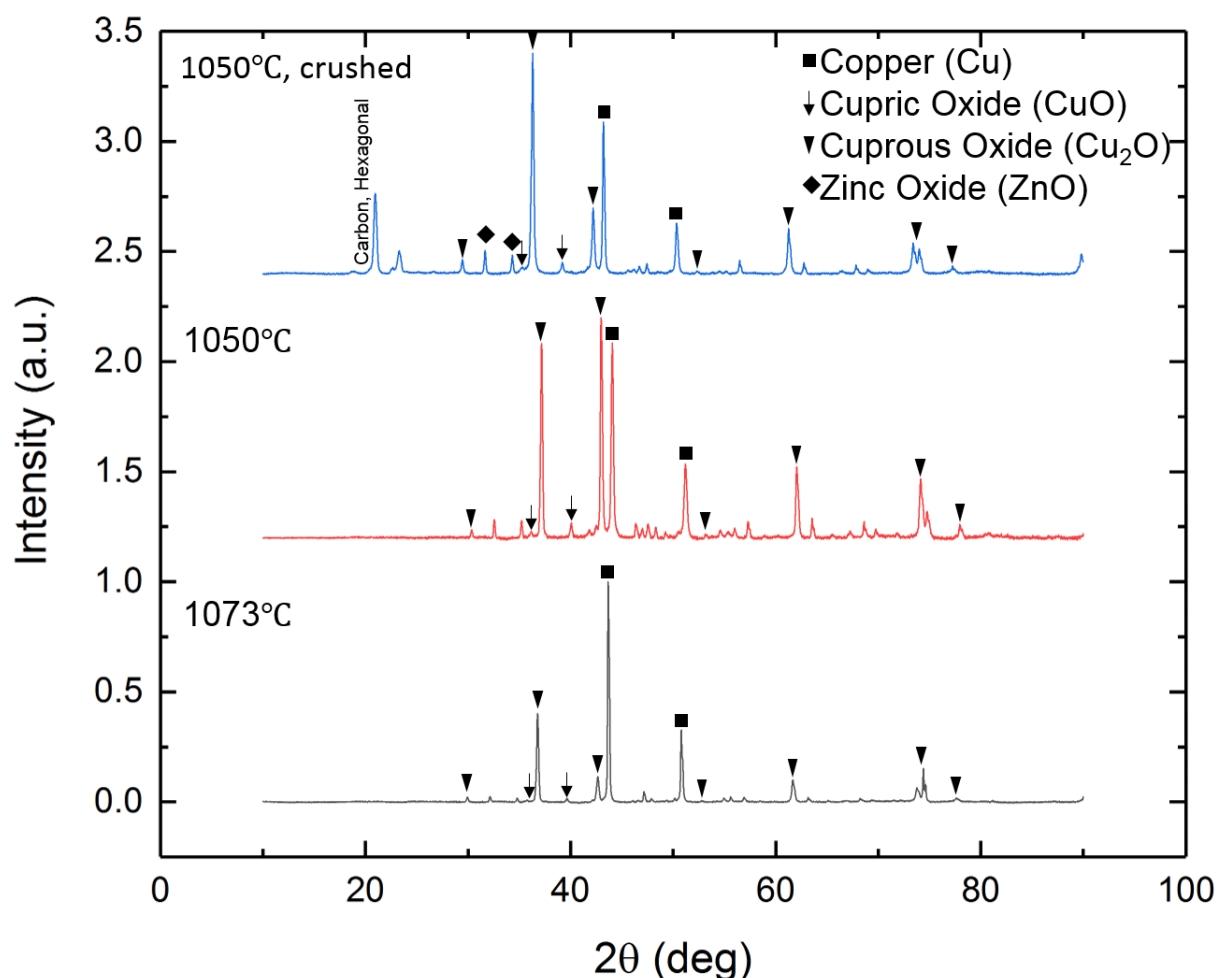

Figure 34: Two different samples, where one was sintered at 1073℃ and the other at 1050℃. The second sample has been crushed to reveal the bulk properties, displayed in blue. Both samples show Cu, CuO, Cu_2O, and ZnO. The crushed sample reveals additionally significant peaks at low 2θ. The peaks have been attributed to organic residues within the sintered sample.

4. Results

Table 13: The summary of the pellet sintering with the sintering order, and the change in the experimental setup.

| #:	Pellet:	Change:
1	Cu$_2$O 4a	Pellet Size
2	Cu$_2$O 4b	Setup, Sintering T
3	Cu$_2$O 5a	Harmix Flushing, Sintering T
4	Cu$_2$O 5b	Sintering T
5	Cu$_2$O 6	Sintering T
7	Cu$_2$O 3	Sintering T
8	Cu$_2$O 10a	Sintering T
9	Cu$_2$O 10b	Sintering T
10	Cu$_2$O 5b	(Re-sintering the sample 5b), Sintering T
11	Cu$_2$O 1	
All others: Made with the setup used for sample Cu$_2$O 1, conditions as stated, fast XRD to check for differences, mainly used as target in the PLD.		
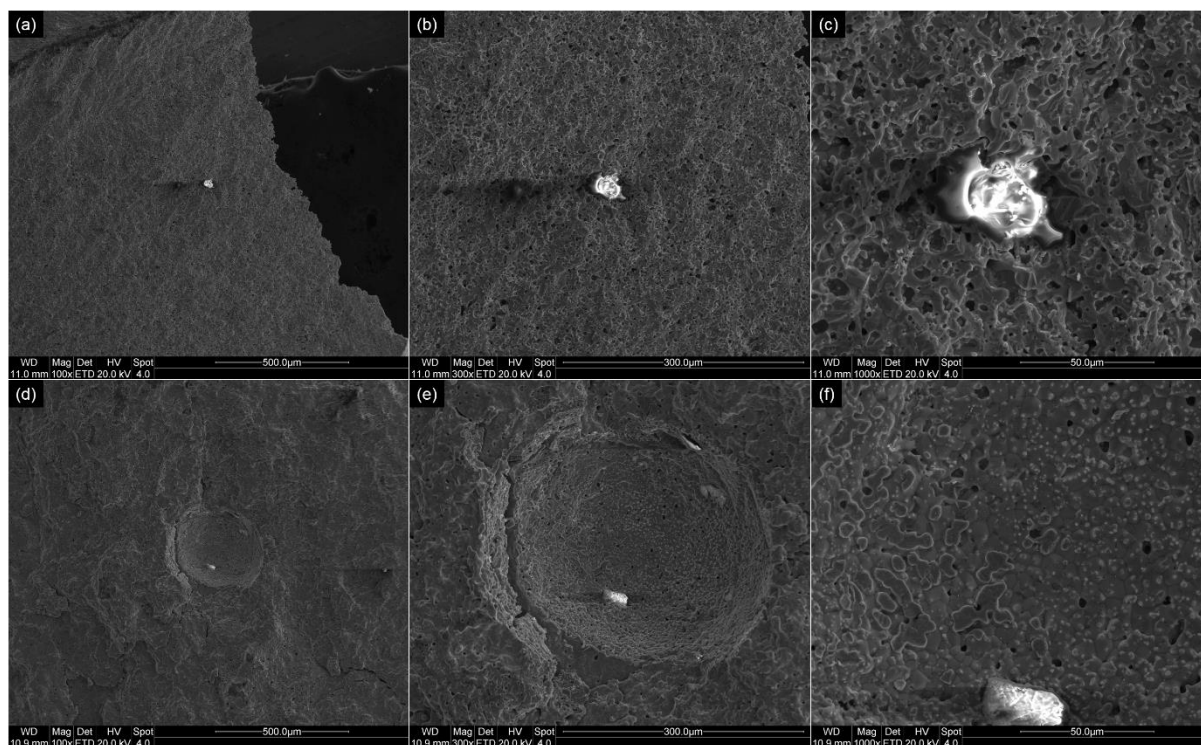
Figure 35: SEM images of the bulk of the sample sintered at 1050℃ and whose XRD is shown in Figure 34. The images are taken after cracking the pellet and reveal two bright regions embedded within the sample. The first bright region is roughly 25 μm in diameter ((a) – (c)). The second bright region is less round but elongated with a width of 25 μm and a height of 10 μm ((d) – (f)).

4.3. Thin Film (S)TEM Results

Table 14: The TEM samples presented below, with the thin films obtained, and pellets used to manufacture them.

Sample Number:	Thin Films:	Pellets Used:
1	ZnO	ZnO 3
2	Cu_2O/ZnO	Cu_2O 3b, ZnO 4

The PLD grown thin films (section 3.1.3) were further studied by (S)TEM methods and the results were used to optimize the deposition conditions of the films, at 200 kV acceleration voltage. The samples presented, as well as their number and pellets used are shown in Table 14. The first sample observed was a thin film of ZnO on Si (TEM sample 1). Figure 36 (a) and (b) illustrate HAADF-STEM and bright-field TEM images, respectively. A 200 nm thick ZnO thin film was grown on the Si substrate, exhibiting a columnar structure. The glue on top of the ZnO layers indicates that the sample is intact, and no copper phase was observed. The diffraction pattern (Figure 36 (c)) shows the heteroepitaxial relationship between the two films of high crystal-quality, without amorphous regions. Figure 36 (d) shows a HRTEM image revealing a sharp Si/ZnO interface.

A second sample (TEM sample 2) was also studied by (S)TEM. Figure 37 (a) illustrates a HAADF-STEM image and (b) the corresponding EDS map, where a copper-rich film of roughly 135 nm thickness was identified followed by the growth of a zinc-rich film of up to 550 nm thickness.

Figure 37 (c) shows the diffraction pattern of the heterostructure. The rings suggest multiple small domains of the observed phases (poly-crystallinity), in this case Cu_2O and ZnO, along with the single-domain Si substrate. Furthermore, CuO (001) has been identified.

In Figure 38 (a) another EDS map is shown, closer to the interface. In (b) – (d) the individual elemental maps are shown. Not a clear difference in the Cu and O signals in the area where CuO/Cu_2O is expected is observed. However, more detailed work at the interfacial area is still pending.
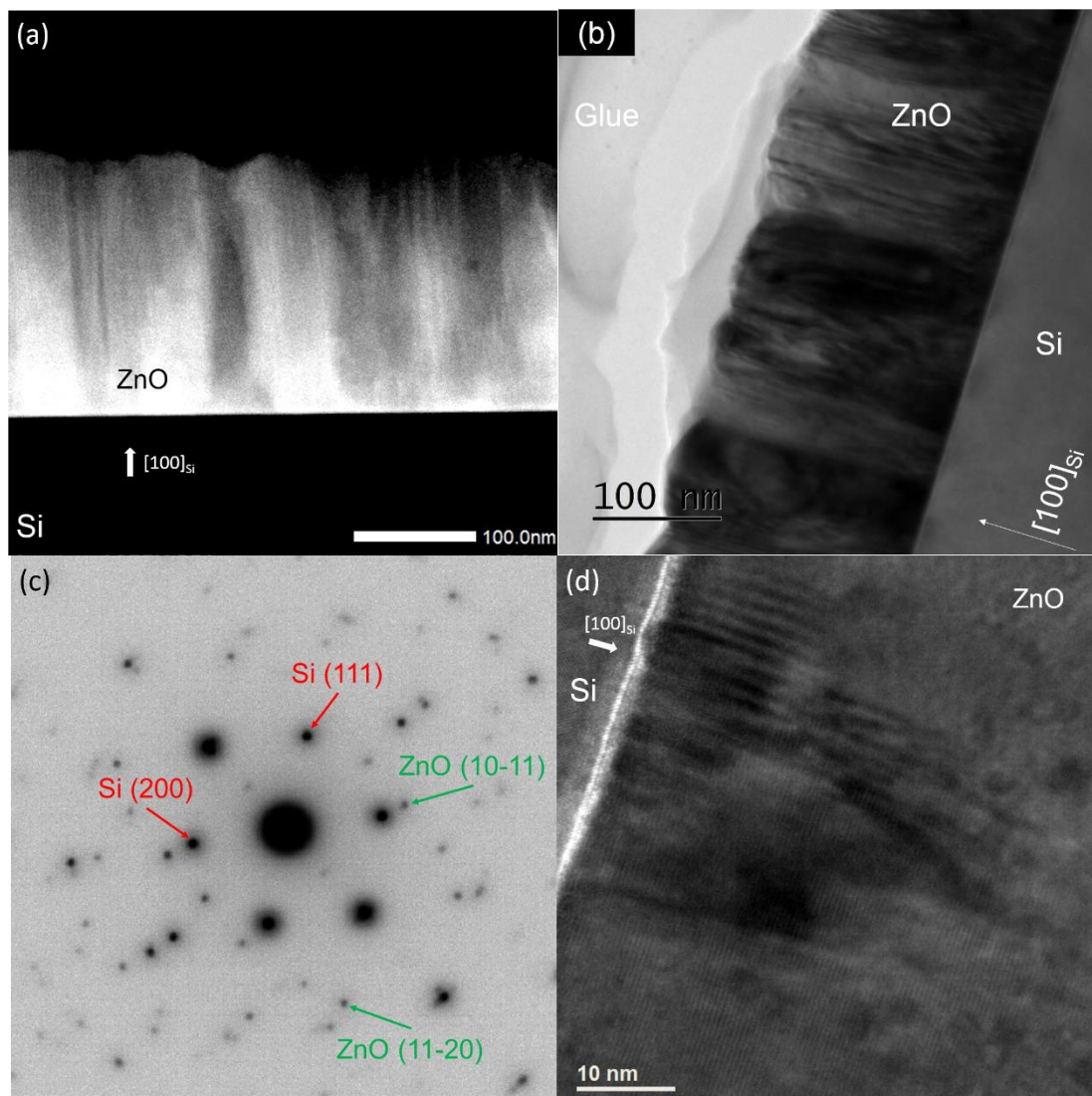
Figure 36: The ZnO thin film grown by PLD on Si. (a) and (b): HAADF-STEM and TEM images revealing the overall morphology of the structures, were a ZnO thin film of columnar growth is illustrated. (c) SAED pattern showing the ZnO/Si heteroepitaxial relationship. No indication of a Cu-phase was observed. (d) HRTEM image showing the sharp ZnO/Si interface.
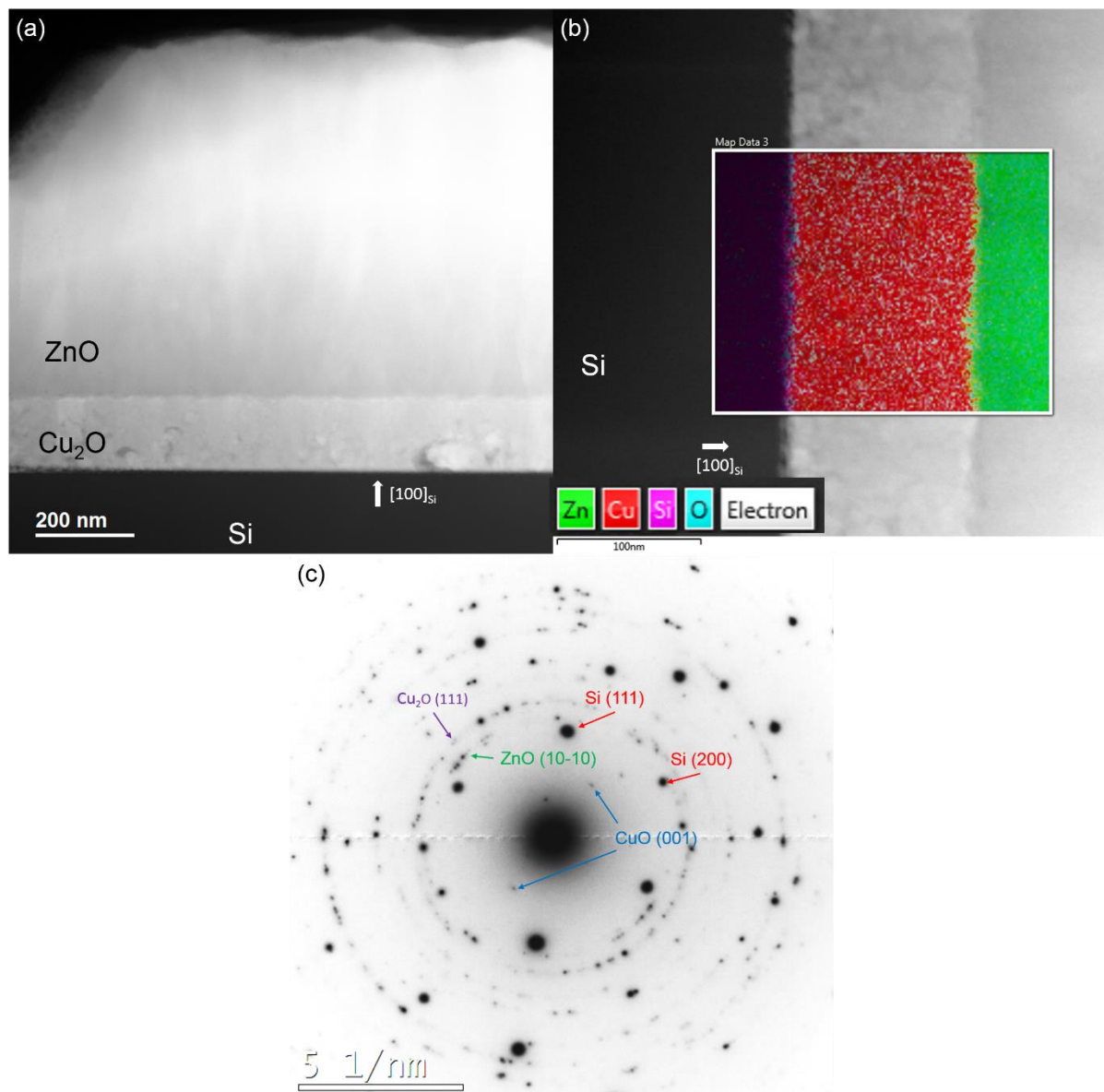
Figure 37: (a) and (b): HAADF-STEM image and the corresponding EDS map. The growth of the Cu-phase film of ~135 nm thickness is illustrated, followed by a Zn-phase film of ~550 nm thickness. (c): SAED pattern showing Cu_2O and ZnO polycrystalline films, as well as a single domain Si, and CuO.

Figure 38: EDS map of the interfacial area. (a) shows an overlay of the elemental map and a HAADF image, and (b) – (d) the maps for Cu, Zn, and O, respectively. Not a clear difference is detectable in the area where CuO/Cu_2O is expected. However, more detailed and systematic work is still pending.
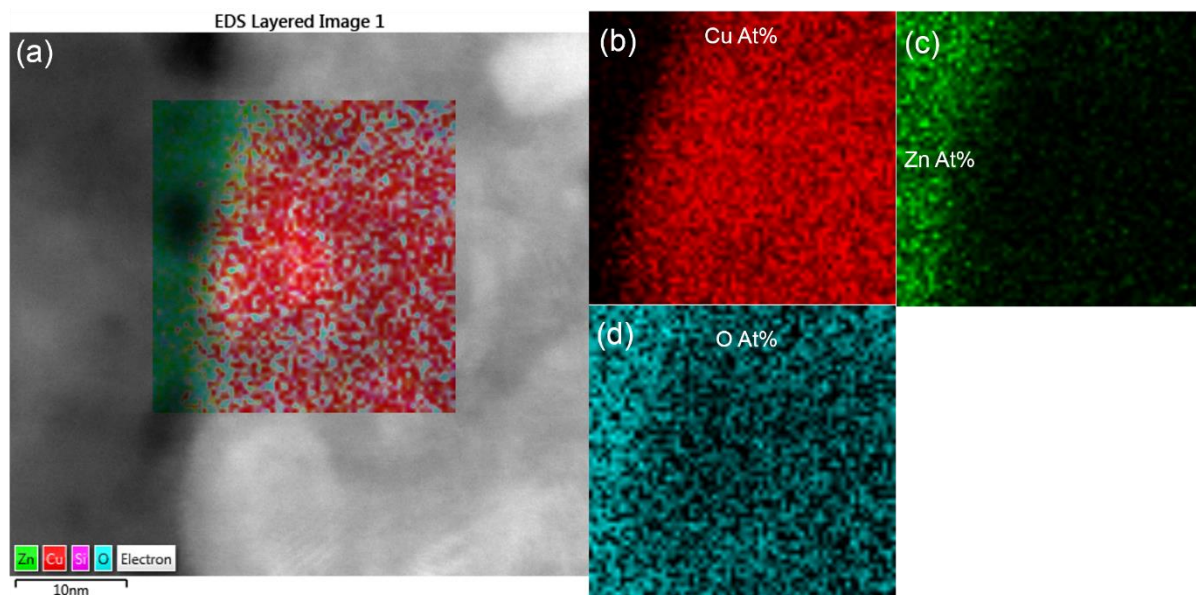
4.4. Computational Results

The energies of selected interfaces were calculated, and the resulting interface energies of the different lateral shifts plotted in contour plots (Figure 39 to Figure 43). Moreover, for every interface, the electron density was used to determine the most stable interface. The density of states (DOS) is shown in Figure 44 for two interface. While the main focus of the calculations was to determine the most likely structure formed, these additional plots can be used to explain the energies and show the limitations of the calculations; for example, the band gap calculation or degeneracy of the interface energy. Table 15 shows the energy per atom for the most stable interface shift for the respective interface.

Table 15: The interfaces and the energy of the most stable structure calculated. The CuO interfaces are more stable than interfaces without CuO.

Interface:	Energy $\Delta_f E_{int}$ (eV/Atom):
Cu_2O (111) – ZnO (0001)	- 0.054
Cu_2O (110) – ZnO (0001)	- 0.055
CuO (100) – Cu_2O (111)	- 0.123
CuO (100) – Cu_2O (110)	- 0.058
CuO (100) – ZnO (0001)	- 0.110
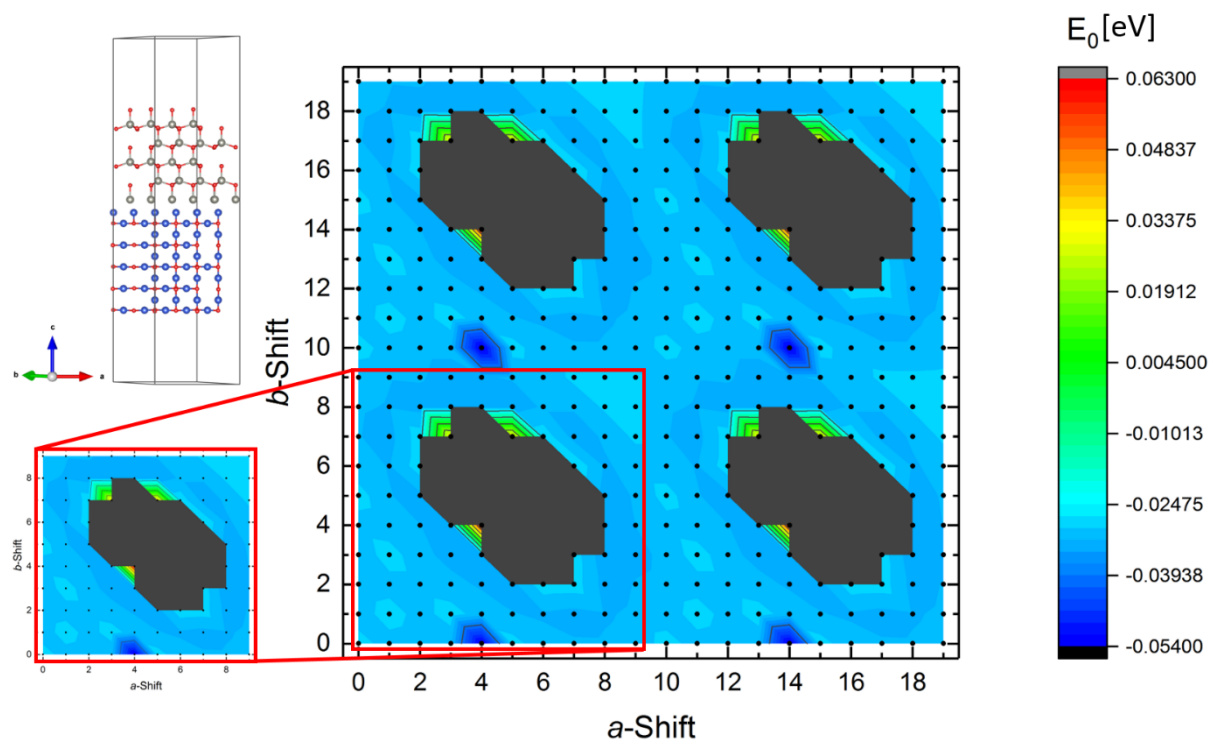
Figure 39: The energies per atom gained by forming the Cu_2O (111) – ZnO (0001) interface versus $a − b$ displacement. The red box shows the quarter of the unit cell that has been calculated. The structures of the other three-quarters of the plot are identical with the calculated structures. The grey areas indicate structures where the ionic relaxation did not converge.
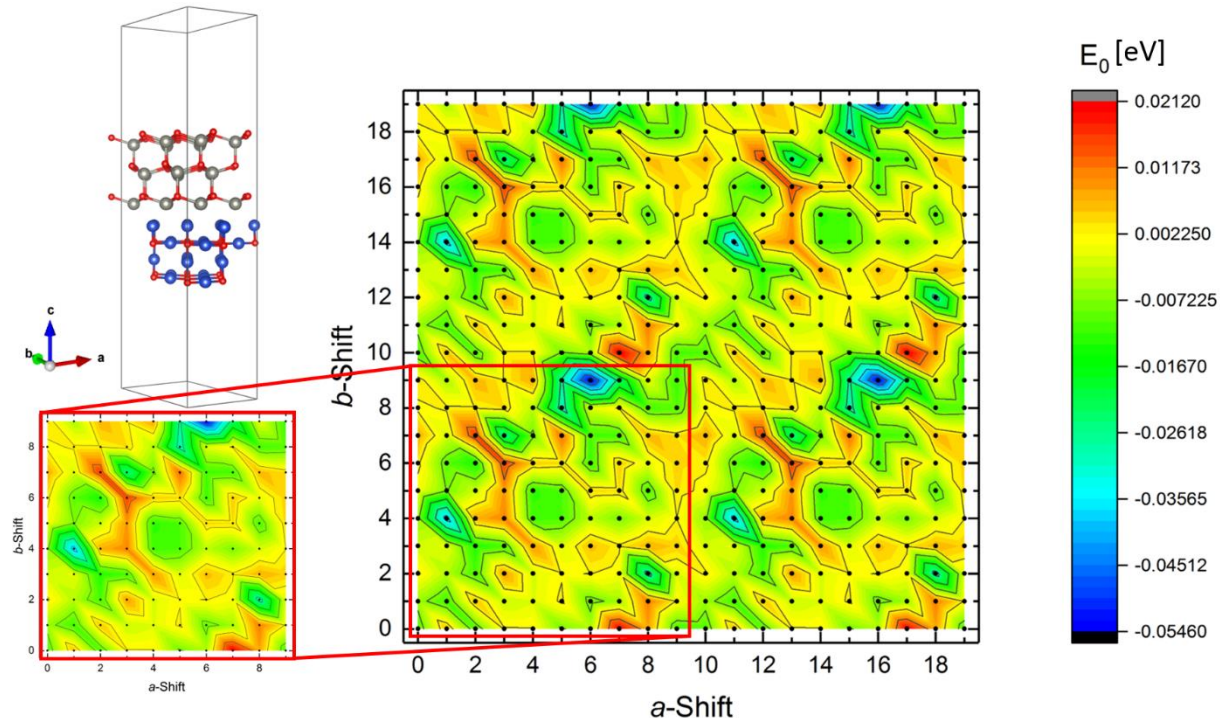

Figure 40: The energies gained by forming the Cu_2O (110) – ZnO (0001) interface for each starting structure. The configuration with the minimum energy is easily observable. Moreover, it is noticeable that a substantial part of the configurations is unfavorable to form.

4. Results

The interface energies will be evaluated according to their energy gain by forming the interface compare to two slabs in vacuum. In order to compare these interfaces and the energies, the results will be shown in eV per atoms for all structures. The equation to determine the energy is

$$\Delta_f E_{int} = \frac{1}{N}(E_{Interface} - E_{Slab}) \tag{78}$$

where N is the number of atoms, $E_{Interface}$ the energy of the interface, E_{Slab} the energy of the slab and $\Delta_f E_{int}$ the energy difference in forming the interface per atom.

The energies of the $Cu_2O(111) - ZnO(0001)$ interface have been calculated and are shown in Figure 39 as a function of the displacement of one slab. The structure most relaxed is the structure with a shift of 4 in *a* direction and 0 in *b* direction. In Cartesian coordinates, this means that the ZnO is shifted 1.25Å in the x-direction. The resulting structure has an energy gain in forming the interface of -4.532 eV or -0.054 eV per atom (84 atoms in total, 24 Cu atoms, 36 O atoms, 24 Zn atoms). No other structure has an energy closer than 0.02 eV per atom. The grey area indicates structures that did not relax properly.

The second interface, $Cu_2O(110) - ZnO(0001)$, has different energies shown in Figure 40. The shift for the most stable interface is 6 in *a* direction and 9 in *b* direction, corresponding to a shift of the ZnO of -2.085Å in x-direction and 4.887Å in the y-direction in a Cartesian coordinate system. The energy gained by forming the interface is -4.529 eV or -0.055 eV per atom (83 atoms in total, 23 Cu atoms, 36 O atoms, 24 Zn atoms). The closest energy of any other surface is 0.016 eV per atom higher.

The last interface containing ZnO is the $CuO(100) - ZnO(0001)$ interface, by far the most stable interface containing ZnO. The shift of the most stable interface is 0 in *a* direction and 5 in *b* direction. This corresponds to a shift of 1.670Å in x-direction and 1.346Å in the y-direction in a Cartesian coordinate system. The energy of said shift is -10.601 eV or -0.110 eV per atom (96 atoms in total, 24 Cu atoms, 48 O atoms, 24 Zn atoms). As is visible in Figure 41, a considerable amount of structures ended up having similar energies, where the closes one is -0.000(2) eV per atom higher than the minimum energy.

The energies of the interface $CuO(100) - Cu_2O(111)$ are shown in Figure 42. The grey area corresponds again to structures not relaxing correctly. The most stable interface was achieved with a shift of 5 in *a* direction and 9 in *b* direction, corresponding to 2.505Å in x-direction and 2.901Å in the y-direction. The energy of the formation of that junction is -12.572 eV or -0.123 eV per atom (102 atoms in total, 64 Cu atoms, 38 O atoms). The closest energy of another shift is 0.001 eV per atom higher.

Finally, the energies of the last interface, CuO (100) – Cu₂O (110) versus their shift in *a* and *b* direction are shown in Figure 43. The most stable interface is formed when shifting the Cu₂O by 9 in *a* direction and 0 in *b* direction, corresponding to a shift of 4.664Å in the x-direction. The energy gained in forming the most stable interface is − 9.686 eV or − 0.058 eV per atom (166 atoms in total, 98 Cu atoms, 68 O atoms). The second lowest energy is 0.000(3) eV per atom higher than this interface.

The calculations represent the interfaces at zero Kelvin and in vacuum. The two most stable interfaces according to these calculations are the CuO (100) – Cu₂O (111) and CuO (100) – ZnO (0001) interface. Unsurprisingly, these interfaces have been reported, as previously indicated. Moreover, these results are evidence that the cupric oxide interlayer is unlikely to disappear without changing any of the conditions substantially, as both of these interfaces gain double as much energy per atom as the formation of any other interface calculated.

The DOS of the interfaces reveals another side of these calculations. As is evident in the plots shown in Figure 44, none of the interfaces show a band gap. This can originate from the choice of exchange-correlation functional. As is stated above, the PBE functional underestimates the band gap of ZnO, Cu₂O, and CuO. As a consequence, the band gap representation can be underestimated, to the extent, where no band gap is shown.
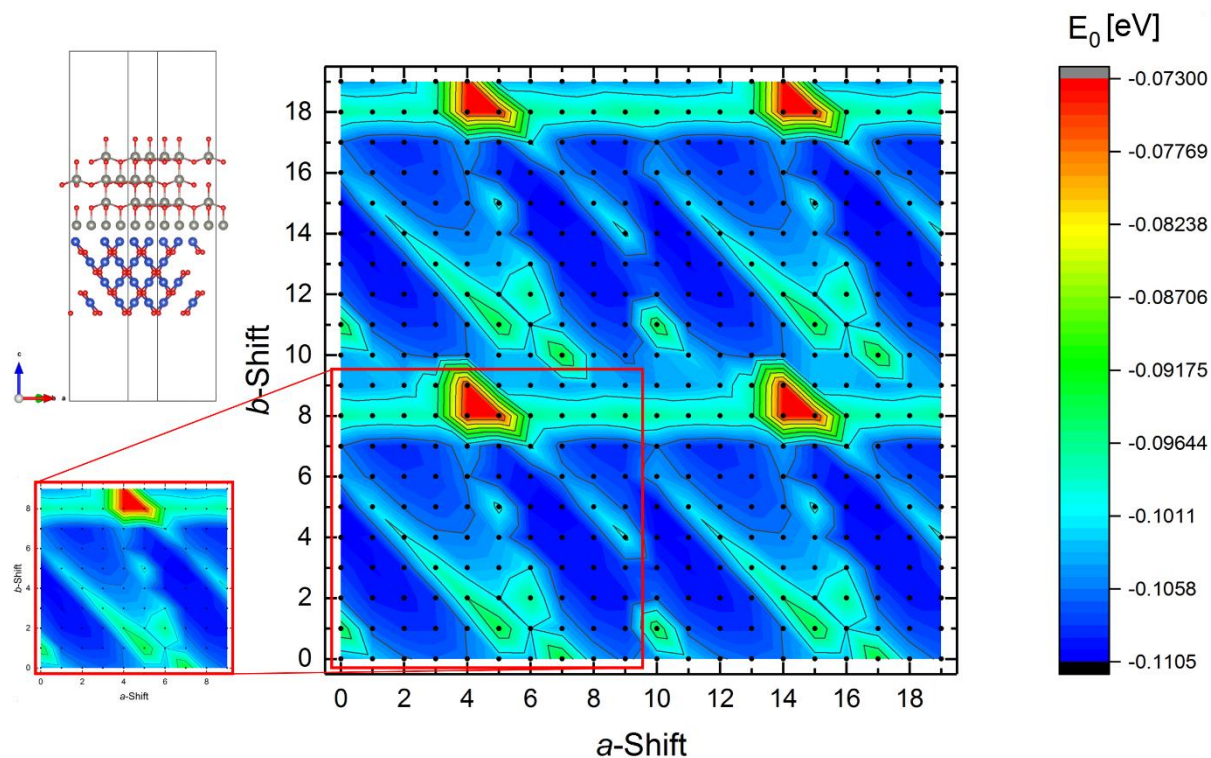
Figure 41: The energies per atom gained by forming the CuO (100) – ZnO (0001) interface for each starting structure. It is not easily distinguishable which is the most stable structure due to the majority of the structures being similarly stable.

4. Results
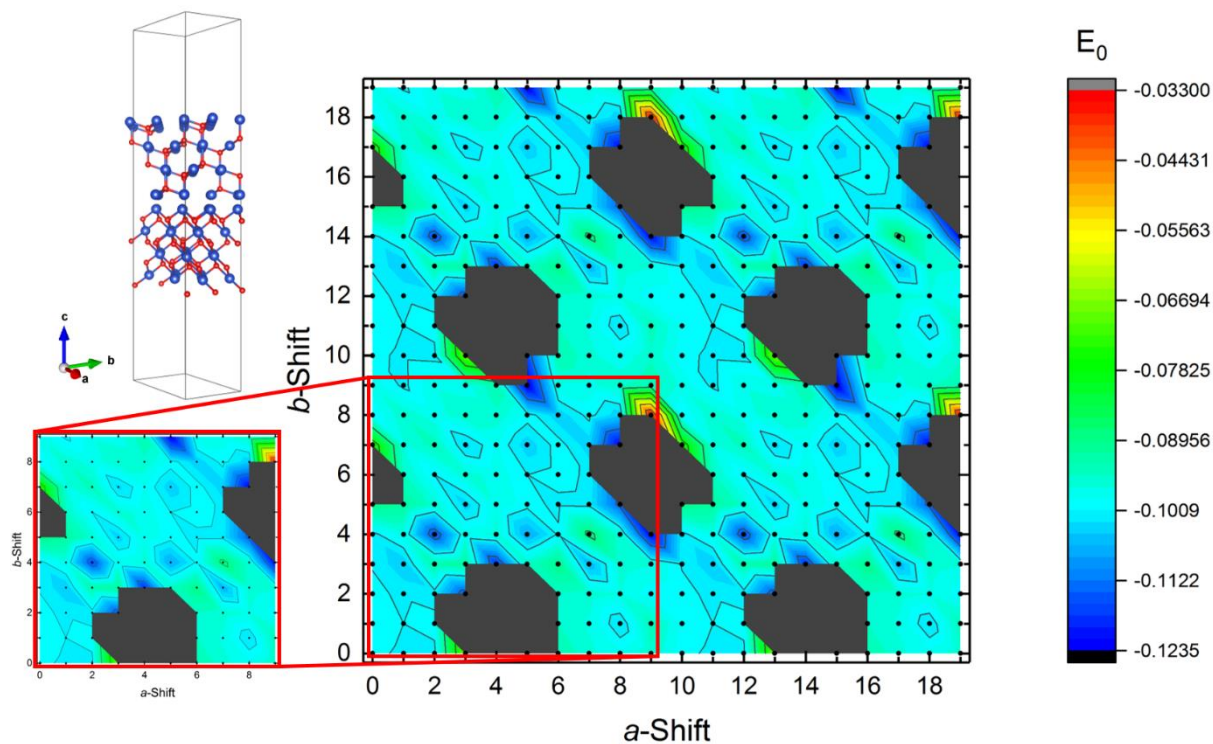
Figure 42: The energies per atom gained by forming the CuO (100) – Cu$_2$O (111) interface as a function of the *a-b* shift. The grey area marks regions that did not converge during relaxation. The majority of the structures has a similar energy per atom pointing toward a formation of the junction. However, there are a couple with considerable lower energies.
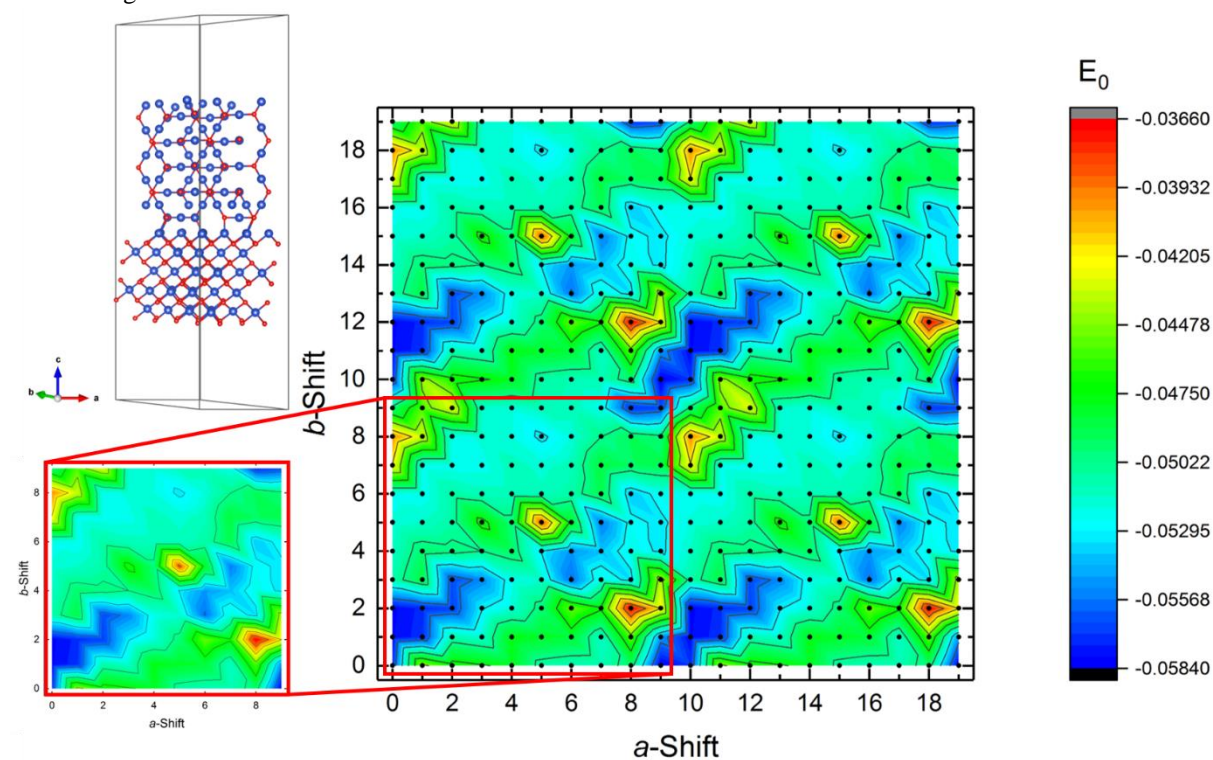

Figure 43: The energies per atom gained by forming the CuO (100) – Cu$_2$O (110) interface versus the *a-b* shift. The region with the most stable configuration is visible, and several structures have similarly low energy.
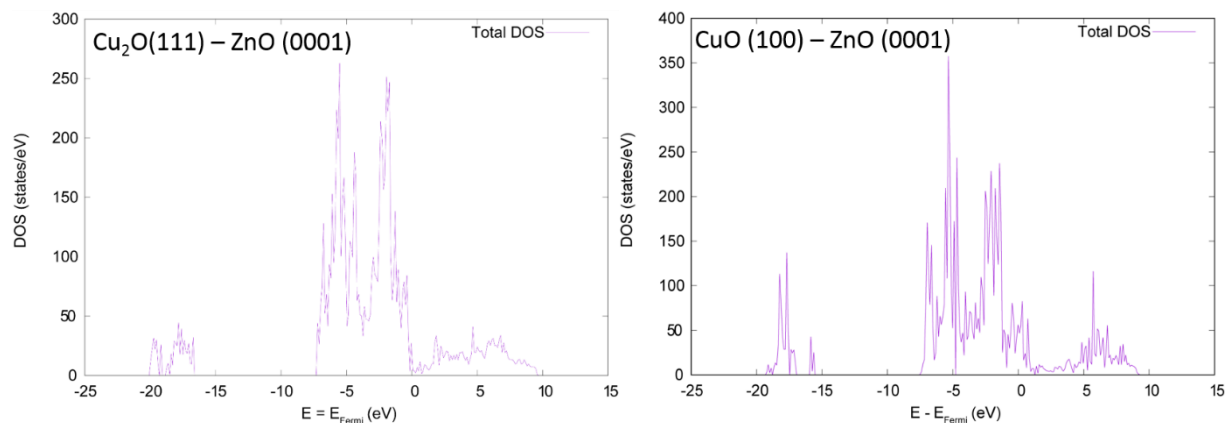
Figure 44: The density of states of two interfaces. As is visible in the plots, there is no band gap around the Fermi level. However, this can originate in the exchange-correlation used during the calculations as discussed above.

The electron density can be used to see the influence of the junction on the electron structure. While there are certainly better exchange-correlation functional to calculate the DOS and electron density, a first indication can be provided by PBE.

The radial distribution function of the distance between the cations and anions in an interface can be used as a measure of disturbance introduced by it. This is shown in Figure 45, where in (a) the radial distribution function for the bulk oxides is given, and in (b) – (d) for the respective interfaces and cations. Naturally, the anions are found on both sides of the interface, introducing a combination of both oxides to the graph. However, the resulting plots are not just an addition of two bulk radial distribution function with a shift, but rather a broadening of peaks, beginning with the highest, initial peak. For the most stable interface, CuO (100) – Cu_2O (111), the initial peak is the dominant, followed by no clear other peak. This is in contrast to all the other graphs, where distinct broad peaks are visible. The plots show the influence of the interface on the structure.

The calculations and their results displayed above show various properties of the interface. First, and foremost, the most stable interface for each interface, and of all five interfaces has been determined as the CuO (100) – Cu_2O (111) interface, followed by the CuO (100) – ZnO (0001) interface. It cannot be coincident that this exact order of phases, Cu_2O (111) – CuO (100) – ZnO (0001), has been observed, and its phases are the most reported observed phases of the system at hand. Moreover, the DOS fails to show any band gaps. The radial distribution function show a broadening of the found cation – anion distances.

85

4. Results
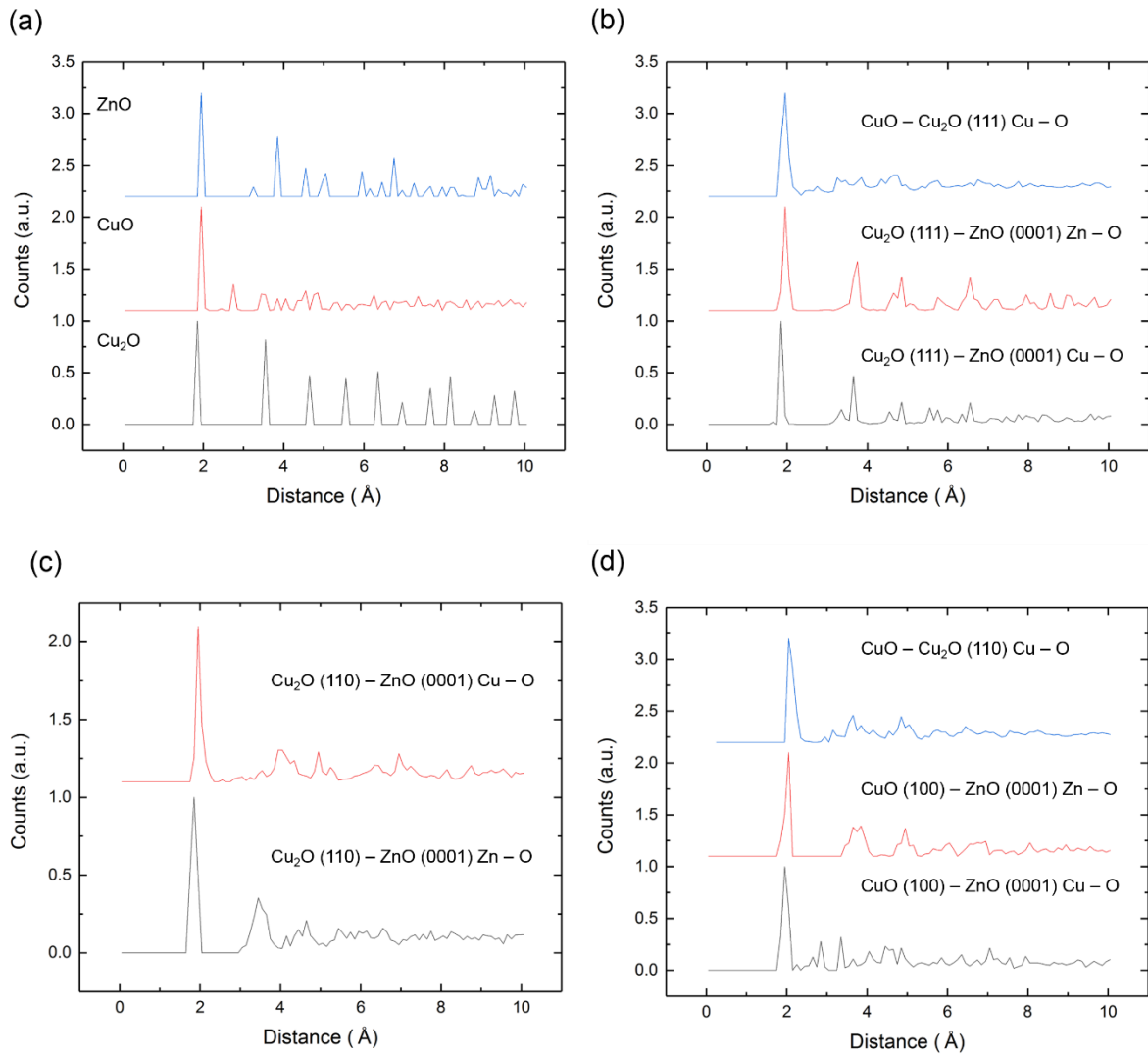
Figure 45: The radial distribution function of the cation – anion distance. In (a) the three bulk oxides. The largest peak is in good agreement with the cation – anion distances reported in [28] and [190]. In (b) – (d) the effect of the respective junction can be seen, where the cation – anion combination behind the interface states the distance examined in the particular plot. In general, it can be said that the peaks appear broader in the interface structures than in the bulk oxides.

5. Discussion

In this chapter, the conditions for the successful formation of Cu2O and ZnO in different forms are summarized. To support the conclusions and statements made, the results shown above will be used as examples. Additionally, the experimental and theoretical results are connected to support these conditions.

5.1. Conditions for the Formation of ZnO

ZnO is readily available as a powder and is thermodynamically stable. Moreover, as is evident from the 5 ZnO pellet samples created, manufacturing ZnO pellets is straightforward by pressing pellets and sintering them at 1400℃ in ambient atmosphere. Sacrificial powder has to be used to prevent evaporation of parts of the ZnO pellet. The formation of a thin film by PLD is achieved by using 190 mJ cm^{-2}. The thickness, number of shots, and energy used are specific to the experimental setup. This is evident that both the $\sim$200 nm and $\sim$550 nm thick ZnO layer were deposited with the same number of shots and energy per shot. However, the height and state of the instrument were changed (height varies 7 cm and 5 cm, respectively, and the lenses were cleaned before the second sample, lenses were repositioned).

Besides the change in thickness, there are two main differences in the samples presented. It has been reported that the conversion efficiency of the p-n-junction is higher for growing in the order of $Si - ZnO - Cu_2O$ than samples grown in the order $Si - Cu_2O - ZnO$, as stated above and in [24]). The structural differences between the two samples manufactured and observed in this work, despite the absence of Cu_2O in one of them, is the size of the domains in ZnO. While both are multi-crystalline, ZnO grown on Si shows much larger domains than ZnO grown on Cu_2O. The difference in domain size can explain why the conversion efficiency is higher.

5.2. Conditions for the Formation of Cu$_2$O

Cuprous oxide is commercially available as a powder. However, powders created by the sol-gel method ultimately lead to the same pellet structure, and the formation can be studied. Creating a sol-gel powder sample lead to evidence of two different behaviors. One above 350℃, upholding the thermodynamic predictions, meaning that CuO and Cu_2O are formed as predicted by the plot in Figure 18, shown by the three samples calcined at high temperature. The other behavior occurs below 350℃, and cannot be predicted by the thermodynamic graph. The formation of CuO, Cu_2O, and Cu is possible and influenced by more factors than the

combination of oxygen partial pressure and temperature. This is evident in the variety of phases obtained in the seven low-temperature samples. An example for the influence of other factors on the sample is the formation of just CuO with high initial ethylene-glycol content and formation of all three copper phases in a sample with less ethylene glycol but otherwise unchanged manufacturing conditions.

The 20 Cu_2O pellets manufactured were all heated to temperatures above 350℃. As has been demonstrated above, the phase can be obtained by adjusting the oxygen partial and temperature in the system. Hence, samples can be sintered at higher temperatures in Ar, and medium temperatures in Harmix to obtain a pellet with a cuprous oxide bulk. The cooling atmosphere and duration define the surface of the pellet, and both CuO and Cu coverages were obtained.

The thin film deposition of Cu_2O was highly dependent on the instrument, resulting in only two observed depositions with a plume. Moreover, the thin film is very polycrystalline, as shown above. The poly-crystallinity prevents the recording of a clear HRTEM image of the copper phase, but the SAED pattern shows the presence of CuO.

5.3. Connection between Theoretical Studies and Experiments

Understanding the principles of heterojunction, with the specific band alignment the Cu_2O – ZnO junction has, explains why cuprous oxide has the greatest potential for solar cell applications. The bandgap of Cu_2O is almost ideal for a tandem solar cell, and the band alignment with ZnO promotes the use of it in a solar cell setup. The DFT calculations predicted that the CuO (100) phase is more stable on Cu_2O (both (110) and (111)) and ZnO (0001) than any other interface of interest these orientations can obtain. This suggests the formation of CuO independent of growing order and orientation. The TEM SAED pattern shows evidence of the layer present at the interface. The copper phase in any experiment conducted in this work forms CuO if the oxygen partial pressure and temperature allows its formation. Additionally, the water vapor present in the system provides oxygen. Both ZnO and Cu_2O have intrinsic defects promoting the migration of oxygen from the ZnO to the Cu_2O. This would suggest a gradient in oxygen around the interface, where elevated numbers of $v_O^{\cdot\cdot}$ are found in ZnO, and the additional oxygen in Cu_2O leads to the formation of CuO. The theoretical studies and experimental observations conducted in this study do not suggest the origin of the additional

oxygen needed to form the CuO phase. Nonetheless, they all show the tendency of the system towards CuO, as is predicted by thermodynamics.

5. Discussion

6. Conclusion

A CuO interlayer was obtained at the interface of a Cu$_2$O-ZnO p-n-junction manufactured utilizing the PLD technique, with Cu$_2$O and ZnO targets, in an argon atmosphere at low temperature (300℃). Moreover, the Si/Cu$_2$O/ZnO sample shows polycrystalline films, whereas ZnO grown on Si leads to a with non-polycrystalline columnar growth. The differences in structure explain why a higher conversion efficiency has been reported for samples with Cu$_2$O grown on ZnO than in the reverse order. Furthermore, the interlayer will form independently of the growing order because of the stability of CuO on ZnO and Cu$_2$O.

Studying the set of interfaces with DFT yielded an accurate prediction of which interfaces will form. The PBE functional underestimates the band gap tremendously, and the Tasker type 3 interfaces influence these calculations, too. To study the most stable interfaces in-depth the choice of functional has to be adjusted to a more advanced functional predicting the right band gap, and the influence of the type 3 interface on the calculations has to be studied.

The formation behavior of copper and its oxides were established. The high-temperature region (>350℃) forms phases defined by thermodynamic equilibrium with temperature and oxygen partial pressure. The low-temperature region (<350℃), however, forms phases defined by kinetics and other factors, such as presence of ethylene glycol. Hence, the formation of CuO or Cu$_2$O is more predictable in the high-temperature range and easier to manipulate. Argon and hydrogen mixtures, in combination with temperature, can be utilized to form the desired Cu$_2$O phase controllably.

In the high-temperature region, the composition of the junction will depend on the thermodynamics. The ZnO layer through its induced change in oxygen partial pressure has considerable influence on the Cu$_2$O at low temperatures. Moreover, much like ethylene glycol, it can be assumed that the ZnO layer in the low-temperature region influences the copper oxide such that CuO is formed.

The influence of defect chemistry on the junction has not been studied. The intrinsic defects reported in literature and discussed above show that oxygen vacancies are present in ZnO, and oxygen interstitials in Cu$_2$O. These two behaviors can promote each other, and lead to a more oxygen-depleted area at the interface in ZnO, and the formation of a CuO phase on the copper oxide side of the interface. However, further studies into the validity of this new hypothesis have to be conducted.

6. Conclusion

All these findings hint on an issue with the operation of the p-n-junction. Assuming a successful formation without CuO interlayer is achieved, the p-n-junction cannot be utilized in a temperature range of ~300℃ to ~1000℃ even in an argon atmosphere, without introducing the CuO interlayer. Unlike the interdiffusion of dopants in Si p-n-junctions at elevated temperatures, the Cu_2O layer does not intermix with the ZnO, but it oxidizes to CuO with elevated temperature and suitable oxygen partial pressure. This process presumably starts at the interface, with the formation of the CuO interlayer that has been observed. Hence, the Cu_2O – ZnO p-n-junction is unstable under certain, common combinations of temperature and oxygen partial pressure. This predicted inherent behavior of the CuO free Cu_2O – ZnO p-n-junctions imposes constraints of the usage of the p-n-junction. Either the devices can only be used in specific temperature ranges, or other ways to ensure the stability, such as oxygen partial pressure regulation during operation have to be established.

The dominant phase, cupric oxide, could be utilized in p-n-junctions. It has a band gap similar to Si and can be doped to obtain both, n- and p-type CuO. However, there are other challenges, such as transport properties and identification of a partner material, that hinder the utilization of CuO. As the dominant phase under ambient oxygen partial pressures and temperatures below 1000℃, it has the potential to become a coexistent p-n-junction alternative to the Si-homojunction if the right partner can be identified. A possible candidate for a CuO based solar cell could be CuO – ZnO. The p-n-junction would be a replacement for a Si-based solar cell instead of an additional layer in a tandem solar cell as the Cu_2O – ZnO interface would be. The band alignment and behavior of the CuO – ZnO junction have to be studied to asses the potential of the junction.

6.1. Outlook

The successful formation of the Cu_2O – ZnO p-n-junction without a CuO interlayer has to be a priority within this field. This can be achieved, for example, by utilizing the PLD technique in either of the two temperature regimes. At low temperatures, system specific processes to ensure the formation of the junction without a CuO interlayer, and uniform film growths have to be established. Taking into account that the thin films typically grow more uniform at higher temperatures, a substrate temperature of ~600℃ or higher is suggested. The corresponding oxygen partial pressure can be created utilizing Harmix and establishing the partial pressure of water. The preferred growing order for future devices would be Cu_2O deposited on ZnO. Additionally, the samples could be annealed in an atmosphere with oxygen partial pressure

defined by the annealing temperature. This technique could allow post-deposition reduction of the CuO layer, and substantially decrease the requirements imposed on the deposition method. However, defect chemistry might ultimately hinder the successful formation. Hence, a simultaneous study of the influence of intrinsic defects in ZnO and Cu_2O on the formation of the junction and the CuO layer present have to be conducted.

Different observation techniques can be utilized in addition to the (S)TEM techniques used above, to observe the junction, such as nano-beam diffraction. The technique would allow the identification of the local structure, enabling the identification of very thin CuO domains. The combination of efforts to reduce the size of the interlayer and (S)TEM observations would also allow the influence of each experimental parameter on the structure near the junction, and lead towards a CuO free interface, and structural characterization of such an interface.

The third step is the electrical characterization of the p-n-junction. This includes the characterization of the CuO free junction, as well as the conditions under which the interlayer is introduced at the junction, and the electrical properties prior the existence, the change in properties during formation, and the electrical properties of such a junction with the interlayer. This characterization procedure would allow the determination whether the CuO is ultimately responsible for the bad conversion efficiency, as has been theorized before.

Finally, different architectures of the p-n-junctions can be established to utilize the junction in different electrical devices. It has to be established if the interlayer forms during the usage of these devices, and how the formation can be prevented in junctions utilized in larger devices. Only then can the coexistent Cu_2O – ZnO p-n-heterojunction be viewed as a valid alternative to a Si-based homojunction.

6. Conclusion

Bibliography

[1]   R. E. Hummel, *Understanding Materials Science: History, Properties, Applications*. Springer Science & Business Media, 2004.

[2]   G. L. Pearson and W. H. Brattain, "History of Semiconductor Research," *Proceedings of the IRE,* https://doi.org/10.1109/JRPROC.1955.278042 vol. 43, no. 12, pp. 1794-1806, 1955.

[3]   A. Volta, "II. Of the method of rendering very sensible the weakest natural or artificial electricity," *Philosophical Transactions of the Royal Society of London,* no. 72, pp. xxxvi-xxxvi, 1782.

[4]   G. Busch, "Early History of the Physics and Chemistry of Semiconductors - From Doubts to Fact in a Hundred Years," *European Journal of Physics,* https://doi.org/10.1088/0143-0807/10/4/002 vol. 10, pp. 254-264, 1989.

[5]   E. Velmre, "Thomas Johann Seebeck (1770-1831)," *Estonian Journal of Engineering,* vol. 13, no. 4, 2007.

[6]   M. Faraday and others, "I. Experimental Researches in Electricity — Fifteenth Series," *Philosophical Transactions of the Royal Society of London,* vol. 129, pp. 1-12, 1839.

[7]   M. Riordan and L. Hoddeson, "The Origins of the p-n-Junction," *IEEE Spectrum,* https://doi.org/10.1109/6.591664 vol. 34, no. 6, pp. 46-51, 1997.

[8]   R. S. Ohl, "Light-Sensitive Electric Device Including Silicon," ed: Google Patents, 1948.

[9]   C. Kittel, S. Johnson, Ed. *Introduction to Solid State Physics*, 8th ed. New York: Wiley 1976.

[10]   S. J. Blundell and K. M. Blundell, *Concepts in Thermal Physics*, 2nd ed. Oxford, UK: OUP Oxford, 2006.

[11]   S. H. Simon, *The Oxford Solid State Basics*, 1st ed. Oxford, UK: OUP Oxford, 2013.

[12]   A. Bhaumik, A. Haque, P. Karnati, M. F. N. Taufique, R. Patel, and K. Ghosh, "Copper Oxide Based Nanostructures for Improved Solar Cell Efficiency," *Thin Solid Films,* https://doi.org/10.1016/j.tsf.2014.09.056 vol. 572, pp. 126-133, 2014.

[13]   Y. Ievskaya, R. L. Z. Hoye, A. Sadhanala, K. P. Musselman, and J. L. MacManus-Driscoll, "Fabrication of ZnO/Cu_2O Heterojunctions in Atmospheric Conditions: Improved Interface Quality and Solar Cell Performance," *Solar Energy Materials and Solar Cells,* https://doi.org/10.1016/j.solmat.2014.09.018 vol. 135, pp. 43-48, 2015.

[14]   T. Minami, Y. Nishi, T. Miyata, and J.-i. Nomoto, "High-Efficiency Oxide Solar Cells with ZnO/Cu_2O Heterojunction Fabricated on Thermally Oxidized Cu_2O Sheets," *Applied Physics Express,* vol. 4, no. 6, pp. 062301-062301, 2011.

[15]   L.-S. Wang, H. Wu, S. R. Desai, and L. Lou, "Electronic Structure of Small Copper Oxide Clusters: From Cu_2O to Cu_2O_4," *Phys. Rev. B,* https://doi.org/10.1103/PhysRevB.53.8028 vol. 53, pp. 8028-8031, 1996.

[16]   A. E. Gunnæs *et al.*, "Epitaxial Strain-Induced Growth of CuO at Cu_2O/ZnO Interfaces," *The Journal of Physical Chemistry C,* vol. 120, no. 41, pp. 23552-23558, 2016.

[17]   J. Gan *et al.*, "Structural Properties of Cu_2O Epitaxial Films Grown on c-Axis Single Crystal ZnO by Magnetron Sputtering," *Applied Physics Letters,* vol. 108, no. 15, pp. 152110-152110, 2016.

[18]   T. Wong, S. Zhuk, S. Masudy-Panah, and G. Dalapati, "Current Status and Future Prospects of Copper Oxide Heterojunction Solar Cells," *Materials,* vol. 9, no. 4, pp. 271-271, 2016.

[19]   A. Sproul, "Understanding the p-n-Junction," *Solar Cells: Resources for the Secondary Science Teacher,* pp. 13-24, 2003.

Bibliography

[20] M. Grätzel, "Solar Cells to Dye for," *Nature,* https://doi.org/10.1038/421586a vol. 421, pp. 586-587, 2003.

[21] S. A. Agarkar, V. V. Dhas, S. Muduli, and S. B. Ogale, "Dye Sensitized Solar Cell (DSSC) by a Novel Fully Room Temperature Process: a Solar Paint for Smart Windows and Flexible Substrates," *RSC Adv.,* https://doi.org/10.1039/C2RA22182A vol. 2, pp. 11645-11649, 2012.

[22] T. Oekermann, D. Zhang, T. Yoshida, and H. Minoura, "Electron Transport and Back Reaction in Nanocrystalline TiO_2 Films Prepared by Hydrothermal Crystallization," *The Journal of Physical Chemistry B,* https://doi.org/10.1021/jp034918z vol. 108, no. 7, pp. 2227-2235, 2004.

[23] T. Minami, T. Miyata, K. Ihara, Y. Minamino, and S. Tsukada, "Effect of ZnO Film Deposition Methods on the Photovoltaic Properties of $ZnO–Cu_2O$ Heterojunction Devices," *Thin Solid Films,* https://doi.org/10.1016/j.tsf.2005.07.167 vol. 494, no. 1, pp. 47-52, 2006.

[24] K. Akimoto, S. Ishizuka, M. Yanagita, Y. Nawa, G. K. Paul, and T. Sakurai, "Thin Film Deposition of Cu_2O and Application for Solar Cells," *Solar Energy,* https://doi.org/10.1016/j.solener.2005.10.012 vol. 80, no. 6, pp. 715-722, 2006.

[25] M. Izaki, K.-t. Mizuno, T. Shinagawa, M. Inaba, and A. Tasaka, "Photochemical Construction of Photovoltaic Device Composed of p-Copper (I) Oxide and n-Zinc Oxide," *Journal of the Electrochemical Society,* vol. 153, no. 9, pp. C668-C672, 2006.

[26] Z. Li, A. Rahtu, and R. G. Gordon, "Atomic Layer Deposition of Ultrathin Copper Metal Films from a Liquid Copper (I) Amidinate Precursor," *Journal of The Electrochemical Society,* vol. 153, no. 11, pp. C787-C794, 2006.

[27] G. Ghiotti and F. Boccuzzi, "Chemical and Physical Properties of Copper-Based Catalysts for CO Shift Reaction and Methanol Synthesis," *Catalysis Reviews,* https://doi.org/10.1080/01614948708078069 vol. 29, no. 2-3, pp. 151-182, 1987.

[28] B. K. Meyer *et al.*, "Binary Copper Oxide Semiconductors: From Materials Towards Devices," *physica status solidi (b),* https://doi.org/10.1002/pssb.201248128 vol. 249, no. 8, pp. 1487-1509, 2012.

[29] L. Xia, Z. Liu, and P. A. Taskinen, "Phase equilibria study of Cu–O–ZnO system in various oxygen partial pressures," *Ceramics International,* vol. 42, no. 4, pp. 5418-5426, 2016/03/01/ 2016.

[30] L. Schramm, G. Behr, W. Löser, and K. Wetzig, "Thermodynamic reassessment of the Cu-O phase diagram," *Journal of phase equilibria and diffusion,* vol. 26, no. 6, pp. 605-612, 2005.

[31] R. Schmid, "A thermodynamic analysis of the Cu-O system with an associated solution model," *Metallurgical Transactions B,* vol. 14, no. 3, pp. 473-481, 1983.

[32] B. Hallstedt, D. Risold, and L. J. Gauckler, "Thermodynamic assessment of the copper-oxygen system," *Journal of phase equilibria,* vol. 15, no. 5, pp. 483-499, 1994.

[33] M. Clavaguera-Mora, J. Touron, J. Rodrıguez-Viejo, and N. Clavaguera, "Thermodynamic description of the Cu - O system," *Journal of Alloys and Compounds,* vol. 377, no. 1-2, pp. 8-16, 2004.

[34] D. Shishin and S. A. Decterov, "Critical assessment and thermodynamic modeling of the Cu–O and Cu–O–S systems," *Calphad,* vol. 38, pp. 59-70, 2012.

[35] K. W. Lay and G. M. Renlund, "Oxygen pressure effect on the Y2O3—BaO—CuO liquidus," *Journal of the American Ceramic Society,* vol. 73, no. 5, pp. 1208-1213, 1990.

[36] J. K. Sharma, M. S. Akhtar, S. Ameen, P. Srivastava, and G. Singh, "Green Synthesis of CuO Nanoparticles with Leaf Extract of Calotropis Gigantea and its Dye-Sensitized Solar Cells Applications," *Journal of Alloys and Compounds,* https://doi.org/10.1016/j.jallcom.2015.01.172 vol. 632, pp. 321-325, 2015.

[37]   S. Masudy-Panah, G. K. Dalapati, K. Radhakrishnan, A. Kumar, and H. R. Tan, "Reduction of Cu-rich interfacial layer and improvement of bulk CuO property through two-step sputtering for p-CuO/n-Si heterojunction solar cell," *Journal of Applied Physics,* vol. 116, no. 7, p. 074501, 2014/08/21 2014.

[38]   S. Masudy-Panah *et al.*, "p-CuO/n-Si heterojunction solar cells with high open circuit voltage and photocurrent through interfacial engineering," *Progress in Photovoltaics: Research and Applications,* vol. 23, no. 5, pp. 637-645, 2015/05/01 2015.

[39]   C. Carel, M. Mouallem-Bahout, and J. Gaudé, "Re-Examination of the Non-Stoichiometry and Defect Structure of Copper(II) Oxide or Tenorite, $Cu1\pm zO$ or $CuO1\pm\epsilon$: A Short Review," *Solid State Ionics,* https://doi.org/10.1016/S0167-2738(98)00247-1 vol. 117, no. 1, pp. 47-55, 1999.

[40]   A. Boudene, K. Hack, A. Mohammad, D. Neuschuetz, and E. Zimmermann, "Experimental investigation and thermochemical assessment of the system Cu-O," *Zeitschrift fuer Metallkunde,* vol. 83, no. 9, pp. 663-668, 1992.

[41]   R. D. Holmes, H. S. C. O'Neill, and R. J. Arculus, "Standard Gibbs free energy of formation for $Cu2O$, NiO, CoO, and FexO: High resolution electrochemical measurements using zirconia solid electrolytes from 900–1400 K," *Geochimica et Cosmochimica Acta,* vol. 50, no. 11, pp. 2439-2452, 1986/11/01/ 1986.

[42]   T. Peters, *Equilibrium fugacities of the Cu2O-CuO and Cu-Cu2O buffers*. 1983, pp. 7-11.

[43]   M. W. Chase, J. L. Curnutt, J. R. Downey, R. A. McDonald, A. N. Syverud, and E. A. Valenzuela, "JANAF Thermochemical Tables, 1982 Supplement," *Journal of Physical and Chemical Reference Data,* vol. 11, no. 3, pp. 695-940, 1982/07/01 1982.

[44]   F. Biccari, *Defects and Doping in Cu₂O*. University of Rome, 2012.

[45]   D. C. Look, "Recent advances in ZnO materials and devices," *Materials Science and Engineering: B,* vol. 80, no. 1, pp. 383-387, 2001/03/22/ 2001.

[46]   Ü. Özgür *et al.*, "A comprehensive review of ZnO materials and devices," *Journal of Applied Physics,* vol. 98, no. 4, p. 041301, 2005.

[47]   S. B. Ogale, *Thin films and heterostructures for oxide electronics*. Springer Science & Business Media, 2006.

[48]   N. H. Nickel and E. Terukov, *Zinc Oxide-A Material for Micro-and Optoelectronic Applications: Proceedings of the NATO Advanced Research Workshop on Zinc Oxide as a Material for Micro-and Optoelectronic Applications, held in St. Petersburg, Russia, from 23 to 25 June 2004*. Springer Science & Business Media, 2006.

[49]   C. Jagadish and S. J. Pearton, *Zinc oxide bulk, thin films and nanostructures: processing, properties, and applications*. Elsevier, 2011.

[50]   A. Janotti and C. G. Van de Walle, "Fundamentals of Zinc Oxide as a Semiconductor," *Reports on progress in physics,* vol. 72, no. 12, p. 126501, 2009.

[51]   A. Mang, K. Reimann, and S. Rübenacke, "Band gaps, crystal-field splitting, spin-orbit coupling, and exciton binding energies in ZnO under hydrostatic pressure," *Solid State Communications,* vol. 94, no. 4, pp. 251-254, 1995/04/01/ 1995.

[52]   Z. L. Wang, "Nanostructures of zinc oxide," *Materials Today,* vol. 7, no. 6, pp. 26-33, 2004/06/01/ 2004.

[53]   D. C. Reynolds, D. C. Look, B. Jogai, C. W. Litton, G. Cantwell, and W. C. Harsch, "Valence-band ordering in ZnO," *Physical Review B,* vol. 60, no. 4, pp. 2340-2344, 07/15/ 1999.

[54]   Y. Chen *et al.*, "Plasma assisted molecular beam epitaxy of ZnO on c -plane sapphire: Growth and characterization," *Journal of Applied Physics,* vol. 84, no. 7, pp. 3912-3918, 1998/10/01 1998.

[55]   V. Srikant and D. R. Clarke, "On the optical band gap of zinc oxide," *Journal of Applied Physics,* vol. 83, no. 10, pp. 5447-5451, 1998/05/15 1998.

[56]   L. Pankratz, "Thermodynamic properties of elements and oxides," *United States Bureau of Mines Bull.,* vol. 509, 1982.

[57]   F. Tuomisto, V. Ranki, K. Saarinen, and D. C. Look, "Evidence of the Zn Vacancy Acting as the Dominant Acceptor in n-Type ZnO," *Physical Review Letters,* vol. 91, no. 20, p. 205502, 11/10/ 2003.

[58]   D. C. Look, G. C. Farlow, P. Reunchan, S. Limpijumnong, S. B. Zhang, and K. Nordlund, "Evidence for Native-Defect Donors in n-Type ZnO," *Physical Review Letters,* vol. 95, no. 22, p. 225502, 11/21/ 2005.

[59]   G. Xiong, J. Wilkinson, B. Mischuck, S. Tüzemen, K. B. Ucer, and R. T. Williams, "Control of p- and n-type conductivity in sputter deposition of undoped ZnO," *Applied Physics Letters,* vol. 80, no. 7, pp. 1195-1197, 2002/02/18 2002.

[60]   Z. L. Wang, "Zinc Oxide Nanostructures: Growth, Properties and Applications," *Journal of Physics: Condensed Matter,* vol. 16, no. 25, pp. R829-R829, 2004.

[61]   D. C. Reynolds, D. C. Look, and B. Jogai, "Optically pumped ultraviolet lasing from ZnO," *Solid State Communications,* vol. 99, no. 12, pp. 873-875, 1996/09/01/ 1996.

[62]   D. M. Bagnall *et al.*, "Optically pumped lasing of ZnO at room temperature," *Applied Physics Letters,* vol. 70, no. 17, pp. 2230-2232, 1997/04/28 1997.

[63]   M. Cardona and Y. Y. Peter, *Fundamentals of semiconductors*. Springer, 2005.

[64]   M. N. Kamalasanan and S. Chandra, "Sol-gel synthesis of ZnO thin films," *Thin Solid Films,* vol. 288, no. 1, pp. 112-115, 1996/11/15/ 1996.

[65]   F. Paraguay D, W. Estrada L, D. R. Acosta N, E. Andrade, and M. Miki-Yoshida, "Growth, structure and optical characterization of high quality ZnO thin films obtained by spray pyrolysis," *Thin Solid Films,* vol. 350, no. 1, pp. 192-202, 1999/08/15/ 1999.

[66]   H. Funakubo, N. Mizutani, M. Yonetsu, A. Saiki, and K. Shinozaki, "Orientation Control of ZnO Thin Film Prepared by CVD," *Journal of Electroceramics,* vol. 4, no. 1, pp. 25-32, 1999/12/01 1999.

[67]   K. Sakurai, M. Kanehiro, K. Nakahara, T. Tetsuhiro, S. Fujita, and S. Fujita, "Effects of oxygen plasma condition on MBE growth of ZnO," *Journal of Crystal Growth,* vol. 209, no. 2, pp. 522-525, 2000/02/01/ 2000.

[68]   T. Yamamoto, T. Shiosaki, and A. Kawabata, "Characterization of ZnO piezoelectric films prepared by rf planar-magnetron sputtering," *Journal of Applied Physics,* vol. 51, no. 6, pp. 3113-3120, 1980/06/01 1980.

[69]   J. Molarius, J. Kaitila, T. Pensala, and M. Ylilammi, "Piezoelectric ZnO films by r.f. sputtering," *Journal of Materials Science: Materials in Electronics,* vol. 14, no. 5, pp. 431-435, 2003/05/01 2003.

[70]   R. Ondo-Ndong, G. Ferblantier, F. Pascal-Delannoy, A. Boyer, and A. Foucaran, "Electrical properties of zinc oxide sputtered thin films," *Microelectronics Journal,* vol. 34, no. 11, pp. 1087-1092, 2003/11/01/ 2003.

[71]   J. G. E. Gardeniers, Z. M. Rittersma, and G. J. Burger "Preferred orientation and piezoelectricity in sputtered ZnO films," *Journal of Applied Physics,* vol. 83, no. 12, pp. 7844-7854, 1998/06/15 1998.

[72]   D. I. Florescu, L. G. Mourokh, F. H. Pollak, D. C. Look, G. Cantwell, and X. Li, "High spatial resolution thermal conductivity of bulk ZnO (0001)," *Journal of Applied Physics,* vol. 91, no. 2, pp. 890-892, 2002/01/15 2001.

[73]   Ü. Özgür *et al.*, "Thermal conductivity of bulk ZnO after different thermal treatments," *Journal of Electronic Materials,* vol. 35, no. 4, pp. 550-555, 2006/04/01 2006.

[74]   J.-Q. Li *et al.*, "Temperature dependence of Cu2O orientations in the oxidation of Cu (111)/ZnO (0001) by oxygen plasma," *Chinese Physics B,* vol. 21, no. 7, p. 076401, 2012/07 2012.

[75]   B. Mohamad Fariza, J. Sasano, T. Shinagawa, H. Nakano, S. Watase, and M. Izaki, "Electrochemical Growth of (0001)-n-ZnO Film on (111)-p-Cu2O Film and the Characterization of the Heterojunction Diode," *Journal of The Electrochemical Society,* https://doi.org/10.1149/1.3623776 vol. 158, no. 10, pp. D621-D625, 2011.

[76]   B. Fultz and J. M. Howe, *Transmission Electron Microscopy and Diffractometry of Materials*. Springer Berlin Heidelberg, 2012.

[77]   D. B. Williams, D. B. Williams, and C. B. Carter, *Transmission Electron Microscopy: A Textbook for Materials Science. Diffraction. II*. Springer, 1996.

[78]   P. A. Korzhavyi and B. Johansson, "Literature review on the properties of cuprous oxide Cu2O and the process of copper oxidation," Sweden, 1404-0344, 2011, [Online]. Available: http://inis.iaea.org/search/search.aspx?orig_q=RN:43041487.

[79]   C. J. Adkins and C. J. Adkins, *Equilibrium Thermodynamics*. Cambridge University Press, 1983.

[80]   D. A. McQuarrie, H. Cox, J. D. Simon, and J. Choi, *Physical Chemistry: A Molecular Approach*. University Science Books, 1997.

[81]   I. Barin and G. Platzki, *Thermochemical data of pure substances*. Weinheim ; New York : VCH, 1995.

[82]   M. Chase Jr, "NIST-JANAF thermochemical tables fourth edition," *J. Phys. Chem. Ref. Data, Monograph,* vol. 9, 1998.

[83]   J. A. Dean, *Lange's handbook of chemistry*. New york; London: McGraw-Hill, Inc., 1999.

[84]   M. Lannoo and J. Bourgoin, "Point defects in semiconductors. Vol," 1981.

[85]   T. Norby, "A kr öger-vink compatible notation for defects in inherently defective sublattices," *Journal of the Korean Ceramic Society,* vol. 47, no. 1, pp. 19-25, 2010.

[86]   A. Janotti and C. G. Van de Walle, "New insights into the role of native point defects in ZnO," *Journal of Crystal Growth,* vol. 287, no. 1, pp. 58-65, 2006/01/18/ 2006.

[87]   C. G. Van de Walle and J. Neugebauer, "First-principles calculations for defects and impurities: Applications to III-nitrides," *Journal of Applied Physics,* vol. 95, no. 8, pp. 3851-3879, 2004/04/15 2004.

[88]   D. B. Laks, C. G. Van de Walle, G. F. Neumark, P. E. Blöchl, and S. T. Pantelides, "Native defects and self-compensation in ZnSe," *Physical Review B,* vol. 45, no. 19, pp. 10965-10978, 05/15/ 1992.

[89]   G. W. Tomlins, J. L. Routbort, and T. O. Mason, "Zinc self-diffusion, electrical properties, and defect structure of undoped, single crystal zinc oxide," *Journal of Applied Physics,* vol. 87, no. 1, pp. 117-123, 2000.

[90]   L. Schmidt-Mende and J. MacManus-Driscoll, *ZnO—Nanostructures, Defects, and Devices*. 2007, pp. 40-48.

[91]   A. Janotti and C. G. Van de Walle, "Native point defects in ZnO," *Physical Review B,* vol. 76, no. 16, p. 165202, 10/04/ 2007.

[92]   C. G. Van de Walle, "Hydrogen as a Cause of Doping in Zinc Oxide," *Physical Review Letters,* vol. 85, no. 5, pp. 1012-1015, 07/31/ 2000.

[93]   A. Janotti and C. G. Van de Walle, "Hydrogen multicentre bonds," *Nature Materials,* vol. 6, p. 44, 12/03/online 2006.

[94]   N. L. Peterson and C. L. Wiley, "Diffusion and point defects in Cu2O," *Journal of Physics and Chemistry of Solids,* vol. 45, no. 3, pp. 281-294, 1984/01/01/ 1984.

Bibliography

[95]   O. Porat and I. Riess, "Defect chemistry of Cu2−yO at elevated temperatures. Part II: Electrical conductivity, thermoelectric power and charged point defects," *Solid State Ionics,* vol. 81, no. 1, pp. 29-41, 1995/10/01/ 1995.

[96]   H. Raebiger, S. Lany, and A. Zunger, "Origins of the p-type nature and cation deficiency in ${\mathrm{Cu}}_{2}\mathrm{O}$ and related materials," *Physical Review B,* vol. 76, no. 4, p. 045209, 07/16/ 2007.

[97]   M. Riordan and L. Hoddeson, "Crystal Fire: The Invention, Development and Impact of the Transistor," *IEEE Solid-State Circuits Society Newsletter,* https://doi.org/10.1109/N-SSC.2007.4785574 vol. 12, no. 2, pp. 24-29, 2007.

[98]   T. Minami, Y. Nishi, and T. Miyata, "Heterojunction Solar Cell With 6% Efficiency Based on an n-Type Aluminum–Gallium–Oxide Thin Film and p-Type Sodium-Doped Cu2O Sheet," *Applied Physics Express,* vol. 8, no. 2, p. 022301, 2015.

[99]   R. Soref and B. Bennett, "Electrooptical Effects in Silicon," *IEEE Journal of Quantum Electronics,* vol. 23, no. 1, pp. 123-129, 1987.

[100] L. Zhang and M. Jaroniec, "Toward designing semiconductor-semiconductor heterojunctions for photocatalytic applications," *Applied Surface Science,* vol. 430, pp. 2-17, 2018/02/01/ 2018.

[101] S. Iqbal, Z. Pan, and K. Zhou, "Enhanced photocatalytic hydrogen evolution from in situ formation of few-layered MoS2/CdS nanosheet-based van der Waals heterostructures," *Nanoscale,* 10.1039/C7NR01705G vol. 9, no. 20, pp. 6638-6642, 2017.

[102] X. Zhang *et al.*, "Efficient band structure tuning, charge separation, and visible-light response in ZrS2-based van der Waals heterostructures," *Energy & Environmental Science,* 10.1039/C5EE03490F vol. 9, no. 3, pp. 841-849, 2016.

[103] M. Reza Gholipour, C.-T. Dinh, F. Béland, and T.-O. Do, "Nanocomposite heterojunctions as sunlight-driven photocatalysts for hydrogen production from water splitting," *Nanoscale,* 10.1039/C4NR07224C vol. 7, no. 18, pp. 8187-8208, 2015.

[104] Z. Zhang and J. T. Yates, "Band Bending in Semiconductors: Chemical and Physical Consequences at Surfaces and Interfaces," *Chemical Reviews,* vol. 112, no. 10, pp. 5520-5551, 2012/10/10 2012.

[105] M. Xu *et al.*, "Rationally Designed n–n Heterojunction with Highly Efficient Solar Hydrogen Evolution," *ChemSusChem,* vol. 8, no. 7, pp. 1218-1225, 2015.

[106] X. Wang *et al.*, "Enhanced photocatalytic hydrogen evolution by prolonging the lifetime of carriers in ZnO/CdS heterostructures," *Chemical Communications,* 10.1039/B904668B no. 23, pp. 3452-3454, 2009.

[107] J. Liu, B. Cheng, and J. Yu, "A new understanding of the photocatalytic mechanism of the direct Z-scheme g-C3N4/TiO2 heterostructure," *Physical Chemistry Chemical Physics,* 10.1039/C6CP06147H vol. 18, no. 45, pp. 31175-31183, 2016.

[108] J. Jin, J. Yu, D. Guo, C. Cui, and W. Ho, "A Hierarchical Z-Scheme CdS–WO3 Photocatalyst with Enhanced CO2 Reduction Activity," *Small,* vol. 11, no. 39, pp. 5262-5271, 2015.

[109] P. Zhou, J. Yu, and M. Jaroniec, "All-Solid-State Z-Scheme Photocatalytic Systems," *Advanced Materials,* vol. 26, no. 29, pp. 4920-4935, 2014.

[110] J. Low, C. Jiang, B. Cheng, S. Wageh, A. A. Al-Ghamdi, and J. Yu, "A Review of Direct Z-Scheme Photocatalysts," *Small Methods,* vol. 1, no. 5, 2017.

[111] B. Zhu, P. Xia, Y. Li, W. Ho, and J. Yu, "Fabrication and photocatalytic activity enhanced mechanism of direct Z-scheme g-C3N4/Ag2WO4 photocatalyst," *Applied Surface Science,* vol. 391, pp. 175-183, 2017/01/01/ 2017.

[112] K. He *et al.*, "Enhanced visible light photocatalytic H2 production over Z-scheme g-C3N4 nansheets/WO3 nanorods nanocomposites loaded with Ni(OH)x cocatalysts," *Chinese Journal of Catalysis,* vol. 38, no. 2, pp. 240-252, 2017/02/01/ 2017.

[113] X. Wang, G. Liu, L. Wang, Z. G. Chen, G. Q. Lu, and H. M. Cheng, "ZnO–CdS@Cd Heterostructure for Effective Photocatalytic Hydrogen Generation," *Advanced Energy Materials,* vol. 2, no. 1, pp. 42-46, 2012.

[114] L. Wang and W. A. Daoud, "BiOI/TiO2-nanorod array heterojunction solar cell: Growth, charge transport kinetics and photoelectrochemical properties," *Applied Surface Science,* vol. 324, pp. 532-537, 2015/01/01/ 2015.

[115] J. Kong, X. Lai, Z. Rui, H. Ji, and S. Ji, "Multichannel charge separation promoted ZnO/P25 heterojunctions for the photocatalytic oxidation of toluene," *Chinese Journal of Catalysis,* vol. 37, no. 6, pp. 869-877, 2016/06/01/ 2016.

[116] M. Ichimura and Y. Song, "Band Alignment at the Cu2O/ZnO Heterojunction," *Japanese Journal of Applied Physics,* vol. 50, no. 5, p. 051002, 2011/05/20 2011.

[117] G. J. C. L. Bruls, "Exact formulas for a thin-lens system with an arbitrary number of lenses," *Optik,* vol. 126, no. 6, pp. 659-662, 2015/03/01/ 2015.

[118] J. Ltd., *JEM-2100 Electron Microscope*. Japan: JEOL Ltd., 2004.

[119] R. P. Feynman, R. B. Leighton, and M. L. Sands, *The Feynman Lectures on Physics*. Addison-Wesley Publishing Company, 1963.

[120] Q.-H. Zhang, D.-D. Xiao, and L. Gu, "Aberration-corrected scanning transmission electron microscopy for complex transition metal oxides," *Chinese Physics B,* vol. 25, no. 6, p. 066803, 2016/06 2016.

[121] M. Scimeca, S. Bischetti, H. K. Lamsira, R. Bonfiglio, and E. Bonanno, "Energy Dispersive X-ray (EDX) microanalysis: A powerful tool in biomedical research and diagnosis," (in eng), *European journal of histochemistry : EJH,* vol. 62, no. 1, pp. 2841-2841, 2018.

[122] D. Sholl and J. A. Steckel, *Density Functional Theory: A Practical Introduction*. Wiley, 2009.

[123] P. Hohenberg and W. Kohn, "Inhomogeneous Electron Gas," *Physical Review,* vol. 136, no. 3B, pp. B864-B871, 11/09/ 1964.

[124] W. H. Brattain, "The Copper Oxide Rectifier," *Reviews of Modern Physics,* vol. 23, no. 3, pp. 203-203, 1951.

[125] L. Zhang, D. Jing, L. Guo, and X. Yao, "In Situ Photochemical Synthesis of Zn-Doped Cu2O Hollow Microcubes for High Efficient Photocatalytic H2 Production," *ACS Sustainable Chemistry & Engineering,* https://doi.org/10.1021/sc500045e vol. 2, no. 6, pp. 1446-1452, 2014.

[126] J. Herion, E. A. Niekisch, and G. Scharl, "Investigation of Metal Oxide/Cuprous Oxide Heterojunction Solar Cells," *Solar Energy Materials,* https://doi.org/10.1016/0165-1633(80)90022-2 vol. 4, no. 1, pp. 101-112, 1980.

[127] A. E. Rakhshani, "Preparation, Characteristics and Photovoltaic Properties of Cuprous Oxide—A Review," *Solid-State Electronics,* https://doi.org/10.1016/0038-1101(86)90191-7 vol. 29, no. 1, pp. 7-17, 1986.

[128] V. F. Drobny and L. Pulfrey, "Properties of Reactively-Sputtered Copper Oxide Thin Films," *Thin Solid Films,* https://doi.org/10.1016/0040-6090(79)90504-2 vol. 61, no. 1, pp. 89-98, 1979.

[129] L. C. Olsen, F. W. Addis, and W. Miller, "Experimental and Theoretical Studies of Cu2O Solar Cells," *Solar Cells,* https://doi.org/10.1016/0379-6787(82)90050-3 vol. 7, no. 3, pp. 247-279, 1982.

[130] L. C. Olsen, R. C. Bohara, and M. W. Urie, "Explanation for Low-Efficiency Cu2O Schottky-Barrier Solar Cells," *Applied physics letters,* vol. 34, no. 1, pp. 47-49, 1979.

[131] H. Tanaka, T. Shimakawa, T. Miyata, H. Sato, and T. Minami, "Electrical and Optical Properties of TCO–Cu$_2$O Heterojunction Devices," *Thin Solid Films,* https://doi.org/10.1016/j.tsf.2004.06.180 vol. 469-470, pp. 80-85, 2004.

[132] A. Mittiga, E. Salza, F. Sarto, M. Tucci, and R. Vasanthi, "Heterojunction Solar Cell with 2% Efficiency Based on a Cu$_2$O Substrate," *Applied Physics Letters,* https://doi.org/10.1063/1.2194315 vol. 88, no. 16, pp. 163502-163502, 2006.

[133] M. Izaki, T. Shinagawa, K.-T. Mizuno, Y. Ida, M. Inaba, and A. Tasaka, "Electrochemically constructed p-Cu2O/n-ZnO heterojunction diode for photovoltaic device," *Journal of Physics D: Applied Physics,* vol. 40, no. 11, pp. 3326-3329, 2007/05/18 2007.

[134] S. Jeong, A. Mittiga, E. Salza, A. Masci, and S. Passerini, "Electrodeposited ZnO/Cu2O heterojunction solar cells," *Electrochimica Acta,* vol. 53, no. 5, pp. 2226-2231, 2008.

[135] C. Xiang, G. M. Kimball, R. L. Grimm, B. S. Brunschwig, H. A. Atwater, and N. S. Lewis, "820 mV open-circuit voltages from Cu2O/CH3CN junctions," *Energy & Environmental Science,* 10.1039/C0EE00554A vol. 4, no. 4, pp. 1311-1318, 2011.

[136] F. Gao, X.-J. Liu, J.-S. Zhang, M.-Z. Song, and N. Li, "Photovoltaic properties of the p-CuO/n-Si heterojunction prepared through reactive magnetron sputtering," *Journal of applied physics,* vol. 111, no. 8, p. 084507, 2012.

[137] K. P. Musselman, A. Marin, L. Schmidt-Mende, and J. L. MacManus-Driscoll, "Incompatible Length Scales in Nanostructured Cu2O Solar Cells," *Advanced Functional Materials,* vol. 22, no. 10, pp. 2202-2208, 2012/05/23 2012.

[138] F. Shao, J. Sun, L. Gao, J. Luo, Y. Liu, and S. Yang, "High Efficiency Semiconductor-Liquid Junction Solar Cells based on Cu/Cu2O," *Advanced Functional Materials,* vol. 22, no. 18, pp. 3907-3913, 2012/09/25 2012.

[139] Y. S. Lee *et al.*, "Ultrathin amorphous zinc-tin-oxide buffer layer for enhancing heterojunction interface quality in metal-oxide solar cells," *Energy & Environmental Science,* vol. 6, no. 7, pp. 2112-2118, 2013.

[140] T. Minami, Y. Nishi, and T. Miyata, "High-Efficiency Cu$_2$O-Based Heterojunction Solar Cells Fabricated Using a Ga$_2$O$_3$ Thin Film as N-Type Layer," *Applied Physics Express,* vol. 6, no. 4, pp. 044101-044101, 2013.

[141] C. Jayathilaka, V. Kapaklis, W. Siripala, and S. Jayanetti, "Improved efficiency of electrodeposited p-CuO/n-Cu2O heterojunction solar cell," *Applied Physics Express,* vol. 8, no. 6, p. 065503, 2015.

[142] S. H. Lee, M. Shin, S. J. Yun, and J. W. Lim, "CuOx/a-Si: H heterojunction thin-film solar cell with an n-type μc-Si: H depletion-assisting layer," *Progress in Photovoltaics: Research and Applications,* vol. 23, no. 11, pp. 1642-1648, 2015.

[143] A. O. Musa, T. Akomolafe, and M. J. Carter, "Production of cuprous oxide, a solar cell material, by thermal oxidation and a study of its physical and electrical properties," *Solar Energy Materials and Solar Cells,* vol. 51, no. 3, pp. 305-316, 1998/02/27/ 1998.

[144] R. Padiyath, J. Seth, and S. V. Babu, "Deposition of copper oxide films by reactive laser ablation of copper formate in an r.f. oxygen plasma ambient," *Thin Solid Films,* vol. 239, no. 1, pp. 8-15, 1994/02/15/ 1994.

[145] W. Siripala, L. D. R. D. Perera, K. T. L. De Silva, J. K. D. S. Jayanetti, and I. M. Dharmadasa, "Study of annealing effects of cuprous oxide grown by electrodeposition technique," *Solar Energy Materials and Solar Cells,* vol. 44, no. 3, pp. 251-260, 1996/11/30/ 1996.

[146] G. P. Pollack and D. Trivich, "Photoelectric properties of cuprous oxide," *Journal of Applied Physics,* vol. 46, no. 1, pp. 163-172, 1975/01/01 1975.

[147] K. Kawaguchi, R. Kita, M. Nishiyama, and T. Morishita, "Molecular beam epitaxy growth of CuO and Cu2O films with controlling the oxygen content by the flux ratio of Cu/O+," *Journal of crystal growth,* vol. 143, no. 3-4, pp. 221-226, 1994.

[148] T. Minami, H. Tanaka, T. Shimakawa, T. Miyata, and H. Sato, "High-Efficiency Oxide Heterojunction Solar Cells Using Cu2O Sheets," *Japanese Journal of Applied Physics,* vol. 43, no. No. 7A, pp. L917-L919, 2004/06/18 2004.

[149] Y. Nishi, T. Miyata, and T. Minami, "Effect of Inserting a Thin Buffer Layer on the Efficiency in n-ZnO/p-Cu2O Heterojunction Solar Cells," *Journal of Vacuum Science & Technology A,* https://doi.org/10.1116/1.3698596 vol. 30, no. 4, pp. 04D103-04D103, 2012.

[150] K. Jacobi, G. Zwicker, and A. Gutmann, "Work Function, Electron Affinity and Band Bending of Zinc Oxide Surfaces," *Surface Science,* https://doi.org/10.1016/0039-6028(84)90199-7 vol. 141, no. 1, pp. 109-125, 1984.

[151] S. W. Lee *et al.*, "Improved Cu2O-Based Solar Cells Using Atomic Layer Deposition to Control the Cu Oxidation State at the p-n Junction," *Advanced Energy Materials,* vol. 4, no. 11, p. 1301916, 2014/08/01 2014.

[152] Y. S. Lee *et al.*, "Nitrogen-doped cuprous oxide as a p-type hole-transporting layer in thin-film solar cells," *Journal of Materials Chemistry A,* 10.1039/C3TA13208K vol. 1, no. 48, pp. 15416-15422, 2013.

[153] C. Zuo and L. Ding, "Solution-Processed Cu2O and CuO as Hole Transport Materials for Efficient Perovskite Solar Cells," *Small,* vol. 11, no. 41, pp. 5528-5532, 2015/11/01 2015.

[154] V. Kumar, S. Masudy-Panah, C. C. Tan, T. K. S. Wong, D. Z. Chi, and G. K. Dalapati, "Copper oxide based low cost thin film solar cells," in *2013 IEEE 5th International Nanoelectronics Conference (INEC)*, 2013, pp. 443-445.

[155] S. Masudy-Panah, K. Radhakrishnan, A. Kumar, T. I. Wong, R. Yi, and G. K. Dalapati, "Optical bandgap widening and phase transformation of nitrogen doped cupric oxide," *Journal of Applied Physics,* vol. 118, no. 22, p. 225301, 2015/12/14 2015.

[156] S. Masudy-Panah, K. Radhakrishnan, H. R. Tan, R. Yi, T. I. Wong, and G. K. Dalapati, "Titanium doped cupric oxide for photovoltaic application," *Solar Energy Materials and Solar Cells,* vol. 140, pp. 266-274, 2015/09/01/ 2015.

[157] G. K. Dalapati, R. S. Kajen, S. Masudy-Panah, and P. Sonar, "Defect analysis of sputter grown cupric oxide for optical and electronics application," *Journal of Physics D: Applied Physics,* vol. 48, no. 49, p. 495104, 2015/11/18 2015.

[158] M. Yang, A. Zakutayev, J. Vidal, X. Zhang, D. S. Ginley, and F. J. DiSalvo, "Strong optical absorption in CuTaN2 nitride delafossite," *Energy & Environmental Science,* 10.1039/C3EE40621K vol. 6, no. 10, pp. 2994-2999, 2013.

[159] H. Katagiri, K. Saitoh, T. Washio, H. Shinohara, T. Kurumadani, and S. Miyajima, "Development of thin film solar cell based on Cu2ZnSnS4 thin films," *Solar Energy Materials and Solar Cells,* vol. 65, no. 1, pp. 141-148, 2001/01/01/ 2001.

[160] H. Katagiri *et al.*, "Enhanced Conversion Efficiencies of Cu2ZnSnS4-Based Thin Film Solar Cells by Using Preferential Etching Technique," *Applied Physics Express,* vol. 1, p. 041201, 2008/04/04 2008.

[161] J. Müller, B. Rech, J. Springer, and M. Vanecek, "TCO and light trapping in silicon thin film solar cells," *Solar Energy,* vol. 77, no. 6, pp. 917-930, 2004/12/01/ 2004.

[162] S. Masudy-Panah, V. Kumar, C. C. Tan, K. Radhaknshnan, D. Z. Chi, and G. K. Dalapati, "Impact of metal contact on the performance of cupric oxide based thin film solar cells," in *2013 IEEE 5th International Nanoelectronics Conference (INEC)*, 2013, pp. 378-380.

Bibliography

[163] G. Kumar Dalapati, S. Masudy-Panah, A. Kumar, C. Cheh Tan, H. Ru Tan, and D. Chi, "Aluminium alloyed iron-silicide/silicon solar cells: A simple approach for low cost environmental-friendly photovoltaic technology," *Scientific Reports,* Article vol. 5, p. 17810, 12/03/online 2015.

[164] G. K. Dalapati *et al.*, "Sputter grown sub-micrometer thick Cu2ZnSnS4 thin film for photovoltaic device application," *Materials Letters,* vol. 160, pp. 45-50, 2015/12/01/ 2015.

[165] G. K. Dalapati, S. L. Liew, A. S. W. Wong, Y. Chai, S. Y. Chiam, and D. Z. Chi, "Photovoltaic characteristics of p-β-FeSi2(Al)/n-Si(100) heterojunction solar cells and the effects of interfacial engineering," *Applied Physics Letters,* vol. 98, no. 1, p. 013507, 2011/01/03 2011.

[166] G. K. Dalapati *et al.*, "Impact of Al Passivation and Cosputter on the Structural Property of β-FeSi2 for Al-Doped β-FeSi2/n-Si(100) Based Solar Cells Application," *ACS Applied Materials & Interfaces,* vol. 5, no. 12, pp. 5455-5460, 2013/06/26 2013.

[167] C. C. Tan *et al.*, "Crystallization of Sputter-Deposited Amorphous (FeSi2)1–xAlx Thin Films," *Crystal Growth & Design,* vol. 15, no. 4, pp. 1692-1696, 2015/04/01 2015.

[168] S. Masudy-Panah *et al.*, "Nanocrystal Engineering of Sputter-Grown CuO Photocathode for Visible-Light-Driven Electrochemical Water Splitting," *ACS Applied Materials & Interfaces,* vol. 8, no. 2, pp. 1206-1213, 2016/01/20 2016.

[169] G. K. Dalapati *et al.*, "Color tunable low cost transparent heat reflector using copper and titanium oxide for energy saving application," *Scientific Reports,* Article vol. 6, p. 20182, 02/05/online 2016.

[170] B. M. Kayes, H. A. Atwater, and N. S. Lewis, "Comparison of the Device Physics Principles of Planar and Radial p-n Junction Nanorod Solar Cells," *Journal of Applied Physics,* https://doi.org/10.1063/1.1901835 vol. 97, no. 11, pp. 114302-114302, 2005.

[171] J. A. Czaban, D. A. Thompson, and R. R. LaPierre, "GaAs Core−Shell Nanowires for Photovoltaic Applications," *Nano Letters,* https://doi.org/10.1021/nl802700u vol. 9, no. 1, pp. 148-154, 2009.

[172] E. C. Garnett and P. Yang, "Silicon Nanowire Radial p−n Junction Solar Cells," *Journal of the American Chemical Society,* https://doi.org/10.1021/ja8032907 vol. 130, no. 29, pp. 9224-9225, 2008.

[173] Z. R. Fan *et al.*, "Three-Dimensional Nanopillar-Array Photovoltaics on Low-Cost and Flexible Substrates," *Nature Materials,* https://doi.org/10.1038/nmat2493 vol. 8, pp. 648-648, 2009.

[174] J. Zhang, H. Liu, Z. Wang, N. Ming, Z. Li, and A. S. Biris, "Polyvinylpyrrolidone-Directed Crystallization of ZnO with Tunable Morphology and Bandgap," *Advanced Functional Materials,* https://doi.org/10.1002/adfm.200700734 vol. 17, no. 18, pp. 3897-3905, 2007.

[175] R. Asahi, T. Morikawa, T. Ohwaki, K. Aoki, and Y. Taga, "Visible-Light Photocatalysis in Nitrogen-Doped Titanium Oxides," *Science,* https://doi.org/10.1126/science.1061051 vol. 293, no. 5528, pp. 269-271, 2001.

[176] B. W. Faughnan and R. S. Crandall, "Optical Properties of Mixed-Oxide WO3/MoO3 Electrochromic Films," *Applied Physics Letters,* https://doi.org/10.1063/1.89566 vol. 31, no. 12, pp. 834-836, 1977.

[177] R. C. Jin, Y. C. Cao, E. C. Hao, G. S. Metraux, G. C. Schatz, and C. A. Mirkin, "Controlling anisotropic nanoparticle growth through plasmon excitation," (in English), *Nature,* https://doi.org/10.1038/nature02020 vol. 425, no. 6957, pp. 487-490, Oct 2 2003.

[178] Y. Xia *et al.*, "One-Dimensional Nanostructures: Synthesis, Characterization, and Applications," *Advanced Materials,* https://doi.org/10.1002/adma.200390087 vol. 15, no. 5, pp. 353-389, 2003.

[179] A. S. A. M. P. R. G. K. Bhaumik, "Significant Enhancement of Optical Absorption Through Nano-structuring of Copper Based Oxide Semiconductors: Possible Future Materials for Solar Energy Applications," *Physical Chemistry Chemical Physics,* https://doi.org/10.1039/C4CP00827H vol. 16, no. 22, pp. 11054-11066, 2014.

[180] L. M. Wong, S. Y. Chiam, J. Q. Huang, S. J. Wang, J. S. Pan, and W. K. Chim, "Growth of Cu_2O on Ga-doped ZnO and Their Interface Energy Alignment for Thin Film Solar Cells," *Journal of Applied Physics,* https://doi.org/10.1063/1.3465445 vol. 108, no. 3, pp. 033702-033702, 2010.

[181] S.-Y. Cho, M.-K. Seo, K. S. Hong, S. J. Park, and I.-T. Kim, "Influence of ZnO evaporation on the microwave dielectric properties of La(Zn12Ti12)O3," *Materials Research Bulletin,* vol. 32, no. 6, pp. 725-735, 1997/06/01/ 1997.

[182] T. Kirchartz, J. Mattheis, and U. Rau, "Detailed Balance Theory of Excitonic and Bulk Heterojunction Solar Cells," *Phys. Rev. B,* https://doi.org/10.1103/PhysRevB.78.235320 vol. 78, pp. 235320-235320, 2008.

[183] Y. Li *et al.,* "Stable and easily sintered BaCe0.5Zr0.3Y0.2O3−δ electrolytes using ZnO and Na2CO3 additives for protonic oxide fuel cells," *Electrochimica Acta,* vol. 95, pp. 95-101, 2013/04/15/ 2013.

[184] M. Z. Khalid, J. Friis, P. Ninive, K. Marthinsen, and A. Strandlie, *A First-Principles Study of the Al (001)/Fe(0-11) Interface*. 2018, pp. 2349-2355.

[185] P. E. Blöchl, "Projector augmented-wave method," *Physical Review B,* vol. 50, no. 24, pp. 17953-17979, 12/15/ 1994.

[186] G. Kresse and D. Joubert, "From ultrasoft pseudopotentials to the projector augmented-wave method," *Physical Review B,* vol. 59, no. 3, pp. 1758-1775, 01/15/ 1999.

[187] P. W. Tasker, "The stability of ionic crystal surfaces," *Journal of Physics C: Solid State Physics,* vol. 12, no. 22, pp. 4977-4984, 1979/11/28 1979.

[188] J. F. Xu *et al.*, "Preparation and Characterization of CuO Nanocrystals," *Journal of Solid State Chemistry,* vol. 147, no. 2, pp. 516-519, 1999/11/01/ 1999.

[189] M. Ghosh and C. N. R. Rao, "Solvothermal synthesis of CdO and CuO nanocrystals," *Chemical Physics Letters,* vol. 393, no. 4, pp. 493-497, 2004/08/01/ 2004.

[190] I. Kaurova, G. Kuz'micheva, and V. B. Rybakov, *Growth and structural, optical, and electrical properties of zincite crystals*. 2013.

[191] G. B. Lesovik, A. V. Lebedev, I. A. Sadovskyy, M. V. Suslov, and V. M. Vinokur, "H-theorem in quantum physics," *Scientific reports,* vol. 6, pp. 32815-32815, 2016.

[192] P. A. Schilpp, *The Library of Living Philosophers, Volume 7. Albert Einstein: Philosopher-Scientist*. Open Court, 1949.

[193] D. J. Griffiths, *Introduction to Quantum Mechanics*. Pearson Prentice Hall, 2005.

Appendix A. Classical Thermodynamics

Classical thermodynamics uses macroscopic measurable properties of a system to describe it. A system is everything, regardless of its simplicity or complexity that is of interest [79]. This system is, depending on the conditions considered, isolated from its surrounding reservoir by different types of walls. Adiabatic walls isolate a system thermally; non-thermally isolating walls are named diathermal, the wall that is permeable to one or more substances of a system are called semipermeable, and isolating walls isolate a system completely [10]. Classical thermodynamics connects macroscopic quantities, without making any assumptions about microscopic properties. It is grounded in four fundamental laws. Recently, it has been reported that an exception for the Second Law has been found in quantum physics [191]. Nonetheless, the laws appear to be universal (the H-Theorem in quantum physics might be the only exception). These laws are based on a multitude of experiments conducted by countless scientists [79].

The simplicity and apparent generality of the laws of thermodynamics lead Albert Einstein to the following quote:

> *"A theory is more impressive the greater the simplicity of its premises is, the more different kinds of things it relates, and the more extended its area of applicability. Therefore, the deep impression which classical thermodynamics made upon me. It is the only physical theory of universal content concerning which I am convinced that, within the framework of the applicability of its basic concepts, it will never be overthrown."* [192]

While the H-Theorem in quantum physics might prove Einstein wrong, for this work, it will be disregarded.

The thermodynamic properties derived below will establish properties of the $Cu_2O - ZnO$ system, to help understand its behavior in different environments and determine a successful strategy to make the p-n-junction. By developing the relevant theory and applying it to the system as well as subsystems thereof, relevant experimental parameters can be extracted, as well as explanations of the system behavior can be found.

The Laws of Thermodynamics

The laws of thermodynamics establish different concepts of a system. The Zeroth Law establishes the idea of temperature. The First Law introduces internal energy, work, and heat, while the Second Law defines the efficiency of the conversion of heat into works, and the irreversibility of nature. The Third Law of thermodynamics states that the entropy reaches a

constant value as temperature goes to absolute zero. For any practical purposes, the Third Law does not apply to the system at hand, and it will not be further discussed.

A.1.1.   The Zeroth Law of Thermodynamics

Statement of the Zeroth Law: *If two systems are separately in thermal equilibrium with a third, then they must also be in thermal equilibrium with each other.* [79]

The Zeroth Law can be exemplified by taking two bodies, A and C, where C is a thermometer, and place them in thermal equilibrium, i.e., no heat exchange occurs. If the same thermometer is subsequently brought into contact with a third body, B, and bodies B and C are in thermal equilibrium, then, by necessity, A and B are already in thermal equilibrium, see Figure 46. The connection between temperature and thermal equilibrium appears trivial, but it leads to more extensive concepts, and the temperature is used as a well-defined variable in a system [79].

Imagining a different system with three cylinders, 1, 2, and 3, each with a certain mass of a fluid, are in thermal equilibrium. System 3 is used as a reference system, with temperature Φ_3, pressure p_3, and volume V_3. All systems remain in thermal equilibrium throughout the experiment. At the same time the parameters of state of the other two systems, p_1 and V_1, and p_2 and V_2, respectively, can be changed. Consequently, one can express:

$$\Phi_1(p_1, V_1) = \Phi_2(p_2, V_2) = \Phi_3(p_3, V_3) = \Theta \qquad (79)$$

where Θ is the empirical temperature, and $\Phi_i(p_i, V_i) = \Theta$ an equation of change. This scale-independent empirical temperature shows that a system can have a variety of pressures and corresponding volumes for the same empirical temperatures value, typically given in an isothermal plot (see Figure 47), where every point among a line has the same temperature [79].
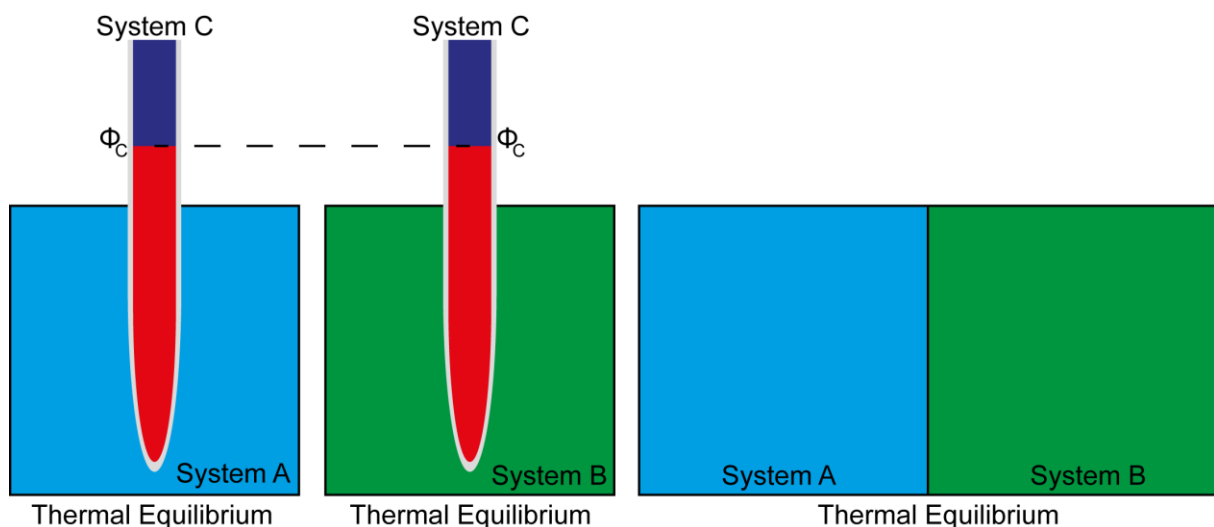

Figure 46: The three bodies, A, B, and C, where A and C are in thermal equilibrium, while B and C are in thermal equilibrium, too. Hence, A and B have to be in thermal equilibrium
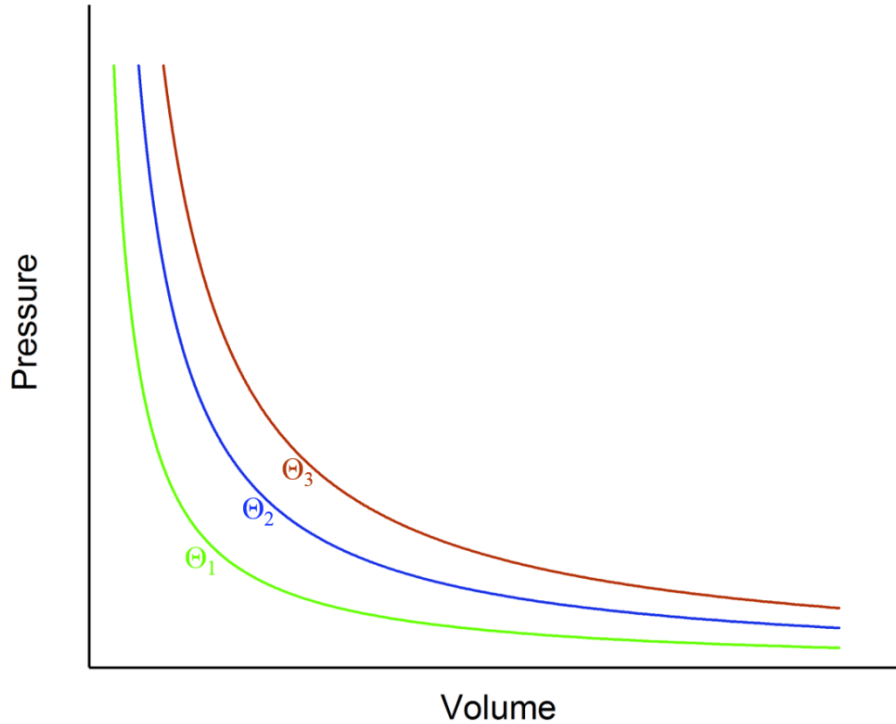
Figure 47: The isothermal plot for three different empirical temperatures Θ_1, Θ_2, and Θ_3. Along each curve, the temperature is the same. Meanwhile, the empirical temperature increases from left to right ($\Theta_1 < \Theta_2 < \Theta_3$).

A.1.2. The First Law of Thermodynamics

Statement of the First Law: *If the state of an otherwise isolated system is changed by the performance of work, the amount of work needed depends solely on the change effected and not on the means by which the work is performed nor on the intermediate stages through which the system passes between its initial and final state.* [79]

An adiabatic change of state is always related to a definite amount of energy. Thus, the total energy must be a function of state, if the First Law is true. A function of state depends solely on the current equilibrium of the system, regardless of the previous change in the system. Without any heat exchange, energy drained or supplied to the system has to decrease or increase the internal energy, U [79]. Hence, work W, as only input of energy changes the internal energy:

$$\Delta U = W \tag{80}$$

In this example, W is independent of the path. Hence, U is a function of state [79].

One can easily imagine a change of state under non-adiabatic condition. It is possible to change the state by heat alone, without doing work on the system. Consequently, the total change in internal energy in any system is dependent on the heat Q and the work W [79]:

$$\Delta U = Q + W \tag{81}$$

The distinction of whether an energy change is due to work or heat can be difficult [79]. The difficulties arise due to the, to a certain extent, equivalency of the two. Thus, to simplify, energy

due to a macroscopically ordered action will be attributed to W, and energy based on a microscopically ordered action to Q. As a change of a system takes place, ΔU is defined because U is a function of state. Consequently, the sum $Q + W$ is defined, too. Nevertheless, Q and W can only be separated if the path of the change is known. Q and W are not functions of states.

A.1.3. The Second Law of Thermodynamics

The Kelvin Statement of the Second Law: *No process is possible whose sole result is the complete conversion of heat into work.* [79]

The Clausius Statement of the Second Law: *No process is possible whose sole result is the transfer of heat from a colder to a hotter body.* [79]

The First Law of thermodynamics states the general conservation of energy by restricting the possible changes energetically possible. The two statements of the Second Law, on the other hand, determine the efficiency and irreversibility of nature [79]. The Kelvin Statement limits the conversion efficiency of transferring heat into work, while the Clausius Statement rejects the idea of transferring heat from a colder body to a hotter body without external work [79]. The two statements are the necessary, and the sufficient condition for the other one to be a true statement, meaning the validity of the Kelvin Statement is the condition and proof of the Clausius Statement, and vice versa [79].

An imaginary machine which violates the Clausius Statement is used to transfer heat from a cold reservoir at temperature Θ_2 to a hot reservoir at temperature Θ_1, without using any work. A second, regular machine is introduced to the system, using the heat from the hot reservoir and rejecting heat to the cold reservoir. Imagining now, that the first machine transfer heat at a rate Q_2, from the cold to the hot reservoir (see Figure 48). If the two engines are combined, then the result is no heat exchange at the cold side, and a heat extraction of $Q_1 - Q_2$ at the hot side, while doing an equal amount of work. This violates the Kelvin Statement [79]. The proof that if the Kelvin Statement is violated, the Clausius Statement is violated follows in a similar way [79].

The First and Second Law of thermodynamics prevent two different kinds of perpetual motion. The First Law prevents perpetual motion of the first kind, stating that an engine cannot create its energy and operate continuously due to the conservation of energy. The Second Law prevents perpetual motion of the second kind, expressing that an engine cannot run continuously using only the internal energy of a single reservoir due to the Kelvin Statement [79].
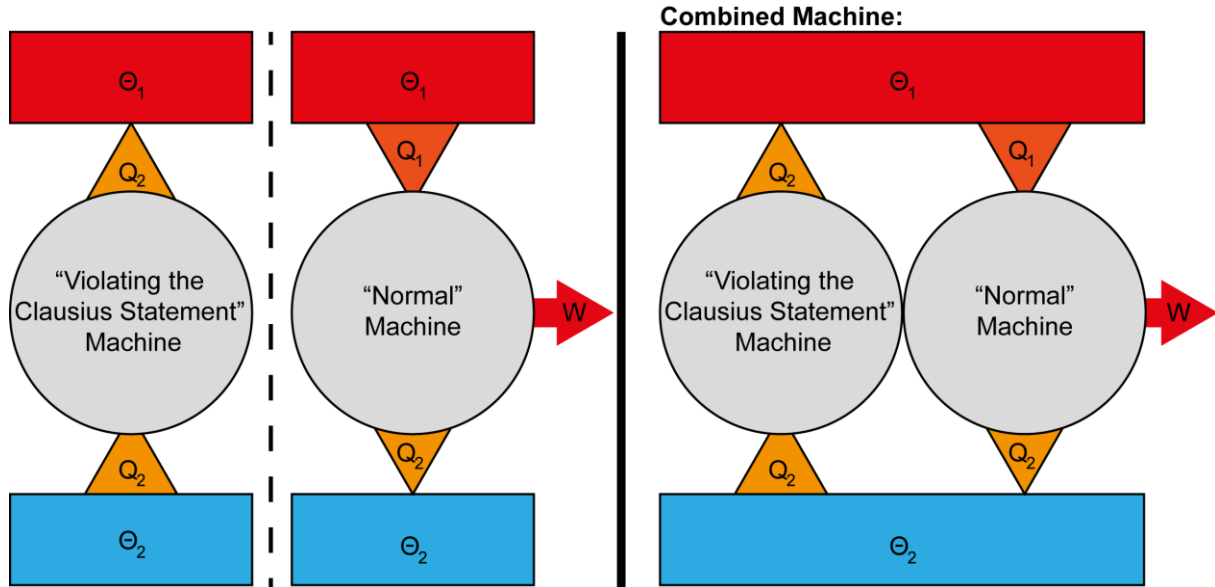
Figure 48: The first machine violates the Clausius Statement by transferring the heat Q_2, with no work. The second is a regular machine, absorbing heat Q_1 while rejecting heat Q_2, and doing work W. The combined machine violates the Kelvin Statement by extracting heat $Q_1 - Q_2$ and doing the equal amount of work $W = Q_1 - Q_2$. Hence, it converts all the heat into work.

Entropy

The thermal efficiency η_{thermal} of a heat engine satisfying the Kelvin Statement is [79]:

$$\eta_{\text{thermal}} = \frac{\text{work out}}{\text{heat in}} = \frac{W}{Q_1} \tag{82}$$

alternatively, using $W = Q_1 - Q_2$:

$$\eta_{\text{thermal}} = \frac{Q_1 - Q_2}{Q_1} = 1 - \frac{Q_2}{Q_1} \tag{83}$$

A.1.4.　Carnot's Theorem

Carnot's theorem states:

No engine operating between two given reservoirs can be more efficient than a Carnot engine between the same two reservoirs. [79]

It can be shown that any engine outperforming a Carnot engine violates one of the statements of the Second Law [79]. Let η_{rev} be the thermal efficiency of a Carnot engine. The theorem demands

$$\eta_{\text{thermal}} \leq \eta_{\text{rev}} \tag{84}$$

for any engine. Using eq. (83) yields:

$$1 - \frac{Q_2}{Q_1} \leq 1 - \frac{Q_{\text{rev},2}}{Q_{\text{rev},1}} \tag{85}$$

Appendix A. Classical Thermodynamics

Q is a measure of the empirical temperature, with $Q_A = T(\Theta_A) = T_A$, where T is a universal quantity depending only on the empirical temperature [79]. It follows that eq. (84) becomes:

$$\frac{Q_2}{Q_1} \geq \frac{Q_{\text{rev},2}}{Q_{\text{rev},1}} = \frac{T_2}{T_1} \tag{86}$$

and

$$\frac{Q_2}{T_2} = \frac{Q_1}{T_1}. \tag{87}$$

Defining heat flowing into a system as positive leads to:

$$\sum \frac{Q}{T} \leq 0 \tag{88}$$

The Carnot engine is the ideal engine, and its cycle can be used to define variables for general cycles [79].

Imagining an infinitesimally small step of a Carnot engine, with the heat supplied đQ is not a perfect differential of Q because Q is not a function of state. The absorbed heat from the reservoir, with temperature T_0, is:

$$\frac{T_0}{T}\text{đ}Q \tag{89}$$

In a full cycle, the heat absorbed must be

$$T_0 \oint \frac{\text{đ}Q}{T} \leq 0. \tag{90}$$

T_0 is, by definition, positive. Hence, the equation $\oint \frac{\text{đ}Q}{T} \leq 0$ is true for any cycle. Additionally, a reversible cycle can run the other way around, leading to: $\oint \frac{\text{đ}Q}{T} \geq 0$. Consequently, for all reversible cycles, it must be true that

$$\oint \frac{\text{đ}Q}{T} = 0 \tag{91}$$

to satisfy both equations [79].

The first condition and eq. (91) leads to the Clausius theorem, which is a consequence of the Second Law applied to each step of an infinitesimally small change [79]:

For any closed cycle $\oint \frac{\text{đ}Q}{T} \leq 0$, where the equality necessarily holds for a reversible cycle. [79]

Finally, a new variable, the entropy S, can be defined as:

$$\text{d}S = \frac{\text{đ}Q_{\text{rev}}}{T} \tag{92}$$

with đQ_{rev} the heat supplied for an infinitesimal reversible change.

A.1.5.   Entropy and Reversible Changes

The change in entropy for a reversible finite change of state of a system is

$$S_2 - S_1 = \int_1^2 \frac{đQ}{T}. \tag{93}$$

The Clausius theorem states that for any reversible cycle with states A and B, as well as paths c and d, eq. (91) has to hold [79]. Using the definition of the entropy given in eq. (92), it follows that:

$$0 = \int_{AcBdA} \frac{đQ}{T} = \int_{AcBdA} dS \tag{94}$$

and

$$\int_{AcB} dS = \int_{BdA} dS = S_B - S_A. \tag{95}$$

If one path is kept the same, for example, c, and the other one, d, is varied eq. (95) shows that the obtained value is always the same for any reversible path d between A and B. Thus, the entropy S is a function of state [79]. Consequently, dS must be a perfect differential. Moreover, due to eq. (92) and with $đQ_{rev}$ not the perfect differential, $\frac{1}{T}$ has to be an integration factor for $đQ_{rev}$.

A.1.6.   Entropy for Irreversible Changes

Equation (92) is only valid for reversible systems. The connection between entropy and heat transfer in irreversible systems can be determined in the following way. An irreversible change from B to A and a reversible change from A to B form a cycle. The Clausius theorem gives:

$$\oint \frac{đQ}{T} \leq 0 \tag{96}$$

Splitting the equation into a reversible and irreversible part yields:

$$\int_{A_{irrev}}^B \frac{đQ}{T} - \int_{A_{rev}}^B \frac{đQ}{T} \leq 0 \tag{97}$$

Rearranging eq. (97) and using eq. (93) to substitute the reversible part yields:

$$\int_{A_{irrev}}^B \frac{đQ}{T} \leq S_B - S_A \tag{98}$$

and

$$dS \geq \frac{đQ}{T} \tag{99}$$

for any infinitesimal change. The equality, again, is a necessity for reversible changes. Additionally, for a system that is thermally isolated, e.g., $đQ = 0$, it follows that $dS \geq 0$. Hence, the entropy of an isolated system cannot decrease [79].

A.1.7. Entropy for Irreversible Changes

As can be deduced from eq. (81), for an infinitesimally small change

$$\mathrm{d}U = \text{đ}Q + \text{đ}W. \tag{100}$$

For a reversible change in a simple fluid

$$\text{đ}W = -p\mathrm{d}V \tag{101}$$

and, as can be determined from eq. (92)

$$\text{đ}Q = T\mathrm{d}S. \tag{102}$$

Hence, for reversible changes

$$\mathrm{d}U = T\mathrm{d}S - p\mathrm{d}V. \tag{103}$$

All the differentials in eq. (103) are differentials of functions of states. Consequently, to determine the difference in thermal energy, only the initial and final state, as well as the existence of some reversible path are required [79]. For irreversible changes eq. (101) are differentials of functions of states. Consequently, to determine the difference in thermal energy, only the initial and final state, as well as the existence of some reversible path are required [79]. For irreversible changes eq. (101) and eq. (102) are not true. Rather, $\text{đ}Q \leq T\mathrm{d}S$ and $\text{đ}W \geq -p\mathrm{d}V$ [79]. The general form of the First Law is, therefore:

$$\mathrm{d}U = \sum_i X_i \mathrm{d}x_i \tag{104}$$

with X_i and x_i the intensive variable and the conjugated extensive variable, respectively.

A.1.8. The Chemical Potential

The natural variables of the internal energy are the entropy S and the volume V (see section 2.2.1). Adding particles to a system, without changing those variables, introduces the concept of chemical potential, μ [10]. It can be introduced by using the differential form of the internal energy (eq. (103)) and adding a term

$$\mathrm{d}U = T\mathrm{d}S - p\mathrm{d}V + \mu\mathrm{d}N \tag{105}$$

with N the number of particles in the system. Hence, considering a system without any change in S and V leads to

$$\mu = \left(\frac{\partial U}{\partial N}\right)_{S,V} \tag{106}$$

where the subscript indicates the constant natural variables of the system [10]. Considering more experimental convenient constraint, for example, constant V and T, or p and T, yield:

$$\mu = \left(\frac{\partial F}{\partial N}\right)_{T,V} \tag{107}$$

$$\mu = \left(\frac{\partial G}{\partial N}\right)_{p,T} \tag{108}$$

All functions of state can be dependent on the number of particles, e.g., $S = S(U, V, N)$. The differential form of the entropy becomes subsequently

$$dS = \left(\frac{\partial S}{\partial U}\right)_{N,V} dU + \left(\frac{\partial S}{\partial V}\right)_{U,N} dV + \left(\frac{\partial S}{\partial N}\right)_{U,V} dN. \tag{109}$$

The differential form of the entropy can be expressed by rearranging eq. (105) to

$$dS = \frac{dU}{T} + \frac{pdV}{T} + \frac{\mu dN}{T} \tag{110}$$

for any thermally isolated system $dS \geq 0$. However, two systems could exchange heat with each other, while remaining thermally isolated from their environment [10, 79]. The change of entropy of the total system is then

$$dS = \left(\frac{\partial S_1}{\partial U_1}\right)_{N,V} dU_1 + \left(\frac{\partial S_2}{\partial U_2}\right)_{N,V} dU_2 \tag{111}$$

Because of the constraint given by the thermal isolation, every loss in the internal energy of one subsystem has to be compensated by the other one [79]. Hence, eq. (111) becomes

$$dS = \left(\frac{\partial S_1}{\partial U_1}\right)_{N,V} dU + \left(\frac{\partial S_2}{\partial U_2}\right)_{N,V} dU. \tag{112}$$

By using eq. (109) and eq. (110), one finds $\left(\frac{\partial S}{\partial U}\right)_{N,V} = \frac{1}{T}$. Hence, eq. (112) becomes

$$dS = \left(-\frac{1}{T_1} + \frac{1}{T_2}\right) dU \geq 0. \tag{113}$$

This means that energy will flow from subsystem 1 to 2 for $T_1 > T_2$, and equilibrium is reached for $T_1 = T_2$ [10].

A similar argument can be made for the particle exchange. The change in entropy due to particle exchange between two systems can be expressed as:

$$dS = \left(\frac{\partial S_1}{\partial N_1}\right)_{U,V} dN_1 + \left(\frac{\partial S_2}{\partial N_2}\right)_{U,V} dN_2 \tag{114}$$

while U and V remain the same. The number of particles can neither decrease, nor increase. Hence,

$$-dN_1 = dN_2 = dN \tag{115}$$

and, correspondingly, eq. (114) becomes

$$dS = \left(\frac{\partial S_1}{\partial N_1}\right)_{U,V} dN + \left(\frac{\partial S_2}{\partial N_2}\right)_{U,V} dN \tag{116}$$

Assuming again that both subsystems are thermally isolated from the environment, and using eq. (109) and eq. (110) to determine $\left(\frac{\partial S}{\partial N}\right)_{U,V} = -\frac{\mu}{T}$, changes eq. (116)

$$dS = \left(\frac{\mu_1}{T} - \frac{\mu_2}{T}\right) dN \geq 0 \tag{117}$$

Fixing $T_1 = T_2$ determines a particle flow from subsystem 1 to 2 for $\mu_1 > \mu_2$, a flow from 2 to 1 for $\mu_1 < \mu_2$, and equilibrium for $\mu_1 = \mu_2$ [10].

A.1.9. The Grand Potential Function

A system with a volume V, energy ε, and the number of particles N is in contact with a large reservoir with energy $U - \varepsilon i$ (with $U \gg \varepsilon$), and particle number $\mathbb{N} - N$ (with $\mathbb{N} \gg N$). The entropy of such a system can be written by using a Taylor expansion and ignoring the higher order terms

$$S(U - \varepsilon, \mathbb{N} - N) = S(U, \mathbb{N}) - \varepsilon \left(\frac{\partial S}{\partial U}\right)_{N,V} - N \left(\frac{\partial S}{\partial \mathbb{N}}\right)_{U,V}. \tag{118}$$

Using the two differentials derived above, $\left(\frac{\partial S}{\partial U}\right)_{N,V} = \frac{1}{T}$ and $\left(\frac{\partial S}{\partial \mathbb{N}}\right)_{U,V} = -\frac{\mu}{T}$, the equation can be simplified to

$$S(U - \varepsilon, \mathbb{N} - N) = S(U, \mathbb{N}) - \frac{1}{T}(\varepsilon - \mu N). \tag{119}$$

The probability of such a system to be in a specific state, $P(\varepsilon, N)$, is proportional to the number of microscopic configurations in the system, Ω_{GC}. Using $S = k_B \ln \Omega_{GC}$ leads to

$$P(\varepsilon, N) \propto \Omega_{GC} \propto \exp\left(\frac{S(U - \varepsilon, \mathbb{N} - N)}{k_B}\right) \propto \exp\left(\frac{\mu N - \varepsilon}{k_B T}\right) \tag{120}$$

This is the grand canonical ensemble, also known as the Gibbs distribution. Setting the chemical potential to zero, $\mu = 0$, leads to the Boltzmann distribution. To normalize the distribution, the grand partition function $\mathcal{Z} = \sum_i \exp\left(\beta(\mu N_i - E_i)\right)$ is used, with $\beta = (k_B T)^{-1}$, and N_i the number of particles in the system with energy E_i. The normalized probability for the state i is

$$P_i = \frac{\exp\left(\beta(\mu N_i - E_i)\right)}{\mathcal{Z}} \tag{121}$$

The normalized probability can be used to describe more useful properties, such as

$$N = \sum_i N_i P_i = k_B \left(\frac{\partial \ln \mathcal{Z}}{\partial \mu}\right)_\beta \tag{122}$$

$$U = \sum_i E_i P_i = -\left(\frac{\partial \ln \mathcal{Z}}{\partial \beta}\right) + \mu N \tag{123}$$

$$S = -k_B \sum_i P_i \ln P_i = \frac{U - \mu N + k_B T \ln \mathcal{Z}}{T} \tag{124}$$

Besides the one ensemble mentioned, there are two more, equally essential ensembles in statistical mechanics. The microcanonical ensemble consists of systems with the same, fixed energy. The entropy S is, as above, $S = k_B \ln \Omega$, where Ω is the number of microstates with the fixed energy. Consequently, Ω_{mC} has to be

$$\Omega_{mC} = \exp(\beta T S) \tag{125}$$

The canonical ensemble utilizes a multitude of systems, which can exchange heat with a surrounding larger reservoir. Consequently, as they will be in thermal equilibrium, the temperature is fixed due to the Zeroth Law. The Helmholtz free energy is

$$F = -k_B T \ln \mathcal{Z}_{mC} \tag{126}$$

and, correspondingly, the partition function

$$\mathcal{Z}_{mC} = \exp(-\beta F). \tag{127}$$

Returning to the grand canonical ensemble, made of systems that are allowed to exchange both heat and particles with a large reservoir, it is essential to realize that the temperature and the chemical potential are fixed. In analogy to the canonical system, the grand partition function is

$$\mathcal{Z} = \exp(-\beta \Phi_G) \tag{128}$$

where Φ_G is the grand potential.

A.1.10. The Grand Potential

The grand potential can be expressed by rewriting eq. (128)

$$\Phi_G = -k_B T \ln \mathcal{Z} \tag{129}$$

Using the Helmholtz free energy defined above and using the relationship between the entropy and the partition function leads to

$$\Phi_G = U - TS - \mu N = F - \mu N. \tag{130}$$

The differential equation of the potential is consequently given by

$$d\Phi_G = dF - \mu dN - N d\mu = -S dT - p dV - N d\mu. \tag{131}$$

Moreover, using eq. (105) in its non-differential form, and solving for μN leads to

$$\mu N = U - TS + pV \tag{132}$$

with $U - TS + pV$ is the Gibbs free energy [10]. Hence, the chemical potential can be expressed as Gibbs free energy per particle

$$\mu = \frac{G}{N} \tag{133}$$

and the grand potential becomes, by substituting eq. (132) into eq. (130), of the form [10]

$$\Phi_G = -pV. \tag{134}$$

A.1.11. Chemical Reaction and Gibbs Free Energy

The chemical potential depends on the type of particle. Thus, eq. (105) has to be generalized to

$$dU = T dS - p dV + \sum_i \mu_i dN_i \tag{135}$$

with N_i the number of particles of species i and μ_i the corresponding chemical potential [10]. If both pressure and temperature are constant, the differential form of the Gibbs free energy becomes

$$\mathrm{d}G = \sum_i \mu_i \mathrm{d}N_i. \tag{136}$$

Consider a reaction with two species, A and B, such that the reaction

$$A \rightleftarrows B \tag{137}$$

occurs. Furthermore, the reaction is assumed to be gaseous. Consequently, the equilibrium concentrations are related to their respective partial pressure p_A and p_B [10]. If those partial pressures are constant, the equilibrium constant K can be defined as

$$K = \frac{p_B}{p_A} \tag{138}$$

The corresponding change in Gibbs free energy at constant pressure and temperature is

$$\mathrm{d}G = \mu_A \mathrm{d}N_A + \mu_B \mathrm{d}N_B \tag{139}$$

As before, a change in $\mathrm{d}N_A$ yields a corresponding, but opposite change in $\mathrm{d}N_B$

$$\mathrm{d}N_B = -\mathrm{d}N_A. \tag{140}$$

This leads to

$$\mathrm{d}G = (\mu_B - \mu_A)\mathrm{d}N_B. \tag{141}$$

Defining $\Delta_f G = (\mu_B - \mu_A)$, called the Gibbs free energy change per mole of formation, and using the expression for a chemical potential of an ideal gas, $\mu(p) = \mu^{\ominus} + RT \ln \frac{p_B}{p_A}$, yields [10]

$$\Delta_f G = \Delta_f G^{\ominus} + RT \ln \frac{p_B}{p_A} \tag{142}$$

where $\Delta_f G^{\ominus}$ is the difference between the two molar chemical potentials, $\mu_A^{\ominus}$ and $\mu_B^{\ominus}$. The symbol $\ominus$ denotes the value of a function measured at standard pressure and temperature.

An equilibrium is reached if $\Delta_f G = 0$. This leads to

$$\ln K = \ln \frac{p_B}{p_A} = \frac{-\Delta_f G^{\ominus}}{RT}. \tag{143}$$

Finally, the Gibbs free energy per mole of formation for a system at equilibrium can be expressed

$$\Delta_f G^{\ominus} = -RT \ln K. \tag{144}$$

Appendix B. Semiconductors

Additional information about semiconductor and their theory is provided within this chapter. The use of this information is not directly relevant for the thesis.

B.1. The Equation of Motion

The equation of motion of an electron in an energy band can be deduced by looking at the motion of a wave packet in an electric field. This wave packet contains wave functions near a wave vector $\vec{k}$ [9]. The group velocity can be defined by:

$$\vec{v}_{\text{Group}} = \frac{d\vec{\omega}}{d\vec{k}} \tag{145}$$

The frequency is $\vec{\omega} = \frac{\vec{E}}{\hbar}$, leading to

$$\vec{v}_{\text{Group}} = \frac{1}{\hbar}\frac{d\vec{E}}{d\vec{k}} = \frac{1}{\hbar}\vec{\nabla}_{\vec{k}}\vec{E}(\vec{k}). \tag{146}$$

This automatically includes the effect of the crystal on the electron motion, as it is contained in the dispersion relation $\vec{E}(\vec{k})$ [9]. In the time interval ∂t, the field $\vec{E}_{\text{Field}}$ does the work $\partial\vec{E}$ on the electron, as in

$$\partial\vec{E} = -\vec{E}_{\text{Field}}\vec{v}_{\text{Group}}\partial t. \tag{147}$$

This leads to

$$\partial\vec{E} = \left(\frac{d\vec{E}}{d\vec{k}}\right)\partial\vec{k} = \hbar\vec{v}_{\text{Group}}\partial\vec{k} \tag{148}$$

where $\partial\vec{k} = -\left(\frac{e\vec{E}_{\text{Field}}}{\hbar}\right)\partial t$ and $-e\vec{E}_{\text{Field}} = \hbar\frac{d\vec{k}}{dt}$ [9]. Hence, the external force is defined as

$$\vec{F} = \hbar\frac{d\vec{k}}{dt}. \tag{149}$$

The force term includes the Lorentz force and the electric force, influencing the electron [9]. It can be rewritten as

$$\vec{F} = -e\left(\vec{E} + \frac{1}{\hbar}\vec{\nabla}_{\vec{k}}\vec{E} \times \vec{B}\right). \tag{150}$$

A formal derivation of the force $\vec{F}$ is given in below.

B.2. Derivation of the External Force

By starting with a Bloch eigenfunction ψ_k with energy eigenvalues E_k and wavevector $\vec{k}$, the eigenfunction as well as the expectation value of the momentum of an electron in the Bloch state $\vec{k}$ can be stated as

$$\psi_k = \sum_{\vec{G}} C(\vec{k} + \vec{G}) \exp[\vec{k}_{\vec{G}} \cdot \vec{r}] \tag{151}$$

$$\vec{p}_{el} = \langle \vec{k} | -i\hbar\vec{\Delta} | \vec{k} \rangle = \sum_{\vec{G}} \hbar (\vec{k} + \vec{G}) |C(\vec{k} + \vec{G})|^2 = \hbar(\vec{k} + \sum_{\vec{G}} \vec{G}(\vec{k} + \vec{G})) \tag{152}$$

In an insulating crystal, which is electrostatically neutral except for the single electron in the state $\vec{k}$, a change to $\vec{k} + \Delta\vec{k}$ occurs by a transfer of momentum between the electron and the lattice.

The weak external force, applied for a defined time interval dt, gives the total impulse of $\vec{J} = \int \vec{F} dt$ to the system, with $\vec{F}$ the external force. For a free electron, the total impulse is

$$\vec{J} = \Delta\vec{p}_{tot} = \Delta\vec{p}_{el} = \hbar\Delta\vec{k} \tag{153}$$

where $\Delta\vec{p}_{tot}$ is the change in total momentum, and $\Delta\vec{p}_{el}$ the change in the momentum of the electron momentum [9]. If the conduction electron interacts with the periodic potential of the crystal, then the total impulse must be

$$\vec{J} = \Delta\vec{p}_{tot} = \Delta\vec{p}_{lat} + \Delta\vec{p}_{el} \tag{154}$$

where $\Delta\vec{p}_{lat}$ is the change in momentum of the lattice momentum [9]. The $\Delta\vec{p}_{el}$ can be expressed as

$$\Delta\vec{p}_{el} = \hbar\Delta\vec{k} + \sum_{\vec{G}} \vec{G} \left[\left(\vec{\nabla}_{\vec{k}} |C(\vec{k} + \vec{G})|^2 \right) \cdot \Delta\vec{k} \right]. \tag{155}$$

Determining the change in lattice momentum can be achieved rather simple. An electron reflected by the lattice transfers a certain amount of momentum. If this electron has the initial momentum $\hbar\vec{k}$, and the momentum $\hbar(\vec{k} + \vec{G})$ after the reflection, the lattice momentum changes by $-\hbar\vec{G}$ [9]. Then the lattice momentum can be expressed as

$$\Delta\vec{p}_{lat} = -\hbar \sum_{\vec{G}} \vec{G} \left[\left(\vec{\nabla}_{\vec{k}} |C(\vec{k} + \vec{G})|^2 \right) \cdot \Delta\vec{k} \right]. \tag{156}$$

The total momentum change is consequently

$$\vec{J} = \Delta\vec{p}_{lat} + \Delta\vec{p}_{el} = \hbar\Delta\vec{k} \tag{157}$$

as in the case of a free electron. Hence, by definition, $\vec{F} = \frac{d\vec{J}}{dt} = \hbar \frac{d\Delta\vec{k}}{dt}$, or, by substituting $\Delta\vec{k}$ with $\vec{k}$, it follows that

$$\vec{F} = \hbar \frac{d\vec{k}}{dt}. \tag{158}$$

B.3. Holes

Unoccupied orbitals in otherwise filled bands are of significance in semiconductors. These vacant orbitals are referred to as holes. A filled band yields a total wavevector of all electron of zero, $\sum_i \vec{k}_i = 0$. It is a consequence of the Brillouin zone. The electrons occupy all pairs of orbitals $\vec{k}$, and $-\vec{k}$ [9].

If one of these electrons is missing, for example, an electron in the orbital with wavevector $\vec{k}_e$, then the system has a total wavevector of $-\vec{k}_e$ [9]. Hence, the hole has the wavevector $\vec{k}_h$, where

$$\vec{k}_h = -\vec{k}_e. \tag{159}$$

However, the velocity of both, electrons and holes are the same [9]. The gradients of the respective energies are equal, e.g.,

$$\Delta_{\vec{k}_h} \vec{E}_h(\vec{k}_h) = \Delta_{\vec{k}_e} \vec{E}_e(\vec{k}_e). \tag{160}$$

Using eq. (146) leads to $\Delta_{\vec{k}_h} \vec{E}_h(\vec{k}_h) = \frac{\vec{v}_h}{\hbar} = \frac{\vec{v}_e}{\hbar} = \Delta_{\vec{k}_e} \vec{E}_e(\vec{k}_e)$, or simplified [9],

$$\vec{v}_h(\vec{k}_h) = \vec{v}_e(\vec{k}_e). \tag{161}$$

The mass of the hole has the same value, but the opposite sign as the electron mass [9],

$$m_h = -m_e \tag{162}$$

Finally, the equation of motion for a hole is [9],

$$\vec{F} = \hbar \frac{d\vec{k}_h}{dt} = -e\left(\vec{E}_h + \frac{1}{\hbar}\Delta_{\vec{k}_h}\vec{E}_h(\vec{k}_h) \times \vec{B}\right). \tag{163}$$

B.4. Effective Mass

Evaluating the formula for the energy, $E = \frac{\hbar^2 k^2}{2m}$, found in any quantum mechanics book [9, 11, 193], shows that both k and m influence the energy. It is imperative to realize that the electron in a periodic potential is accelerated in the same way as if the electron had an effective mass [9]. Hence, using (146) and take the time derivative yields

$$\frac{d\vec{v}_{Group}}{dt} = \frac{1}{\hbar}\frac{d^2\vec{E}}{d\vec{k}dt} = \frac{1}{\hbar}\left(\frac{d^2\vec{E}}{d\vec{k}^2}\frac{d\vec{k}}{dt}\right) \tag{164}$$

Utilizing eq. (149) gives

$$\vec{F} = \left(\frac{\hbar^2}{\frac{d^2\vec{E}}{d\vec{k}^2}}\right)\frac{d\vec{v}_{Group}}{dt} \tag{165}$$

with acceleration $\vec{a} = \frac{\mathrm{d}\vec{v}_{\text{Group}}}{\mathrm{d}t}$, the mass has to be $m = \left(\frac{\hbar^2}{\frac{\mathrm{d}^2 \vec{E}}{\mathrm{d}\vec{k}^2}} \right)$, and the effective mass is [9],

$$\frac{1}{m^*} = \frac{1}{\hbar^2} \frac{\mathrm{d}^2 \vec{E}}{\mathrm{d}\vec{k}^2}. \tag{166}$$

B.5. Thermoelectricity Treated by Classical Thermodynamics

Technically, thermoelectricity cannot be treated strictly within reversible thermodynamics. However, thermoelectricity can be used to demonstrate the limitations and shortcomings of reversible thermodynamics. First, the thermoelectric effects are described, before examining the difficulties of the treatment, as well as discussing Lord Kelvin's approach to deal with the difficulties.

B.5.1.   Thermoelectric Effects

A temperature gradient not only creates a heat flow in an electrical conductor but also an electric field. Qualitatively, the origin of this field can be explained by treating the free electrons as an electron gas [79]. Once the gas is heated, the local pressure increases. A "normal" gas would be distributed such that there is no pressure gradient within the volume [79]. An electron gas, however, cannot due to the charge of the electrons. As further discussed in section 2.5, if undistributed, the total electron charge in a domain of the p-n-junction balances the total ion charge. The disturbance of the electron charge density, due to temperature, results in a space charge, resulting in an electric field. Thus, a temperature gradient in a conductor leads to a small charge distribution that creates an electric field [79]. For small temperature gradients, the strength of this field is proportional to the gradient,

$$\vec{E} = \vec{S}\vec{\nabla}T \tag{167}$$

where the tensor $\vec{S}$ is the thermoelectric power (thermopower) of the material, $\vec{E}$ the electric field, and T the position dependent temperature within the sample [79].

As this is difficult to measure directly due to temperature gradients in the measurement equipment, the difference between the thermopowers of the two different conductors, whose junctions are at different temperatures, is usually measured [79]. The electromotive force of such a circuit is

$$\varepsilon = \int \vec{E}\mathrm{d}\vec{r} = \int \vec{S}\vec{\nabla}T \, \mathrm{d}\vec{r} = \int_{T_0}^{T_1} \vec{S}_B \mathrm{d}T + \int_{T_1}^{T_2} \vec{S}_A \mathrm{d}T + \int_{T_2}^{T_0} \vec{S}_B \mathrm{d}T. \tag{168}$$

This electromotive force is known as the Seebeck electromotive force. Its occurrence is called the Seebeck effect. Contracting the difference $\vec{S}_B - \vec{S}_A$ to $\vec{S}_{AB}$, called thermopower of the couple, leads to

$$\frac{d\varepsilon}{dT} = \vec{S}_{AB}. \tag{169}$$

This Seebeck effect provides the basis of thermometry with thermocouples [79].

The conjugate to the Seebeck effect is the Peltier effect. A flow of charge carriers comes hand in hand with a temperature flow [79]. The magnitude and sign of the thermal flux depend on the electronic structure. If the current is sufficiently small, the effect is linear with the proportionality factor Π, called the Peltier coefficient [79], where

$$Q = I(\Pi_A + \Pi_B = I\Pi_{AB}. \tag{170}$$

with I the current passing through, and Π_{AB} the Peltier coefficient of the couple. This effect is reversible [79].

The third effect is the heat generation or absorption in the conductor, proportional to the product of the current and the temperature gradient [79]. The rate of heating per unit length is

$$\dot{Q} = \mu_T I \frac{dT}{dx} \tag{171}$$

$\dot{Q}$ is known as the Thomson heat, with μ_T being the Thomson coefficient. This effect is reversible, too [79]. The Thomson coefficient is the heat capacity per unit length of the charge carriers, and sign and magnitude of μ_T depend on the electronic structure.

While in metals thermoelectric effects are small, and their usefulness confined to thermometry, these effects can be enlarged in semiconductors by changing the electronic structure. The thermopower yields detailed information about the electronic structure of a material, making it of importance in solid-state physics [79].

B.5.2. The Irreversibility in Thermoelectricity

The presence of two irreversible processes, entangled with the reversible processes discussed above, denies the rigorous treatment of thermoelectricity within reversible thermodynamics. These processes are the Joule heating, due to the electrical resistance of the conductors, and the thermal conduction. The entanglement is demonstrated below.

A wire, with a cross section A and length dx, with the current I flowing through it, and located in a temperature gradient $\frac{dT}{dx}$ has the electrical resistivity ρ and the thermal conductivity λ. The element is in a steady state. Hence, the entropy change associated with the processes within the element must be present in the surrounding [79]. Thus,

$$\dot{S}\mathrm{d}x = \frac{q(x+\mathrm{d}x)}{T(x+\mathrm{d}x)} - \frac{q(x)}{T(x)} \tag{172}$$

with $\dot{S}$ the rate of entropy generated per unit length, and q the rate of heat flow [79]. It can be rewritten as

$$\dot{S} = \frac{\mathrm{d}}{\mathrm{d}x}\left(\frac{q}{T}\right) = \frac{1}{T}\frac{\mathrm{d}q}{\mathrm{d}x} - \frac{q}{T^2}\frac{\mathrm{d}T}{\mathrm{d}x}. \tag{173}$$

Moreover, the rate of heat flow is defined as

$$q = -A\lambda\frac{\mathrm{d}T}{\mathrm{d}x}. \tag{174}$$

Additionally, applying the First Law of thermodynamics leads to

$$\dot{S} = \frac{I^2\rho}{AT} + \frac{I\mu_T}{T}\left(\frac{\mathrm{d}T}{\mathrm{d}x}\right) + \frac{A\lambda}{T^2}\left(\frac{\mathrm{d}T}{\mathrm{d}x}\right)^2 \tag{175}$$

with $\frac{I^2\rho}{AT}$ the Joule heating, $\frac{I\mu_T}{T}\left(\frac{\mathrm{d}T}{\mathrm{d}x}\right)$ the Thomson heat, and $\frac{A\lambda}{T^2}\left(\frac{\mathrm{d}T}{\mathrm{d}x}\right)^2$ the thermal conduction [79]. It is easily observable that the irreversible thermal conduction and the Joule heating cannot be small while the reversible Thomson heat is large, and vice versa [79]. Consequently, they cannot be separated.

B.5.3.   Lord Kelvin's Approach

Lord Kelvin treated only the reversible parts of the thermoelectric effect while disregarding the irreversible part. Consider a thermoelectric circuit, with one side at temperature T and the other at $\mathrm{d}T + T$, and the Seebeck electromotive force $\mathrm{d}\varepsilon$ [79]. Ignoring the irreversible processes, the circuit allows charge being passed reversibly around it, in an equilibrium state.

The conservation of energy demands that

$$\mathrm{d}\varepsilon = \Pi_{AB}(\mathrm{d}T + T) - \Pi_{AB}(T) + (\mu_A - \mu_B)\mathrm{d}T \tag{176}$$

for a unit charge passed around the circuit [79]. The equation can be rearranged to

$$\frac{\mathrm{d}\varepsilon}{\mathrm{d}T} = \vec{S}_{AB} = \frac{\mathrm{d}\Pi_{AB}}{\mathrm{d}T} + \mu_{AB} \tag{177}$$

with $\mu_{AB} = \mu_A - \mu_B$ [79].

The heat exchange that arises when charges move through the system must conserve the overall entropy because irreversible processes are excluded. The Thomson heat generates the entropy in the wire, and by the Peltier heat at the junctions in the reservoirs [79]. The total change in entropy must be zero, as in

$$\dot{S} = 0 = \frac{\Pi_{AB}(\mathrm{d}T+T)}{T+\mathrm{d}T} - \frac{\Pi_{AB}(T)}{T} + \int_T^{T+\mathrm{d}T}\frac{\mu_{AB}}{T}\mathrm{d}T. \tag{178}$$

The terms $\frac{\Pi_{AB}(\mathrm{d}T+T)}{T+\mathrm{d}T} - \frac{\Pi_{AB}(T)}{T}$ originate from the Peltier heat at the junctions, and $\int_T^{T+\mathrm{d}T}\frac{\mu_{AB}}{T}\mathrm{d}T$ is the Thomson heat in the wires [79]. Taking the temperature derivative leads to

$$0 = \frac{\mathrm{d}}{\mathrm{d}T}\left(\frac{\Pi_{AB}}{T}\right) + \frac{\mu_{AB}}{T}. \tag{179}$$

Eliminating the Thomson coefficient by using the expression for $\vec{S}_{AB}$ in eq. (179) lead to [79]

$$\vec{S}_{AB} = \frac{\mathrm{d}\varepsilon}{\mathrm{d}T} = \frac{\mathrm{d}\Pi_{AB}}{\mathrm{d}T} - T\frac{\mathrm{d}}{\mathrm{d}T}\left(\frac{\Pi_{AB}}{T}\right) = \frac{\mu_{AB}}{T}. \tag{180}$$

Finally, using eq. (179) in the temperature derivative of eq. (180) yields [79]

$$\frac{\mathrm{d}\vec{S}_{AB}}{\mathrm{d}T} = \frac{\mathrm{d}^2\varepsilon}{\mathrm{d}T^2} = -\frac{\mu_{AB}}{T}. \tag{181}$$

Equation (180) and eq. (181) are the thermoelectric equations. They are supported by experiments and can be obtained by irreversible thermodynamics, too [79].

In addition to Lord Kelvin's approach, some, like Tolman and Fine, included the irreversibility into classical thermodynamics [79]. All these approaches have in common that they divide the problem into reversible and irreversible parts, and have assumptions that are outside classical thermodynamics [79].

Appendix C. Powder XRD and SEM

The XRD patterns labeled with the corresponding orientation. The samples are the same as in section 4.1.
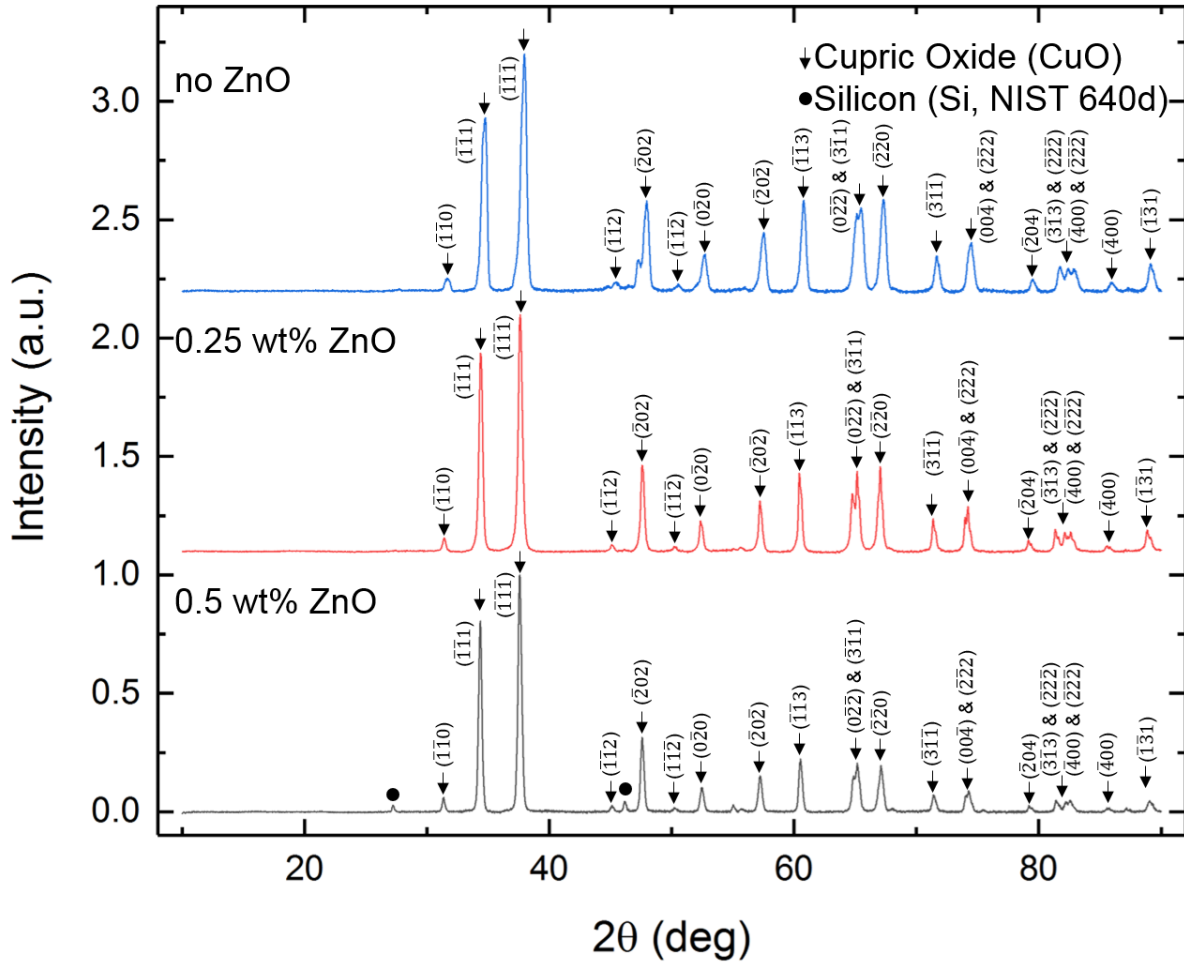

Figure 49: The corresponding planes for each peak shown in Figure 24. The samples are the same as in the said figure.
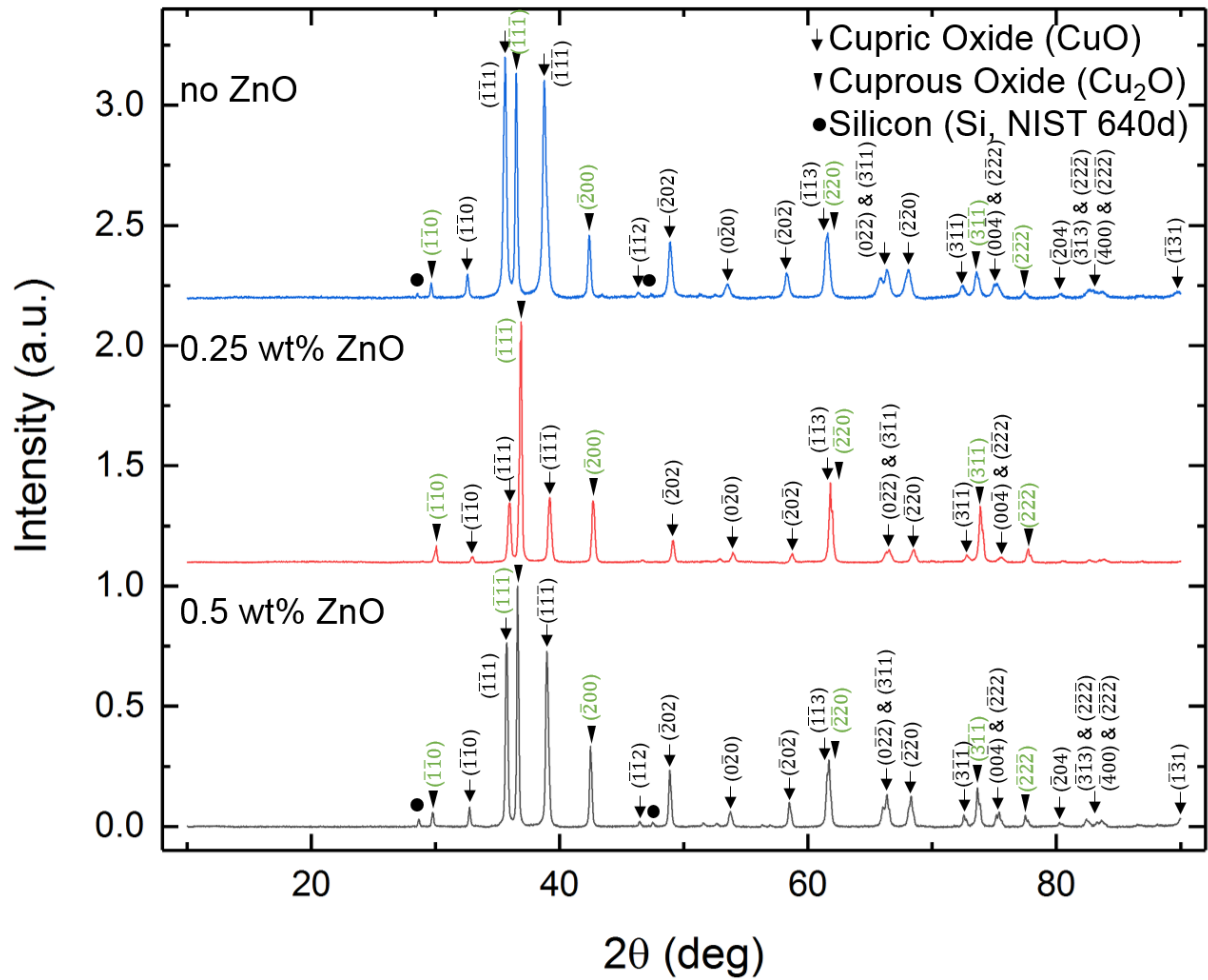
Figure 50: The corresponding plane to each peak reported. Green numbering is the Cu_2O phase, and black numbering is the CuO phase. The samples are the same as in Figure 25.
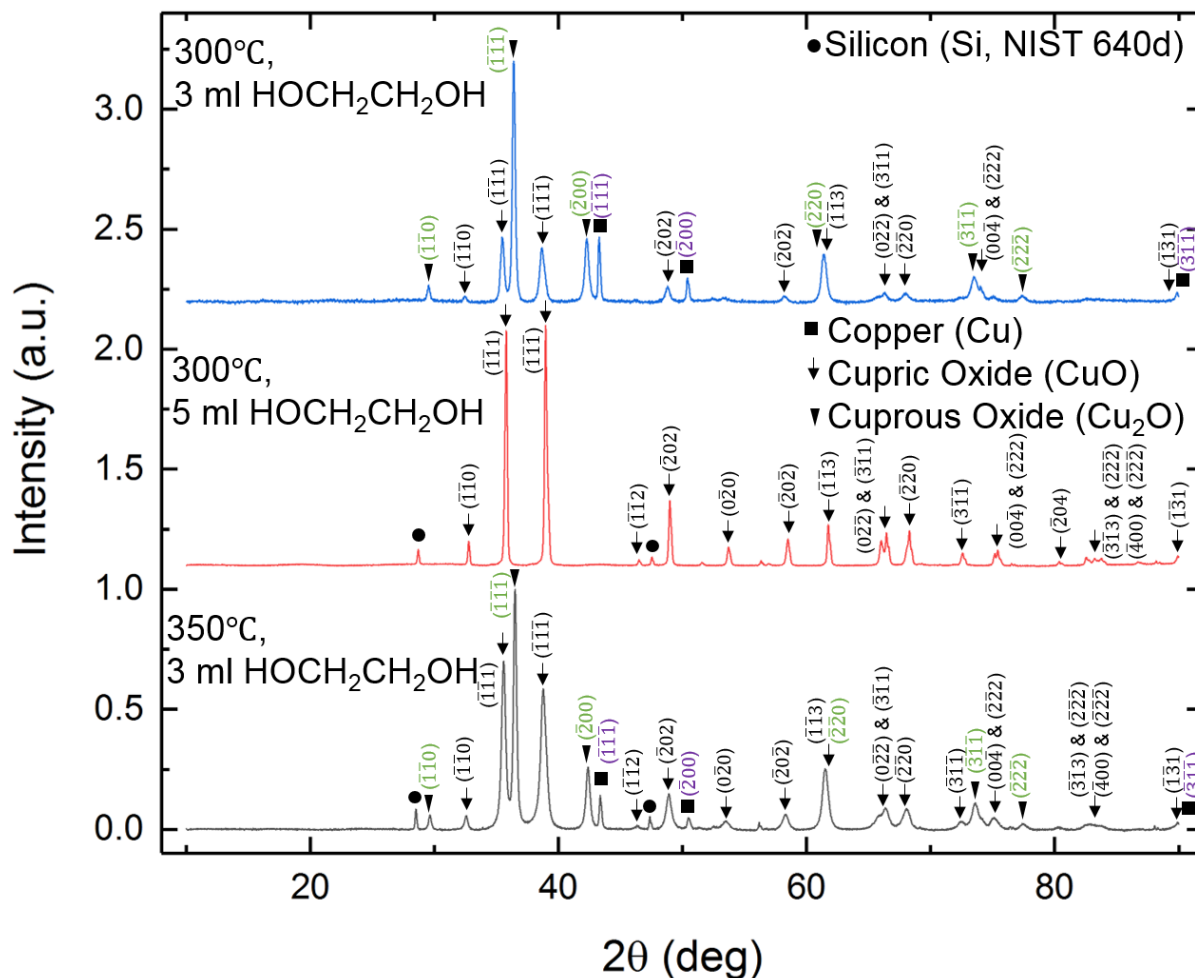
Figure 51: Each plane for the reported peaks and samples in Figure 26. Green numbering is the Cu$_2$O phase, black numbering is the CuO phase, and violet numbering is the Cu phase.
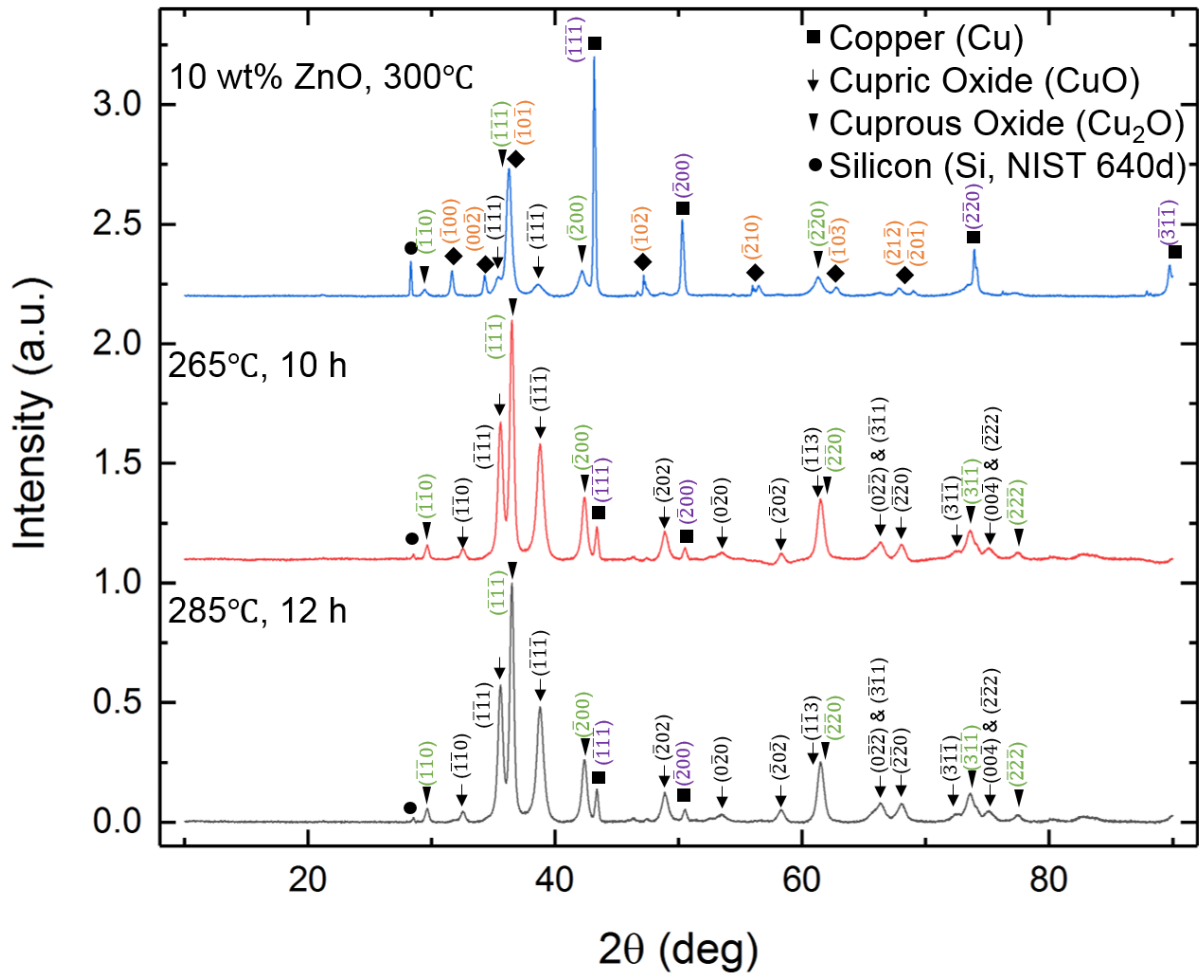
Figure 52: The planes are corresponding to the reported peak in Figure 27. The green numbering indicates the Cu_2O phase, the black numbering the CuO phase, the violet numbering the Cu phase, and the orange numbering the ZnO phase.
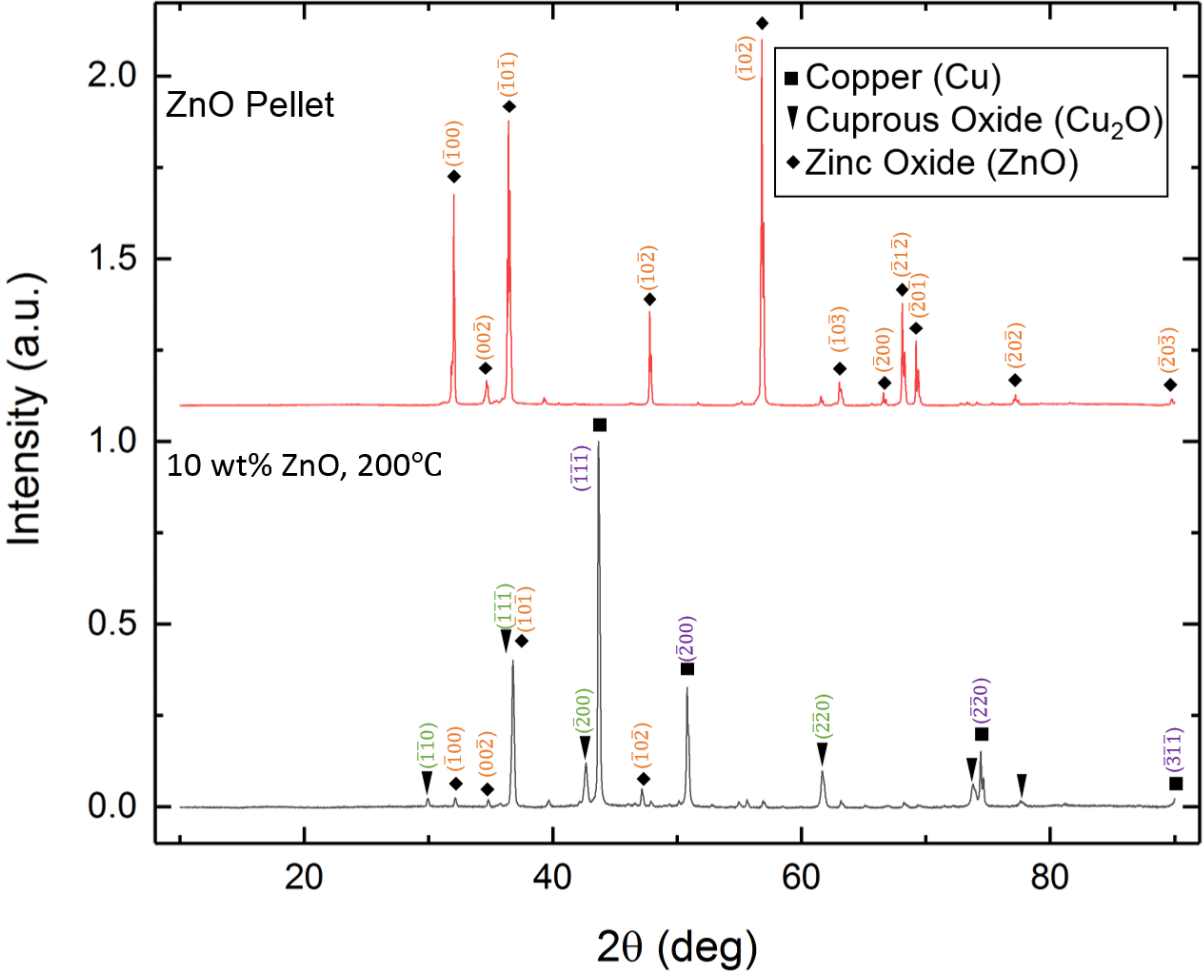
Figure 53: The planes for the reported XRD patterns in Figure 29. The green numbering is the Cu_2O phase, the violet numbering the Cu phase, and the orange numbering the ZnO phase.